

Experimental Investigation of the Spray Autoignition  
of n – Heptane in a  
Jet in Cross Flow Configuration and  
Comparison to Single Droplet Ignition Simulations

Dem Fachbereich Produktionstechnik

der

UNIVERSITÄT BREMEN

zur Erlangung des Grades  
Doktor-Ingenieur  
genehmigte

Dissertation

von

MEng. Peter Rickmers

Gutachter: Prof.-Dr. H. J. Rath  
Prof.-Dr. F. Dinkelacker

Tag der mündlichen Prüfung: 05.07.2010

---

## Abstract

Modern combustion machines, which inject liquid hydrocarbon fuels into compressed air at high temperatures, aim for a high compression ratio to achieve high process efficiency. This means, there is only a limited residence time of the fuel in the combustion chamber before autoignition. The residence time however is important in terms of vaporizing and turbulent mixing of the fuel with air. A well stirred mixture with a lean overall equivalence ratio (near the lean flammability limit) will reduce the combustion temperature and in turn reduce the production of nitric oxides (NO, N<sub>2</sub>O and NO<sub>2</sub>) through the Zeldovich mechanism.

This thesis details the results obtained under the ESA MAP project CPS III (Combustion Properties of Partially Premixed Spray Systems), where (amongst other topics) n-heptane sprays are observed under machine conditions and these experimental results are compared to numerical results of a simulation for single droplet ignition. The experiments were conducted in the hot – wind – tunnel Bremen (HWK), a newly operational Ludwig – tube type wind tunnel, which provides high temperature and high pressure flows with moderate flow rates.

The comparison of the experimental data and simulations shows, that for the simple case of an unobstructed jet in cross flow (JICF) configuration, the induction times and their scatter can be predicted fairly well by assuming for the simulation, many super-positioned monodisperse equidistant sprays of different droplet diameter and their respective volume fractions assuming a Rosin – Rammler distribution.

---

## Preamble and Acknowledgements

Diese Dissertation entstand im Rahmen meiner Arbeit in der Verbrennungsgruppe des Zentrums für Angewandte Raumfahrttechnologie und Mikrogravitation (ZARM). Sie wäre nicht ohne die Unterstützung von Prof.-Dr. H. J. Rath möglich gewesen, bei dem ich mich für die Möglichkeit bedanken möchte, die Dissertation am ZARM durchführen zu dürfen.

Ich möchte mich auch bei Prof.-Dr. F. Dinkelacker für die investierte Zeit zur Zweitbegutachtung der Dissertation und das entgegengebrachte Interesse an meiner Arbeit bedanken.

Mein besonderer Dank gilt Christian Eigenbrod, der mich immer bei meiner Arbeit unterstützt und mir geholfen hat, die Arbeit und Forschung durch viele Hinweise und hilfreiche Diskussionen zu bereichern.

Außerdem möchte ich mich bei allen Kollegen der Gruppe "Antriebs- und Energiesysteme" bedanken, die mir immer mit Rat und Tat zur Seite gestanden haben.

Insbesondere möchte ich mich bei Michael Peters, Andreas Pommerening und der ganzen Belegschaft der Werkstatt für Ihre technische Unterstützung bedanken. Ohne Ihre Hilfe und Erfahrung wären die Experimente am HWK nie möglich gewesen.

Ganz besonders bin ich für die nicht endende Unterstützung, Motivation und Geduld meiner Verlobten Isabel dankbar. Ihre vielen hilfreichen Hinweise und Ihr geduldiges Zuhören, haben diese Dissertation in der vorliegenden Form erst ermöglicht.

Meinen Eltern und meiner ganzen Familie möchte ich danken, dass sie mich immer bei meinen Zielen unterstützen und mir so die Möglichkeiten schaffen, meine Träume zu verfolgen.

Außerdem möchte ich mich bei all meinen Freunden bedanken, die unermüdlich beim Editieren der Arbeit geholfen haben.

Die Arbeit ist im Rahmen des von der ESA geförderten Projekts CPS (Combustion Properties of Partially Premixed Spray Systems) entstanden.

---

# Table of Contents

---

<b>1</b>	<b>INTRODUCTION AND MOTIVATION</b> .....	<b>1</b>
1.1	STATE OF THE ART.....	5
1.2	OBJECTIVE.....	8
<b>2</b>	<b>THEORETICAL BACKGROUND</b> .....	<b>10</b>
2.1	FLOW IN A LUDWIG – TUBE .....	10
2.1.1	<i>Introduction</i> .....	10
2.1.2	<i>Isentropic Flow Relations</i> .....	10
2.1.3	<i>Establishment of the Wave System</i> .....	14
2.1.4	<i>Moving Normal Shock</i> .....	15
2.1.5	<i>Finite Nonlinear Waves</i> .....	17
2.1.6	<i>Method of Characteristics</i> .....	18
2.1.7	<i>Shock Tube – Relations and Ludwig – Tube Modification</i> .....	21
2.2	DESCRIPTION OF A SPRAY .....	25
2.2.1	<i>Introduction</i> .....	25
2.2.2	<i>Atomisation</i> .....	26
2.2.2.1	Primary Spray Break-up.....	26
2.2.2.2	Secondary Spray Breakup .....	32
2.2.3	<i>Spray Characterization</i> .....	33
2.2.3.1	Mathematical Description of Spray Data.....	34
2.2.4	<i>Empirical Methods</i> .....	40
2.3	SINGLE DROPLET IGNITION.....	41
2.3.1	<i>Introduction</i> .....	41
2.3.2	<i>Brief Overview</i> .....	41
2.3.3	<i>Closed Vessel Simulation Validation</i> .....	44
<b>3</b>	<b>EXPERIMENTAL FACILITY</b> .....	<b>47</b>
3.1	INTRODUCTION .....	47
3.2	OVERVIEW OF COMPONENTS .....	48
3.2.1	<i>Nozzle and Fast Acting Valve</i> .....	48
3.2.2	<i>Thermal Management System</i> .....	49
3.3	PRESSURISATION SYSTEM.....	53
3.3.1	<i>Fuel Injection System</i> .....	54
3.3.2	<i>Ancillary Systems</i> .....	57
3.4	DATA ACQUISITION .....	58
3.5	EXPERIMENTAL TIMELINE .....	61
3.6	DATA ANALYSIS AND HANDLING .....	62
3.6.1	<i>Determination of the mixture ratio</i> .....	67
3.7	EXPERIMENTAL ERROR.....	71
<b>4</b>	<b>RESULTS AND DISCUSSION</b> .....	<b>77</b>
4.1	EXPERIMENTAL RESULTS .....	78
4.1.1	<i>General Overview</i> .....	78
4.1.2	<i>Effect of fuel temperature on autoignition</i> .....	80
4.1.3	<i>Effect of injection pressure on autoignition</i> .....	82
4.1.4	<i>Effect of pressure on autoignition</i> .....	83
4.1.5	<i>Effect of temperature on autoignition</i> .....	85
4.1.6	<i>Correlation between Pressure and Temperature</i> .....	86
4.1.7	<i>Phenomenological observations</i> .....	89
4.2	NUMERICAL RESULTS.....	93
4.2.1	<i>Effect of Pressure and Temperature</i> .....	93
4.2.2	<i>Effect of Droplet Diameter and Mixture-ratio</i> .....	98
4.3	COMPARISON OF NUMERICAL AND EXPERIMENTAL RESULTS.....	100
<b>5</b>	<b>CONCLUSION</b> .....	<b>107</b>
5.1	OUTLOOK .....	108
<b>6</b>	<b>APPENDIX</b> .....	<b>110</b>

---

6.1	THERMOCOUPLES .....	110
6.2	PRESSURE TRANSDUCERS .....	111
6.3	PHOTODIODES.....	111
<b>7</b>	<b>BIBLIOGRAPHY.....</b>	<b>113</b>

## List of Symbols

Symbols			
A	Area	[m <sup>2</sup> ]	γ Wave number
a	Speed of sound	[m/s]	Δ Relative Span Factor
b <sub>n</sub>	Fourier series const.		Δ <sub>B</sub> Dispersion Boundary Factor
c <sub>p</sub>	Specific heat (p const.)	[J/kg K]	κ Isentropic exponent
c <sub>v</sub>	Specific heat (V const.)	[J/kg K]	λ <sub>c</sub> Thermal conductivity [W/m K]
d <sub>0</sub>	Nozzle diameter	[m]	λ Wavelength [m]
d	Jet diameter	[m]	μ Dynamic viscosity [kg/m s]
D	Droplet diameter	[m]	ν Kinematic viscosity [m <sup>2</sup> /s]
e	Internal energy	[J]	ρ Density [kg/m <sup>3</sup> ]
E	Energy	[J]	σ Surface tension [N/m]
E <sub>a</sub>	Activation energy	[J/mol]	τ Induction time [s]
F	Force	[N]	φ Mixture ratio (Fuel/Air)
h	Specific enthalpy	[J/kg]	Ψ Fugacity [Pa]
m	Mass	[kg]	
n	Positive int. / mode		
Oh	Ohnesorge number		
p	Pressure	[Pa]	
Δp	Pressure drop (nozzle)	[Pa]	
Q	Cumulative volume fraction		
q	Growth rate		
r	Radius	[m]	
R	Specific gas constant	[J/kg K]	
Re	Reynolds number		

S	Surface	
s	Entropy	[J/K]
$u_p$	Contact surface velocity	[m/s]
U, u	Velocity (x-component)	[m/s]
V, v	Velocity (y-component)	[m/s]
$\mathcal{V}$	Volume	[m <sup>3</sup> ]
T	Temperature	[K]
t	Time	[S]
W	Shock wave velocity	[m/s]
We	Weber number	
Y	Mass fraction	
Z	Compressibility factor	
$Z^{**}$	Modified compressibility factor	

### Subscripts

0	Minimum (unless otherwise stated)	$V_f$	Volume fraction
A	Aerodynamic	$\infty$	Ambient condition
g	Gravity		
G	Gas		
i	Counter variable		
j	Counter variable		
k	Counter variable		
I	Internal		
L	Liquid		
m	Maximum		
R	Relative (velocity)		

S	Surface	
st	Surface Tension	
<b>Constants</b>		
g	Gravity	9,81 m/s <sup>2</sup>
R <sub>u</sub>	Universal gas constant	8,314 J/K·mol

## List of Abbreviations

CCD	Charge-Coupled Device	SQL	Structured Query Language
CFD	Computational Fluid Dynamics	TBV	Thermal Barrier Valve
CMOS	Complementary Metal Oxide Semiconductor	TMS	Thermal Management System
CPS	Combustion Properties of Partially Premixed Spray Systems	ZARM	Center of Applied Space Technology and Microgravity
CPU	Central Processing Unit	ZTC	Zero Temperature Gradient
CVS	Closed Vessel Simulation		
DAQ	Data Acquisition		
DUI	Droplet Uniformity Index		
EU	European Union		
ESA	European Space Agency		
GUI	Graphical User Interface		
HFCs	Hydrofluorocarbons		
HWK	Hot Wind Tunnel		
IR	Infrared		
JICF	Jet-In-Cross-Flow		
LED	Light Emitting Diode		
LIF	Laser Induced Fluorescence		
LPP	Lean Prevaporised Premixed		
MMD	Mass Median Diameter		
NMVOOC	Non Methane Volatile Organic Compounds		
NTC	Negative Temperature Coefficient		
PFCs	Perfluorocarbons		
SMD	Sauter Mean Diameter		
SPC	Stored Program Controller		

## 1 Introduction and Motivation

Today's technological society is highly dependent on energy for almost any activity imaginable. Much of this energy is currently supplied by non-renewable energy sources such as fossil fuels. Figure 1.1 shows the primary energy usage in Germany in 2006, split up into the different energy sources.

What becomes immediately evident is the very high reliance on liquid fuels. The normal process by which these are turned into energy, be it electrical or otherwise, is to mix them with air and then initiate combustion using the heat release as energy source.

The obvious problem with the combustion of hydrocarbons with air is the production of pollutants, of which the most important are CO, NO<sub>x</sub>, NMVOC (non methane volatile organic compounds) and SO<sub>2</sub>, as well as the production of environmentally problematic products, defined by the Kyoto protocol, prime among which is CO<sub>2</sub>. The other greenhouse gases which were defined by the Kyoto protocol, but are not necessarily a product of combustion, are methane (CH<sub>4</sub>), nitrous oxide (N<sub>2</sub>O), perfluorocarbons (PFCs), hydrofluorocarbons (HFCs) and sulphur hexafluoride (SF<sub>6</sub>). The development of the emissions of these gases with respect to the reference year 1990 can be seen in Figure 1.2. With the notable exception of HFCs (which are the replacement for chlorofluorocarbons and hence become increasingly important) the emission of these gases has been significantly reduced since 1990 [1].

Most of the CO<sub>2</sub> and classical greenhouse gases shown in Figure 1.2 are produced by two industrial sectors, namely energy and transport and consequently the improvement in emissions is mostly the result of reduction efforts in these two sectors. These were achieved mostly by restructuring of these industries in response to new EU and German national legislative. In response to these new laws old power plants were taken offline, being either replaced by more modern and environmentally friendly ones or existing power plants were improved. This same legislation encouraged the development of more efficient engines in transportation to conform to the new emission limits.

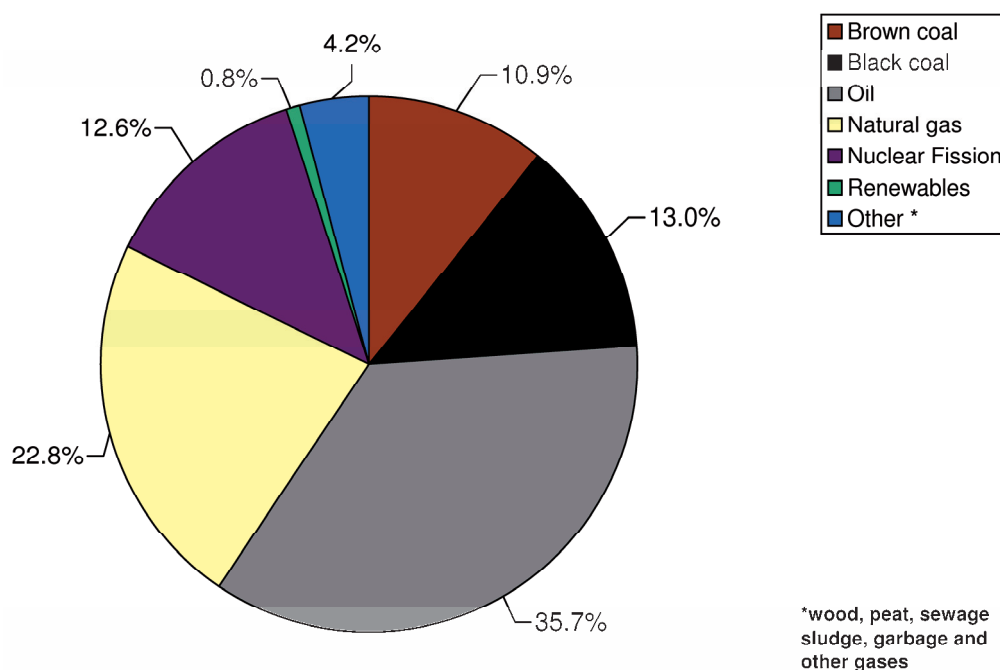


Figure 1.1 – Primary energy usage in Germany 2006 [2]

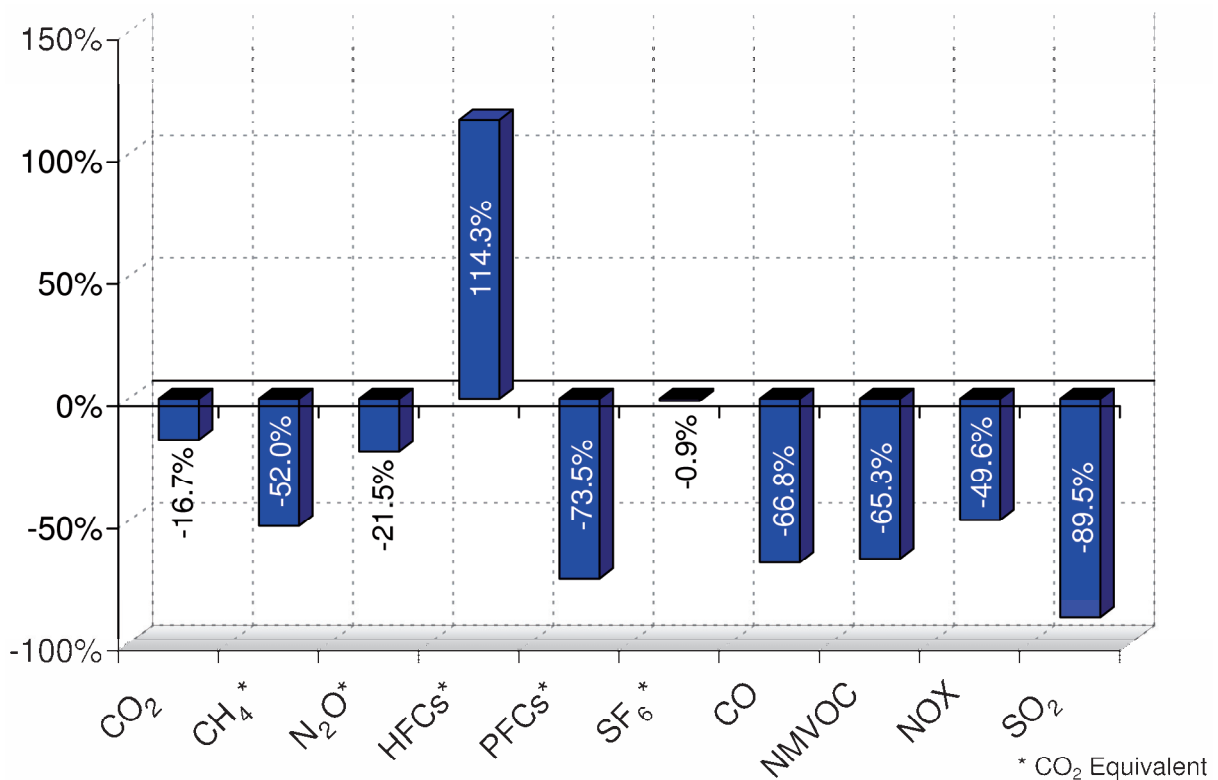


Figure 1.2 – Development of greenhouse gases in Germany 1990-2005[1]

Other approaches in the recent past proposed to replace some, if not all of the problematic liquid fuels with biologically derived alternatives for example via the Fischer – Tropsch – synthesis. In the Fischer – Tropsch – process, a synthesis gas composed of hydrogen and carbon monoxide is catalysed in chemical reactions to various types of liquid hydrocarbon fuels. It was developed by Franz Fischer and Hans Tropsch in 1925. This process has the advantage, that the CO<sub>2</sub> balance of these synthesized fuels would be neutral, the source plants (from which the initial synthesis gas is produced) having absorbed as much CO<sub>2</sub> in their growth as will be released upon combustion. There is of course some CO<sub>2</sub> production associated with the ancillary processes involved, such that a total CO<sub>2</sub> reduction of about 90% is possible.

Considering the amount of fossil fuels that are required by today's society, however, it is highly questionable if it is possible to replace all fossil liquid fuels, especially in the mid term. Simply too many unanswered questions exist. For example it is unclear, how to produce the required amounts without competing with food production or how to prepare the very varied organic input products for an efficient synthesis, since the process relies on a steady inflow of the same raw material. Also not fully solved, is the problem of how to efficiently transport the raw material from vast growing areas to the production plants. This is also reflected in the data of a study investigating the potential for renewable energy sources in Germany in the near and far term [3] (see Figure 1.3). It can clearly be seen that liquid fuels like petrol, diesel, kerosene and bio fuels still play a major part in the energy mix of the future.

What is also evident from Figure 1.3 is that a very large increase in efficiency of energy usage is projected. This increase in efficiency applies to all energy sources. In terms of liquid fuels this means not only that the limited amount of fuel must be utilised as efficiently as possible but also that in doing so the amount of greenhouse gases will be reduced.

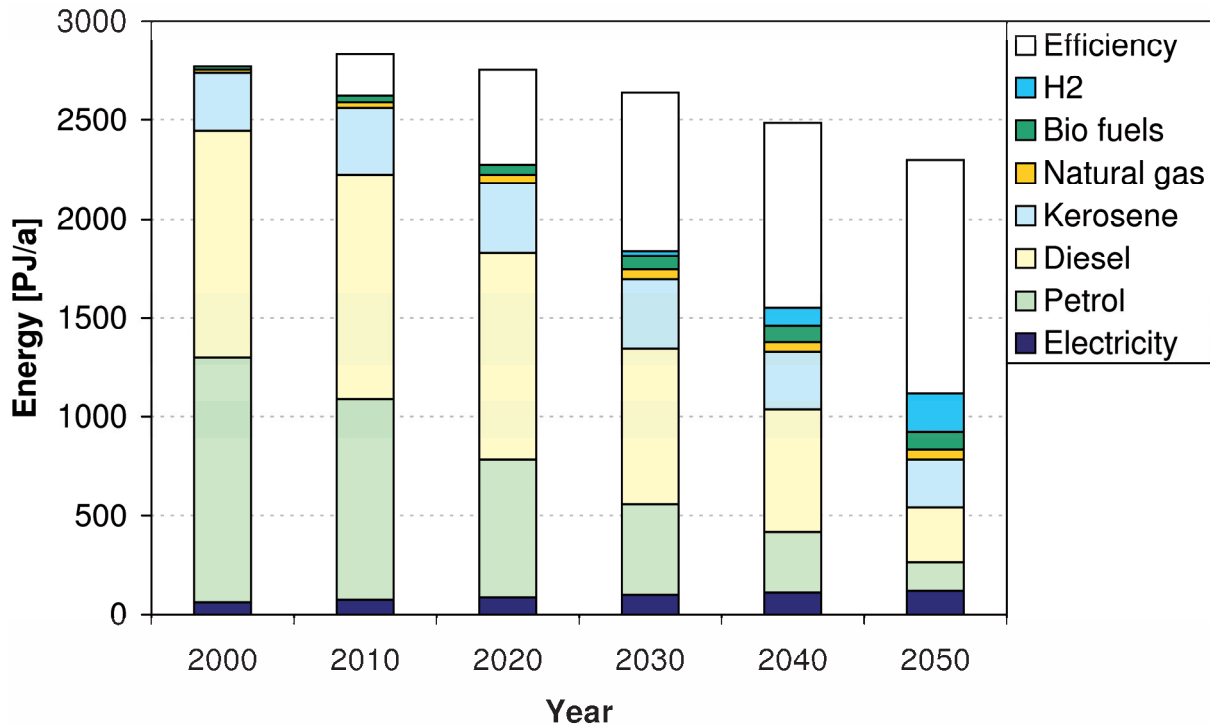


Figure 1.3 – Projection of energy sources with high eco-investment [3]

One class of the classical pollutants, the emissions of which can be significantly influenced by the combustion process itself are nitric oxides (collectively known as  $\text{NO}_x$ ). While these can also be converted after combustion (secondary measure), for example through catalytic processes, it is much preferable to avoid the production of  $\text{NO}_x$  in the first place during combustion (primary measure) [4]. This is especially true, where a secondary measure is too mass intensive, such as in an aircraft turbine, or simply too expensive, to be implemented such as in a large power plant turbine.

Nitric oxide formation is generally classified in three main categories: prompt- or Fenimore- $\text{NO}_x$ , fuel- $\text{NO}_x$  and thermal or Zeldovich- $\text{NO}_x$  [4]. The production mechanisms of  $\text{NO}_x$  through combustion are shown in Figure 1.4.

Fenimore- $\text{NO}_x$  is named after C.P. Fenimore, who first postulated its formation process in 1979. It is produced in relatively small amounts and its formation mechanism is only weakly temperature dependent. The mechanism itself is very complex and still not fully understood; nonetheless the amount of  $\text{NO}_x$  produced via this process is mostly dependent on the type of hydrocarbon used. Only small amounts of  $\text{NO}_x$  are produced in this way and hence it is of minor importance as far as reduction efforts are concerned [4].

Fuel- $\text{NO}_x$  as the name suggests is formed in the low temperature regime below 1000K from  $\text{NO}_x$  components already present in the fuel itself. This is mainly the case with coal and to some extent heavy oil. Most classical liquid fuels and especially synthetically derived ones on the other hand, only contain negligible amounts of these components. Should such compounds still be present, the only way to combat these emissions is through re-burning (see Figure 1.4) some of the  $\text{NO}_x$  in a sophisticatedly designed process. Overall however, this formation process is also of limited importance, especially considering the low quantities of culprit components in most of the classical liquid fuels in use [4].



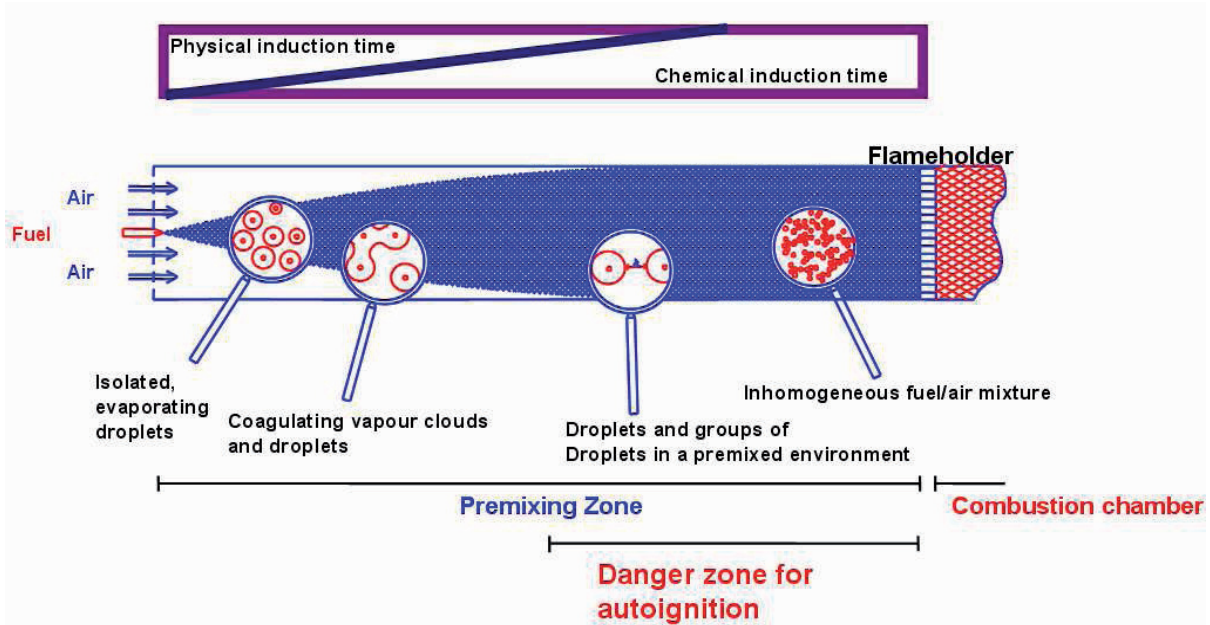


Figure 1.5 – Schematic of LPP combustion [5]

Currently, there is no complete simulation available to describe the physical and chemical processes involved in the autoignition of a spray. The development of such a simulation however, has been the goal of ongoing research since it would allow a-priori testing of the appropriate mixing devices. This thesis presents some recent results in the effort to develop a complete spray simulation.

## 1.1 State of the Art

As was described in the previous section, one of the major problems with LPP combustion is the tendency of the spray to autoignite prematurely. Autoignition or “the process of spontaneous ignition of a combustible mixture without the assistance of an external source” [6], for example a sparkplug, is present in many technical applications [6]. Sometimes autoignition is desired, such as in a diesel engine for example. In other applications such as a gasoline engine, a gas turbine (especially in future LPP combustors) or fire safety, autoignition must be avoided. Hence, a multitude of research efforts have been undertaken on the autoignition of sprays in a hot ambience.

Most studies describe autoignition in terms of an induction time,  $\tau$  [6]. This induction time can be further subdivided in a physical induction time and chemical induction time (see Figure 1.5) [7]. The physical induction time, is the time taken for the homogenous liquid jet to form a combustible mixture with the ambient air. This encompasses atomisation, evaporation and mixing. Chemical induction time on the other hand, is concerned with the chemical reactions creating a significant amount of radicals and the release of heat from these reactions [6]. It should be noted that, contrary to many other references which treat physical induction as the process requiring most time and chemical induction as a negligibly short one, there is no sharp demarcation between these two processes but rather a smooth transition as indicated in Figure 1.5.

Another ambiguity in the description of the induction time is what constitutes “ignition”. Depending on the measurement technique employed, there can be a wide range of induction

times for essentially the same experimental conditions. For example, if one uses the light generation of the emerging flame as indicator for ignition, the times measured can vary widely depending on the wavelength and sensitivity employed. Hence, a clear definition of the criterion defined as ignition is necessary for any kind of study in this area such that a later comparison to other experiments remains possible.

Most of the studies up to date have represented the induction times as a function of initial gas temperature while varying many other parameters. Many experimental studies exist and they fall into three main categories:

1. Spray injected into a hot stagnant environment with a constant volume [8-14]
2. Spray injected into a hot air stream [7, 15-23]
3. Spray ignition behind a shock in a shock tube [24-28]

In addition to the experimental studies many theoretical studies have been conducted, to attempt to describe the observations from the experiments. These theoretical models range from phenomenological models to multidimensional, multi-step (chemical) numerical models [6].

The present work shall concentrate on the second case mentioned above, a spray injected into a hot air stream, and the comparison of this type of autoignition case with a one dimensional multi-step numerical model [5]. This type of spray injection is most typical of an aircraft gas turbine application [6], where the reduction of  $\text{NO}_x$  is of foremost importance, because a secondary  $\text{NO}_x$  reduction is not possible due to weight restrictions and the  $\text{NO}_x$  is released high in the atmosphere, which is most susceptible to its damaging effects at these high altitudes.

The knowledge of induction times then logically leads to an understanding of the ignition location, when the temporal information is correlated with the flow. The ignition location is vitally important in many technical applications, where an ignition in the wrong location can lead to damage in the machinery. The location of ignition of a spray injected into a quiescent atmosphere of elevated temperature and pressure was investigated amongst others by Edwards et al. [9] and Sato et al. [8]. The latter found that the ignition was located at the stagnation point of the fuel spray tip, while the former found that ignition was initiated in eddies, containing a rather rich air/fuel mixture. These eddies were shed by the fuel jet interacting with the surrounding ambience.

There have been many studies of a spray injected into a hot flowing air stream and an overview of some of the results can be seen in Figure 1.6. The most recent of these studies are those of Spadaccini et al. [7] and Wolff et al. [23]. Spadaccini and Wolff, in contrast to other workers, utilized electrical heaters to raise the temperature of the combustion air to the desired value.

This is notable because in previous works, the air was heated with combustion devices; the air in this case is described as vitiated [6]. This has the drawback that some oxygen was already used for the heating process and in addition to this the air is contaminated with combustion products. This was found to have a significant effect on the measured induction times [6]. To offset this problem in some cases the air was replenished with fresh oxygen, the combustion products however, were still present.

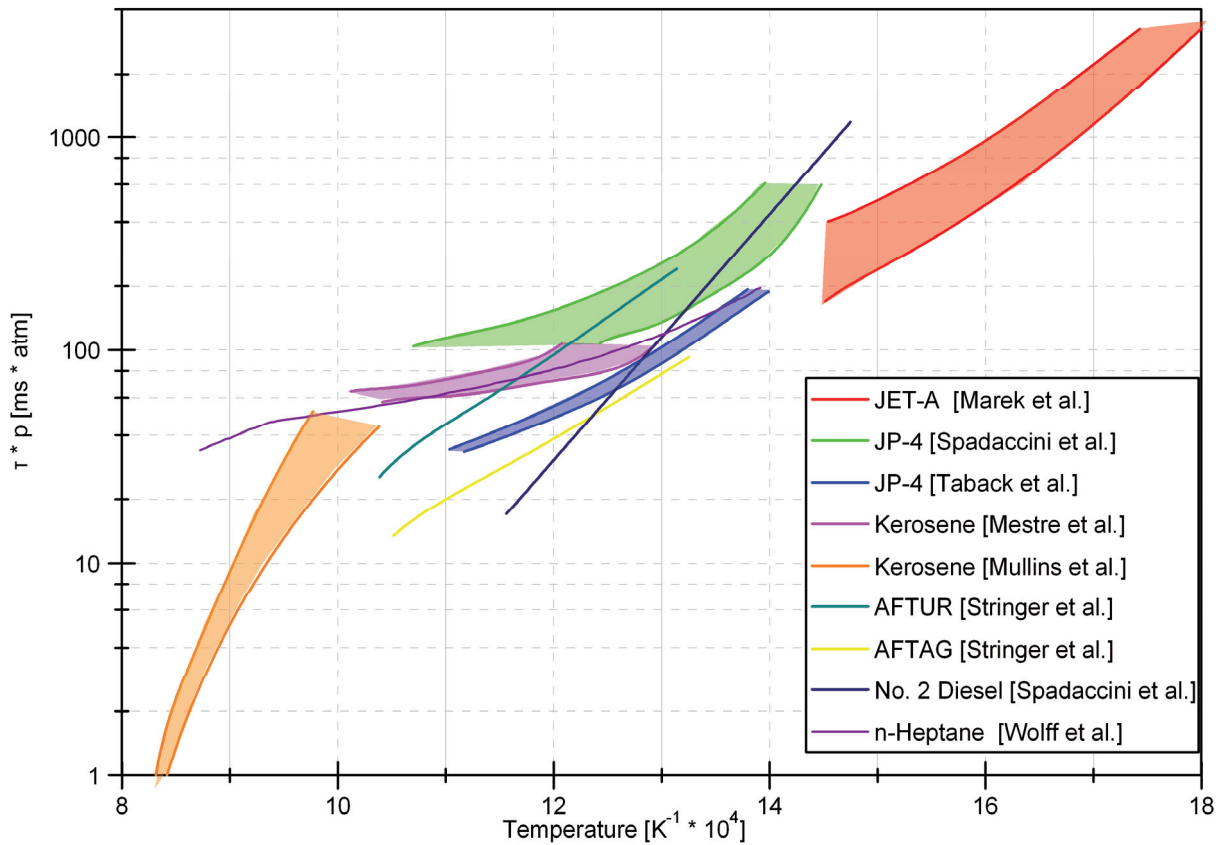


**Figure 1.6** – Results from various autoignition experiments [6, 9-15]

The results of the above works were often presented in the form of an Arrhenius type relationship of the form:

$$\tau = \frac{A}{p^n} e^{\frac{E_a}{R_u T}} \quad (1.1.1)$$

where  $A$  and  $n$  are empirical constants. While  $n$  was reported to range between 0.7 and 2 in many papers preceding the Spadaccini – TeVelde work, the latter reported a value of 2 [6], which has been adopted in many other works since.

The  $A$  constant on the other hand has varied very widely over many of the published results. This is due to the strong dependence of the results on the experimental apparatus employed. In heated air stream experiments, the fuel injection and fuel temperature (i.e. spray characteristics); size and configuration of the wind tunnel (boundary layer effects) and general measurement techniques (detection of ignition), all play an important role in the autoignition behaviour and the subsequent quantification of the induction time. All of these factors have to be controlled as tightly as possible, so that a clear distinction between the influencing parameters can be made.

## 1.2 Objective

The objective of this work is to shed some more light on the processes involved in spray autoignition. To this end results from the Center of Applied Space Technology and Microgravity (ZARM) Closed Vessel Simulation (CVS), which describes a monodisperse equidistant spray (see section 2.3) are compared with experiments conducted at the hot wind tunnel (HWK), which provides flows similar to those found in current and future combustion machines.

This work represents the next step in the development of a complete numerical description of the spray autoignition process, as the CVS was already compared to single droplet microgravity and ground test experiments [5, 29-32].

A roadmap of the development efforts towards a complete spray ignition simulation can be seen in Figure 1.7, which represents the research efforts of various workers in the ZARM combustion group over a period of more than 10 years. Initially, single droplet ignition experiments were conducted and a single droplet ignition simulation was developed. In order to be able to observe the droplet in the experiments, it had to be quite large. This meant that it is highly influenced by natural convection and other gravity dependent parameters. As a consequence many experiments were conducted under micro-gravity ( $\mu$ -g) conditions in the ZARM drop tower, eliminating gravity and supplying an observable but spherically symmetric droplet, which could then be compared to the one-dimensional spherically symmetric simulation. Once the simulation was validated against the  $\mu$ -g experiments with large droplets it could also be used to simulate small droplets of technical dimension (few to tens of micrometers).

The final and still ongoing steps are the development of a single droplet simulation with variable gas boundary conditions and the connection of this information with characteristic trajectories of single droplets from a CFD simulation, leading to a complete spray ignition simulation.

As an intermediate step, the present work compares the first complete spray experiments with single droplet simulations from the CVS. Initially, only one single droplet simulation was compared to the experiments, which is in essence a comparison of a monodisperse equidistant spray with a real spray ignition. Later several thousand single droplet simulations of different initial diameter were combined to provide a polydisperse equidistant spray simulation.

Since this was the first operational campaign of the HWK, the details of experimental facility and the requirements for its successful operation will be highlighted in section 3.

In addition to comparing the experimental results to the numerical ones, the experiments will also be compared and contrasted to earlier experimental efforts by other researchers for validation purposes.

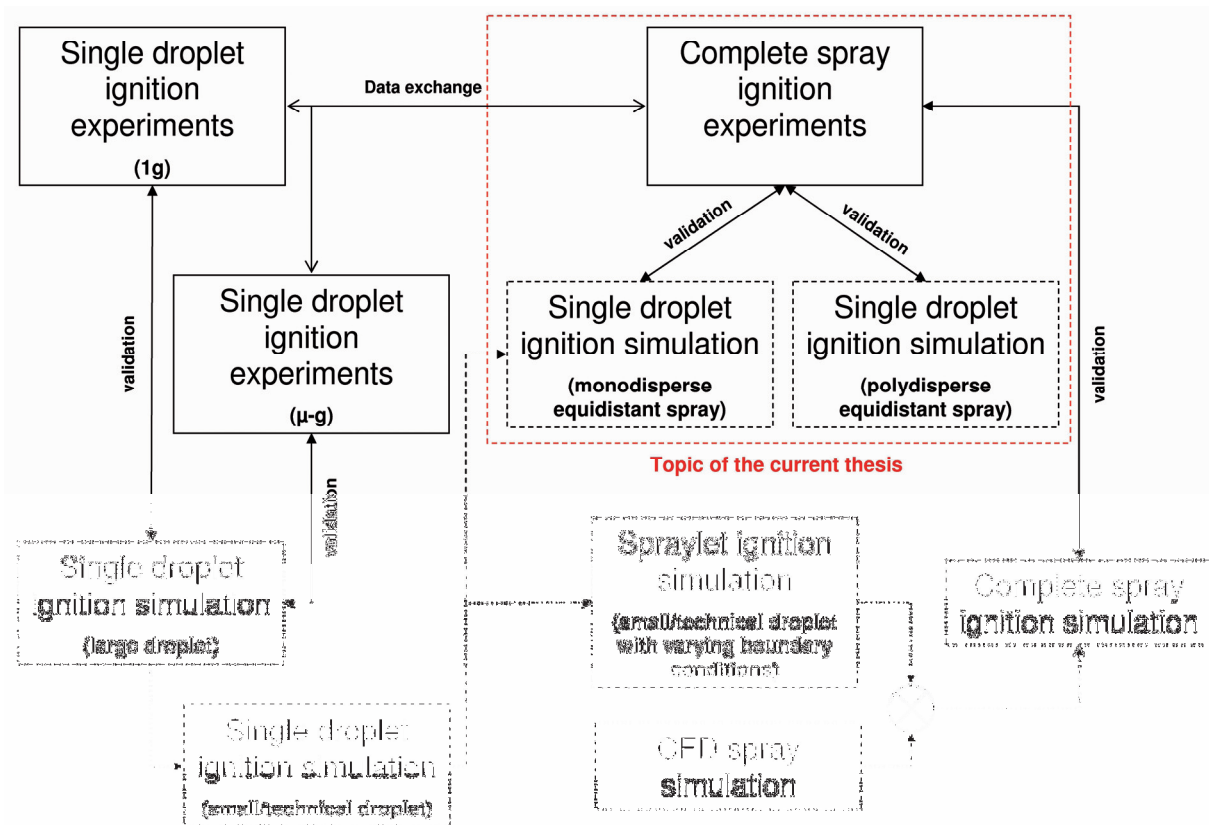


Figure 1.7 – Roadmap to a full spray ignition description

Prior to the discussion of the results (section 4) and the description of the HWK, the reader will be introduced to the theoretical background of the three main topics, which are crucial in the understanding of the experiments.

First, there is the theory governing the generation of a high temperature/pressure flow in the HWK. Once an understanding of this flow is reached, the next step is the introduction of a fuel jet into such a flow, and which mechanisms lead to the generation of a spray from the fuel jet. Finally, the processes that happen in the spray from the point of injection to ignition, with respect to a single droplet (as appropriate to the CVS) will be highlighted.

In the last section of this work (section 5) the results will be summarised and conclusions will be drawn. In addition to this an outlook for the conduction of future work and experiments will be given.

## 2 Theoretical Background

### 2.1 Flow in a Ludwieg – Tube

#### 2.1.1 Introduction

The Ludwieg – tube is a high Reynolds number wind tunnel that was developed by Hubert Ludwieg in 1955 in a response to a competition for a low cost – high Reynolds number wind tunnel. A Ludwieg – tube is a modification of the well known shock tube [33]. As such the Ludwieg – tube also possesses a converging-diverging nozzle, having sonic flow at its throat and supersonic flow downstream of the throat. This enables tight control of the mass flow and consequently flow velocity in the high pressure region.

A comparison between the two is sketched in Figure 2.1. In both cases a high and low pressure region are separated by a diaphragm or a very fast acting valve. The high pressure region is usually called “driver section”, while the low pressure region is known as the “driven section”. The gas in the two chambers can also be of different temperature and/or chemical composition in order to modify the flow conditions that ensue after the removal of the separation [33].

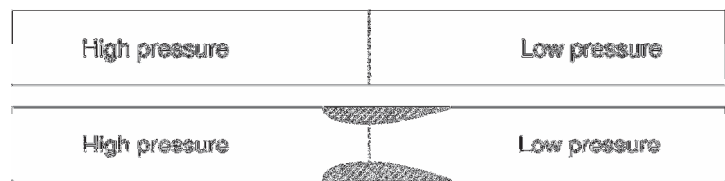


Figure 2.1 – Shock tube (top), Ludwieg – tube (bottom)

Once the separation is removed an expansion wave propagates into the driver section, while a normal shock wave propagates into the driven section. The established wave system behaves according to the laws of unsteady wave motion. The laws of unsteady wave motion apply to both shock tubes and Ludwieg – tubes. In between regions of wave motion the flow will behave according to the isentropic flow relations. Hence, the following section will first briefly review the flow in the isentropic flow regime and then elaborate upon this to also include the laws of unsteady wave motion for the description of the transient behaviour of the flow in a Ludwieg – Tube. The understanding of this behaviour is vital for the later interpretation of the experimental results presented in section 4.

#### 2.1.2 Isentropic Flow Relations

The flow in a Ludwieg – Tube can be treated as quasi-one-dimensional, meaning that while there is a change in cross-sectional area the flow variations are only considered in one dimension, assuming that the variations in  $y$  and  $z$  directions are small compared to the overall flow parameters in the  $x$  direction. This assumption is only valid if the change in cross-section is gradual.

Hence, first pure one-dimensional flow is considered and this is then extended upon to include quasi-one-dimensional flow.

The situation described above is schematically represented in Figure 2.2. The flow enters a domain (1) and is subject to some arbitrary change as it passes into region 2. In the case of one-dimensional flow areas one and two are equal.

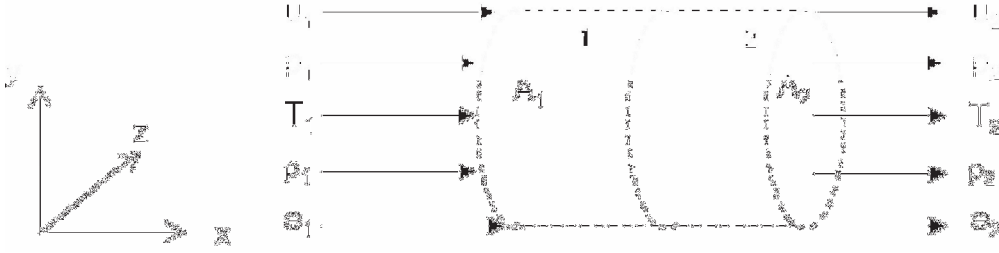


**Figure 2.2** – Schematic of one – dimensional flow

Hence continuity, momentum and energy (respectively), are described by:

$$-\oint_S \rho \mathbf{V} \cdot d\mathbf{S} = \frac{\partial}{\partial t} \iiint_{\mathcal{V}'} \rho d\mathcal{V}' \quad (2.1.1)$$

$$\oint_S (\rho \mathbf{V} \cdot d\mathbf{S}) \mathbf{V} + \iiint_{\mathcal{V}'} \frac{\partial(\rho \mathbf{V})}{\partial t} d\mathcal{V}' = \iiint_{\mathcal{V}'} \rho \mathbf{F} d\mathcal{V}' - \oint_S p d\mathbf{S} \quad (2.1.2)$$

$$\iiint_{\mathcal{V}'} \dot{q} \rho d\mathcal{V}' - \oint_S p \mathbf{V} \cdot d\mathbf{S} + \iiint_{\mathcal{V}'} \rho (\mathbf{F} \cdot \mathbf{V}) d\mathcal{V}' = \iiint_{\mathcal{V}'} \frac{\partial}{\partial t} \left[ \rho \left( e + \frac{V^2}{2} \right) \right] d\mathcal{V}' + \oint_S \rho \left( e + \frac{V^2}{2} \right) \mathbf{V} \cdot d\mathbf{S} \quad (2.1.3)$$

But since body forces can be neglected and the flow is considered steady (i.e. not changing with time), the above reduces to:

$$-\oint_S \rho \mathbf{V} \cdot d\mathbf{S} = 0 \quad (2.1.4)$$

$$\oint_S (\rho \mathbf{V} \cdot d\mathbf{S}) \mathbf{V} = -\oint_S p d\mathbf{S} \quad (2.1.5)$$

$$\iiint_{\mathcal{V}'} \dot{q} \rho d\mathcal{V}' - \oint_S p \mathbf{V} \cdot d\mathbf{S} = \oint_S \rho \left( e + \frac{V^2}{2} \right) \mathbf{V} \cdot d\mathbf{S} \quad (2.1.6)$$

These can be integrated to yield the basic equations for steady one-dimensional flow (note the definition of enthalpy  $h = e + p/\rho$  and  $A_1 = A_2$ ):

$$\rho_1 u_1 = \rho_2 u_2 \quad (2.1.7)$$

$$p_1 + \rho_1 u_1^2 = p_2 + \rho_2 u_2^2 \quad (2.1.8)$$

$$h_1 + \frac{u_1^2}{2} + q = h_2 + \frac{u_2^2}{2} \quad (2.1.9)$$

From these equations the main isentropic flow relations can be derived, specifically the energy equation (2.1.9) can be modified if one assumes no heat addition and a perfect gas ( $h = c_p T$ ).

$$c_p T_1 + \frac{u_1^2}{2} = c_p T_2 + \frac{u_2^2}{2} \quad (2.1.10)$$

Now, if the flow were to be brought to rest adiabatically, then  $u_2 = 0$ . Further by defining  $T_1 = T$ ,  $T_2 = T_0$  and  $u_1 = u$  equation (2.1.10) becomes:

$$c_p T + \frac{u^2}{2} = c_p T_0 \quad (2.1.11)$$

$T_0$  then represents the total temperature if the flow were to be brought to rest and its kinetic energy were to be transformed into thermal energy without any losses. The subscript 0 in this case denotes total or stagnation conditions.

Under the further assumption that the flow is isentropic, the following relations apply [33]:

$$c_p = \frac{\kappa R}{\kappa - 1} \quad (2.1.12)$$

$$c_v = \frac{R}{\kappa - 1} \quad (2.1.13)$$

$$a = \sqrt{\kappa R T} \quad (2.1.14)$$

equation (2.1.11) becomes:

$$\frac{T_0}{T} = 1 + \frac{\kappa - 1}{2} M^2 \quad (2.1.15)$$

And since the process is isentropic, it follows that:

$$\frac{p_0}{p} = \left( 1 + \frac{\kappa - 1}{2} M^2 \right)^{\frac{\kappa}{\kappa - 1}} \quad (2.1.16)$$

$$\frac{\rho_0}{\rho} = \left( 1 + \frac{\kappa - 1}{2} M^2 \right)^{\frac{1}{\kappa - 1}} \quad (2.1.17)$$

Equations (2.1.15) through (2.1.17) relate the stagnation condition in any isentropic flow field to the flow conditions. In a Ludwieg – tube however there are also variations of the cross section of the wind-tunnel, hence the assumption that  $A_1 = A_2$  in Figure 2.2 is no longer valid. In order to still be able to incorporate these changes of cross-section into this model, one has to turn to quasi-one-dimensional flow. As was explained, in this approximate model of the flow, it is assumed that the variations of the flow variables along the  $y$  and  $z$ -coordinates are small in comparison to the general flow direction. As such quasi-one-dimensional flow assumes that the flow conditions are the same over an entire area at a specific  $x$ -coordinate.

Although this is an approximate model, it is important to note, that the approximation is made in the physical model, not the equations now following. These fully account for all flow parameters and hence quasi-one-dimensional isentropic flow in essence represents an “average” value of the flow condition variations at any given  $x$  station.

Similarly, with the assumption of quasi-one-dimensional flow equations (2.1.1) through (2.1.3) reduce to:

$$\rho_1 u_1 A_1 = \rho_2 u_2 A_2 \quad (2.1.18)$$

$$p_1 A_1 + \rho_1 u_1^2 A_1 + \int_{A_1}^{A_2} p dA = p_2 A_2 + \rho_2 u_2^2 A_2 \quad (2.1.19)$$

$$h_1 + \frac{u_1^2}{2} = h_2 + \frac{u_2^2}{2} \quad (2.1.20)$$

These can also be stated in differential forms, so in the case of continuity [33]:

$$d(\rho u A) = 0 \quad (2.1.21)$$

In the case of momentum all second-order terms can be ignored, because their overall contribution is very small:

$$\rho u^2 dA + \rho u A du + A u^2 d\rho = 0 \quad (2.1.22)$$

And finally in the case of energy:

$$dh + u du = 0 \quad (2.1.23)$$

From these and the assumption that the flow is isentropic, two very important flow relations can be derived; the first is the Euler equation, which is the fluid dynamical equivalent to Newton's second law:

$$dp = -\rho u du \quad (2.1.24)$$

The second being the area velocity relationship:

$$\frac{dA}{A} = (M^2 - 1) \frac{du}{u} \quad (2.1.25)$$

The area velocity relationship is of major importance as it highlights a peculiarity of supersonic compressible flow. By inspection of equation (2.1.25), when  $M < 1$  the flow velocity increases with a decrease of area, as was expected from incompressible flow. However when  $M > 1$  the situation is exactly reversed, an increase in area leads to a flow velocity increase, while a decrease in velocity is achieved, with a decrease in area. The limiting case being  $M = 1$ , in this case the area has a minimum; hence the flow velocity in the smallest cross-section of a duct also known as throat is always exactly sonic (provided the pressure ratio is sufficient, see equation (2.1.16) when  $M=1$ , this is the minimum pressure ratio for sonic/supersonic flow). This explains the configuration of any supersonic nozzle as convergent – divergent [33].

From the above equation a relationship can be derived, which relates the throat area  $A^*$  to the other areas of the tube and the corresponding Mach number (assuming choked i.e.  $M=1$  at  $A^*$ , flow):

$$\frac{A}{A^*} = \frac{1}{M} \left( \frac{2 + (\kappa - 1) M^2}{\kappa + 1} \right)^{\frac{\kappa + 1}{2(\kappa - 1)}} \quad (2.1.26)$$

Although difficult to see because equation (2.1.26) is implicit, there are always two mach numbers for any one corresponding area ratio; one supersonic and one subsonic, corresponding to the down- and upstream positions with respect to the throat.

This completes this brief review of isentropic flow relations, as equation (2.1.26) and (2.1.15) through (2.1.17), allow the complete treatment of the steady flow conditions in a Ludwieg tube, as quasi-one-dimensional flow.

It should be noted that above relations are only valid in between regions of unsteady wave motion, as the initial assumption in the derivation of the isentropic flow relations was steady flow.

The following section will show that initially four distinct regions of flow are established in a shock tube (see Figure 2.3), the first one being in between the first end-wall of the tube and a normal shock wave, the second between the downstream side of the shock and a contact surface, the third region is generated between the contact surface and the head of an expansion wave, and finally the fourth region between the head of the expansion wave and the second end-wall of the tube. The isentropic flow-relations are only valid within these regions, *not* across them, as the flow is unsteady across these regions.

### 2.1.3 Establishment of the Wave System

As was explained in the previous section a wave system is established in the shock tube, this is depicted in Figure 2.3.

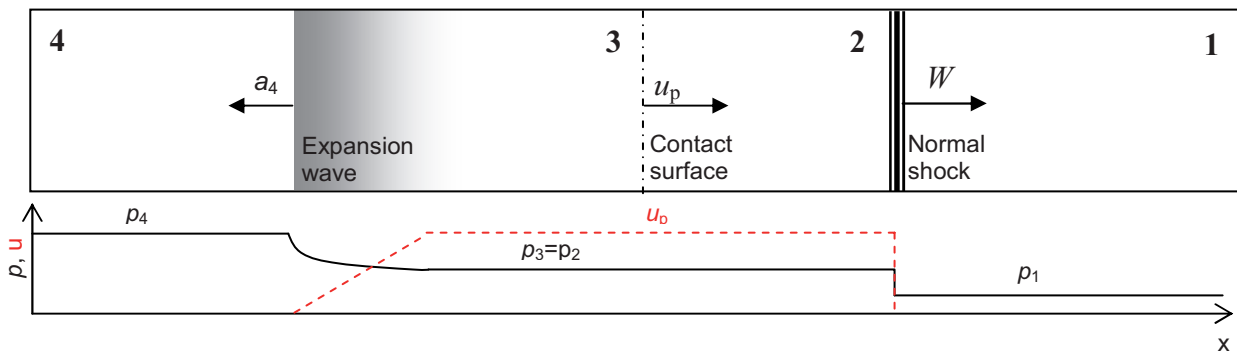


**Figure 2.3** – Established wave system in a shock tube after the removal of the separation

As can be seen the expansion wave moves into the high pressure region (4) and over the expansion wave the pressure drops smoothly to a new pressure level that is established between the expansion wave and the shock. The flow in this region moves in the direction of the normal shock with the velocity of the contact surface,  $u_p$ . It is important to note, that while pressure and velocity are maintained across the interface between region two and three (as can be seen in Figure 2.3) enthalpy changes discontinuously. Hence, the isentropic flow relations are *not* valid across the contact surface, as was mentioned above [33].

Because of this enthalpy change across the contact surface, it is best to treat the wave system in a shock tube as two parts, one region (1 and 2) governed by the normal shock, and the other (3 and 4) governed by the expansion wave. While the conditions in regions 1 and 4 are known form the initial conditions.

The HWK is designed in such a way that the experiment is conducted in region 3 after the expansion wave has passed.

### 2.1.4 Moving Normal Shock

The shock wave depicted in Figure 2.3 moves into a region of stagnant air and induces a velocity behind it. This situation is equivalent to a stationary normal shock that is kept in place by the flow approaching it with a velocity equalling its forward movement (such as in an overexpanded supersonic nozzle for example) and the flow behind the shockwave receding with a velocity equal to its velocity minus the induced flow velocity (see Figure 2.3):

$$W = u_1 \quad (2.1.27)$$

$$W - u_p = u_2 \quad (2.1.28)$$

This is an important change of perspective, as the flow from the point of view of moving coordinates has become quasi-steady. Hence, from the moving-observers perspective the one-dimensional flow equations from section 2.1.2 apply, rewritten here for convenience:

$$\rho_1 u_1 = \rho_2 u_2 \quad (2.1.29)$$

$$p_1 + \rho_1 u_1^2 = p_2 + \rho_2 u_2^2 \quad (2.1.30)$$

$$h_1 + \frac{u_1^2}{2} = h_2 + \frac{u_2^2}{2} \quad (2.1.31)$$

By substitution of (2.1.27) and (2.1.28) into (2.1.29) through (2.1.31) and algebraic manipulation the Hugoniot equation can be derived:

$$e_2 - e_1 = \frac{p_1 + p_2}{2} \left( \frac{1}{\rho_1} - \frac{1}{\rho_2} \right) \quad (2.1.32)$$

Equation (2.1.32) is very useful as it relates only thermodynamic properties across a normal shock wave and is valid to both a moving and a stationary normal shock.

Under the special case of a calorically perfect gas the Hugoniot equation can be solved to relate pressure and temperature and consequently also pressure and density across a moving normal shock wave:

$$\frac{T_2}{T_1} = \frac{p_2}{p_1} \left( \frac{\frac{\kappa+1}{\kappa-1} \frac{p_2}{p_1}}{1 + \frac{\kappa+1}{\kappa-1} \frac{p_2}{p_1}} \right) \quad (2.1.33)$$

$$\frac{\rho_2}{\rho_1} = \frac{1 + \frac{\kappa+1}{\kappa-1} \frac{p_2}{p_1}}{\frac{\kappa+1}{\kappa-1} + \frac{p_2}{p_1}} \quad (2.1.34)$$

Where (in the case of a calorically perfect gas):

$$c_p - c_v = R \quad (2.1.35)$$

$$\kappa = \frac{c_p}{c_v} \quad (2.1.36)$$

As was explained, a moving shock can be treated as a stationary normal shock, if one considers the moving observer perspective. In a normal stationary shock the pressure ratio across the shock is given by:

$$\frac{p_2}{p_1} = 1 + \frac{2\kappa}{\kappa+1}(M^2 - 1) \quad (2.1.37)$$

And the Mach number of the shock will be given by:

$$M_s = \frac{W}{a_1} \quad (2.1.38)$$

Hence, from the moving coordinates:

$$W = a_1 \sqrt{\frac{\kappa+1}{2\kappa} \left( \frac{p_2}{p_1} - 1 \right) + 1} \quad (2.1.39)$$

The velocity induced behind the moving shock in Figure 2.3 can now be derived through the use of equations (2.1.29), (2.1.28), (2.1.34) and (2.1.39):

$$u_p = \frac{a_1}{\kappa} \left( \frac{p_2}{p_1} - 1 \right) \left( \frac{\frac{2\kappa}{\kappa+1}}{\frac{p_2}{p_1} + \frac{\kappa-1}{\kappa+1}} \right)^{\frac{1}{2}} \quad (2.1.40)$$

As can be seen the induced velocity behind a moving shockwave can be calculated only by knowing the pressure ratio across the shock, the gas properties and the speed of sound ahead of the shock. From the above equations all other thermodynamic properties across a moving shock can be calculated. The fundamental difference between moving and stationary shocks, should however not be forgotten, which is that in an unsteady adiabatic inviscid flow the total enthalpy is not constant [33]. This can easily be seen when examining a variant of the energy equation:

$$\rho \frac{Dh_0}{Dt} = \frac{\partial p}{\partial t} \quad (2.1.41)$$

Since the flow is unsteady there is a change of pressure with respect to time and hence  $dp/dt \neq 0$ , which in turn means that  $h_0$ , cannot be constant.

### 2.1.5 Finite Nonlinear Waves

The second wave shown in Figure 2.3 is an expansion wave that propagates into the high pressure region (denoted by 4 in the figure) and leaves a region of reduced pressure in its wake (denoted 3).

This wave is similar to a sound wave in that its head always moves into the gas ahead of it with the local speed of sound, but in contrast to a sound wave, this wave is a strong wave. As a consequence the main assumption in acoustic theory that any perturbation is small is no longer valid and acoustic theory is not applicable to finite nonlinear waves. The following tables compares and contrasts the differences between sound- and finite waves [33].

<i>Sound wave</i>	<i>Finite wave</i>
Perturbations ( $\Delta p$ , $\Delta T$ , $\Delta \rho$ etc.) are small	Perturbations ( $\Delta p$ , $\Delta T$ , $\Delta \rho$ etc.) are large
All parts of the wave move at $a_\infty$	Each part of the wave moves at local velocity $u + a$
Wave shape is constant	Wave shape is a function of time
Linear equations govern flow variables	Full nonlinear equations govern flow variables
Ideal situation (closely approximated by sound waves)	Non-idealised situation (valid for all real wave)

**Table 2.1** – Comparison between sound- and finite waves

The treatment of finite waves starts by considering the continuity equation in its full three-dimensional form as a substantial derivative:

$$\frac{D\rho}{Dt} + \rho(\nabla \cdot \mathbf{V}) = 0 \quad (2.1.42)$$

Where the substantial derivative is defined as:

$$\frac{D}{Dt} \equiv \frac{\partial}{\partial t} + u \frac{\partial}{\partial x} + v \frac{\partial}{\partial y} + w \frac{\partial}{\partial z} = \frac{\partial}{\partial t} + (\mathbf{V} \cdot \nabla) \quad (2.1.43)$$

The first term in equation (2.1.42) describes the local fluid elements change of density over time – hence in this case the flow is treated as unsteady, very much in contrast to the isentropic flow relations presented in section 2.1.2.

Since density is a function of both pressure and entropy one can write:

$$\begin{aligned} \rho &= \rho(p, s) \\ d\rho &= \left( \frac{\partial \rho}{\partial p} \right)_s dp + \left( \frac{\partial \rho}{\partial s} \right)_p ds \end{aligned} \quad (2.1.44)$$

If the flow is now assumed to be isentropic  $ds = 0$  and equation (2.1.44) simplifies to:

$$d\rho = \left( \frac{\partial \rho}{\partial p} \right)_s dp$$

Recalling the basic definition of the speed of sound for isentropic flow from thermodynamics:

$$a^2 = \left( \frac{\partial p}{\partial \rho} \right)_s \quad (2.1.45)$$

Hence, employing the above definition and the definition for the substantial derivative (2.1.43), it follows that:

$$\frac{D\rho}{Dt} = \frac{1}{a^2} \frac{Dp}{Dt} \quad (2.1.46)$$

Finally combining equations (2.1.42) and (2.1.46) gives the variation of the main flow parameters pressure and density in a finite wave.

$$\frac{1}{a^2} \frac{Dp}{Dt} + \rho(\nabla \cdot \mathbf{V}) = 0 \quad (2.1.47)$$

In addition to this, another equation is necessary for the full description of the flow in a finite wave, hence taking the momentum equation:

$$\rho \frac{D\mathbf{V}}{Dt} + \nabla p = 0 \quad (2.1.48)$$

In the case of a shock tube the flow can essentially be treated as one-dimensional (Figure 2.3), so equations (2.1.47) and (2.1.48) can be simplified as follows (respectively):

$$\frac{1}{a^2} \left( \frac{\partial p}{\partial t} + u \frac{\partial p}{\partial x} \right) + \rho \frac{\partial u}{\partial x} = 0 \quad (2.1.49)$$

$$\frac{1}{a\rho} \left( \frac{\partial p}{\partial t} + u \frac{\partial p}{\partial x} \right) + a \frac{\partial u}{\partial x} = 0 \quad (2.1.50)$$

$$\frac{\partial u}{\partial t} + u \frac{\partial u}{\partial x} + \frac{1}{\rho} \frac{\partial p}{\partial x} = 0 \quad (2.1.51)$$

The above equations completely describe the flow field in a one-dimensional isentropic finite wave. These equations can be solved through various methods, one of the most famous of which is the method of characteristics. This method will be briefly discussed in the following section.

## 2.1.6 Method of Characteristics

Considering the wave system depicted in Figure 2.3; before the diaphragm is broken there are two regions with different conditions. This situation is also depicted in Figure 2.4 as the initial time  $t_0$ . Once the diaphragm is removed, a shockwave will propagate into the low pressure region, raising the pressure behind it to a prescribed level (section 2.1.4), while an expansion wave will propagate into the high pressure region and lower the pressure in its wake ( $t_1$  in Figure 2.4).

As is shown in Figure 2.4, the head and tail of the expansion wave diverge, while the shockwave remains an infinitesimal disturbance. The reason for this lies in the nature of the waves. Through raising the pressure behind it, the shockwave also induces a temperature increase behind it. This in turn causes the speed of sound behind the shockwave to increase and any following disturbance will tend to coalesce into the shockwave, hence maintaining its finite defined structure. The head of the expansion wave on the other hand, induces a pressure and temperature reduction, and hence any lagging disturbance will move more slowly as the speed of sound behind the leading wave is reduced. This leads to the spreading of the wave as depicted in Figure 2.4, also known as expansion wave fanning [33].

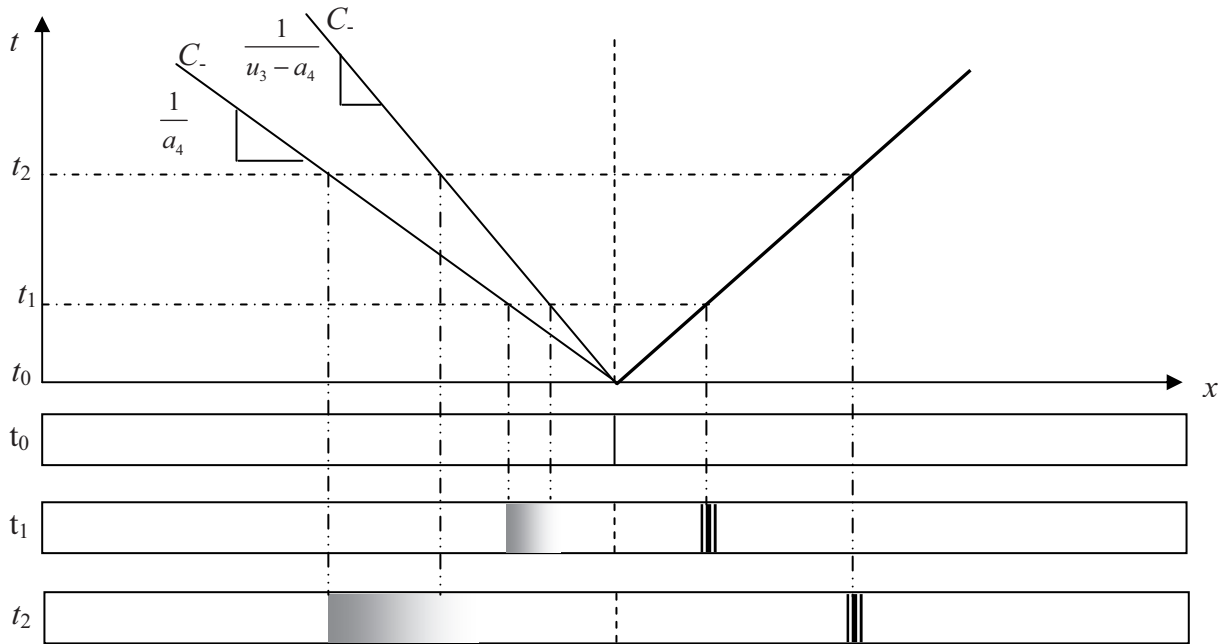


**Figure 2.4** – Wave movement in the x-t plane

Considering this physical picture of the finite wave further, a physical explanation for a “characteristic line” can be obtained. A hypothetical observer, moving with the head of the expansion wave through the stagnant gas ahead of the wave (region 4 in Figure 2.3) would always “see” the flow approaching with the speed of sound and see the flow receding behind the wave with some velocity less than the speed of sound. The velocity reduction would be characteristic for this portion of the wave and would remain constant (unless the conditions ahead of the wave change).

A mathematical description for this can be obtained by adding (or subtracting) equations (2.1.50) and (2.1.51):

$$\left[ \frac{\partial u}{\partial t} + (u + a) \frac{\partial u}{\partial x} \right] + \frac{1}{\rho a} \left[ \frac{\partial p}{\partial t} + (u + a) \frac{\partial p}{\partial x} \right] = 0 \quad (2.1.52)$$

$$\left[ \frac{\partial u}{\partial t} + (u - a) \frac{\partial u}{\partial x} \right] + \frac{1}{\rho a} \left[ \frac{\partial p}{\partial t} + (u - a) \frac{\partial p}{\partial x} \right] = 0 \quad (2.1.53)$$

These two equations describe both velocity and pressure as a function of time and position. So any arbitrarily small change in velocity or pressure with respect to position and time would be represented by:

$$du = \frac{\partial u}{\partial t} dt + \frac{\partial u}{\partial x} dx \quad (2.1.54)$$

$$dp = \frac{\partial p}{\partial t} dt + \frac{\partial p}{\partial x} dx \quad (2.1.55)$$

But from our previous thought experiment as observer on the wave, it was shown that there can be lines with characteristic changes in these entities and that in this example these are represented as a straight line with the slope of  $1/(u-a)$  (see figure Figure 2.4):

$$dx = (u - a) dt \quad (2.1.56)$$

Hence the combination of equations (2.1.52) through (2.1.56), leads to the following expressions:

$$du - \frac{dp}{\rho a} = 0 \quad (2.1.57)$$

$$du + \frac{dp}{\rho a} = 0 \quad (2.1.58)$$

These are called the compatibility equations for the characteristic line and they hold *only* along the  $C_-$  and  $C_+$  characteristics (respectively) shown in Figure 2.4. The result is nonetheless significant, because the partial differential equations (2.1.52) and (2.1.53) have been reduced to ordinary differential equations and can hence be solved in closed forms.

The integration results of the above compatibility equations are called the Riemann invariants [33]:

$$J_- = u - \int \frac{dp}{\rho a} = const. \quad (2.1.59)$$

$$J_+ = u + \int \frac{dp}{\rho a} = const. \quad (2.1.60)$$

Under the assumption of a calorically perfect gas and isentropic flow, these integrals can be shown to result in the two main equations for the method of characteristics.

$$J_- = u - \frac{2a}{\kappa - 1} = const. \quad (2.1.61)$$

$$J_+ = u + \frac{2a}{\kappa - 1} = const. \quad (2.1.62)$$

The two above equations are of major importance to flow problems in unsteady wave motion as shown in Figure 2.4. If the values of the Riemann invariants  $J_+$  and  $J_-$  is known at any point in the  $x-t$  plane equations (2.1.61) and (2.1.62) will give the values of  $a$  and  $u$  for this point in the flow field through:

$$a = \frac{\kappa - 1}{4} (J_+ - J_-) \quad (2.1.63)$$

$$u = \frac{1}{2} (J_+ + J_-) \quad (2.1.64)$$

This can now be applied to the flow shown in Figure 2.4. As the Riemann invariants are always constant along one characteristic. Hence a hypothetical  $C_+$  characteristics (right running) passing through the wave flow field of the wave shown in Figure 2.4 always carries the same Riemann invariant value. Hence any Riemann invariant in an arbitrary region in the wave must be equal to the Riemann invariant value of region 4 (in Figure 2.3) if one follows a  $C_+$  characteristic:

$$u_4 + \frac{2a_4}{\kappa-1} = u + \frac{2a}{\kappa-1}$$

But the flow in region 4 is at rest, so  $u_4=0$  and hence:

$$\frac{a}{a_4} = 1 - \frac{\kappa-1}{2} \left( \frac{u}{a_4} \right) \quad (2.1.65)$$

Finally with the definition of the speed of sound (see equation (2.1.14)) and under the assumption of isentropic flow, all conditions throughout the wave can be calculated by equation (2.1.65) and the following relationships:

$$\frac{T}{T_4} = \left[ 1 - \frac{\kappa-1}{2} \left( \frac{u}{a_4} \right) \right]^2 \quad (2.1.66)$$

$$\frac{p}{p_4} = \left[ 1 - \frac{\kappa-1}{2} \left( \frac{u}{a_4} \right) \right]^{\frac{2\kappa}{\kappa-1}} \quad (2.1.67)$$

As can be seen the local flow conditions are referenced to conditions in region 4 and since the flow is stagnant in this region the ratio  $u/a_4$  can be replaced by Mach number [33].

$$\frac{T}{T_4} = \left[ 1 - \frac{\kappa-1}{2} (M) \right]^2 \quad (2.1.68)$$

$$\frac{p}{p_4} = \left[ 1 - \frac{\kappa-1}{2} (M) \right]^{\frac{2\kappa}{\kappa-1}} \quad (2.1.69)$$

The above is only valid as long as the flow is stationary in region 4, if this is not the case then the Mach number cannot be used as  $a_4 \neq a_0$  [33].

### 2.1.7 Shock Tube – Relations and Ludwieg – Tube Modification

With the tools of isentropic flow and unsteady wave motion (both expansion- and shockwave) it is possible to solve all initial regions in the flow-field of a shock tunnel and also expand this to the modification of a Ludwieg – Tube as shown in Figure 2.1.

Concentrating on the flow in a shock tube first, it is possible to relate the initial conditions of regions one and four (see Figure 2.3) to all flow parameters, ensuing when the diaphragm is removed. As the static pressure and velocity of the flow in region two and three are identical, equations (2.1.67) and (2.1.40) can be related to give an implicit relationship between the pressure ratios and speeds of sound of the four regions:

$$\frac{p_4}{p_1} = \frac{p_2}{p_1} \left[ 1 - \frac{(\kappa_4 - 1) \frac{a_1}{a_4} \frac{p_2}{p_1 - 1}}{\sqrt{2\kappa_1 \left( 2\kappa_1 + (\kappa_1 + 1) \frac{p_2}{p_1 - 1} \right)}} \right]^{\frac{-2\kappa_4}{\kappa_4 - 1}} \quad (2.1.70)$$

This allows the calculation of the strength of the resulting shock-wave and its corresponding pressure ratio, which in turn allows the determination of all properties behind the shock wave through the laws of moving shocks which were presented above.

Since the static pressures in region two and three are the same, the pressure ratio  $p_3/p_4$  is also known and with it the strength of the finite expansion wave. All properties inside the wave can then be calculated by using equations (2.1.65) and (2.1.69), while all properties behind the expansion wave can be determined using the isentropic flow relations. It is important to note that the wave equations are only valid in the region of  $a_4 \geq u \geq u_3$ , as the flow in this region is unsteady, while the flow in the region between the tail of the expansion wave and the contact surface is steady and hence has to be treated with the isentropic flow relations.

An example of the pressure development in a typical shock tube can be seen in Figure 2.5, in this case with an initial pressure ratio of about 2.35 to 1. At the time of diaphragm rupture, an expansion wave can be seen propagating to the left, while a compression wave is moving toward the right. The effect of expansion wave fanning (i.e. the spreading of the finite wave with time) is clearly visible as the expansion wave moves toward the left. It can also be seen that the head of the expansion wave is reflected on the left hand side wall and then passes through the rest of the wave. This region is known as a non-simple region as the wave passes through a region of changing conditions induced by its own trailing regions. The region where the wave propagates into a region of constant conditions is known as simple region. A non-simple region can nonetheless still be solved by the method of characteristics, by moving between small sections of the expansion wave and interpolating with straight line characteristics.

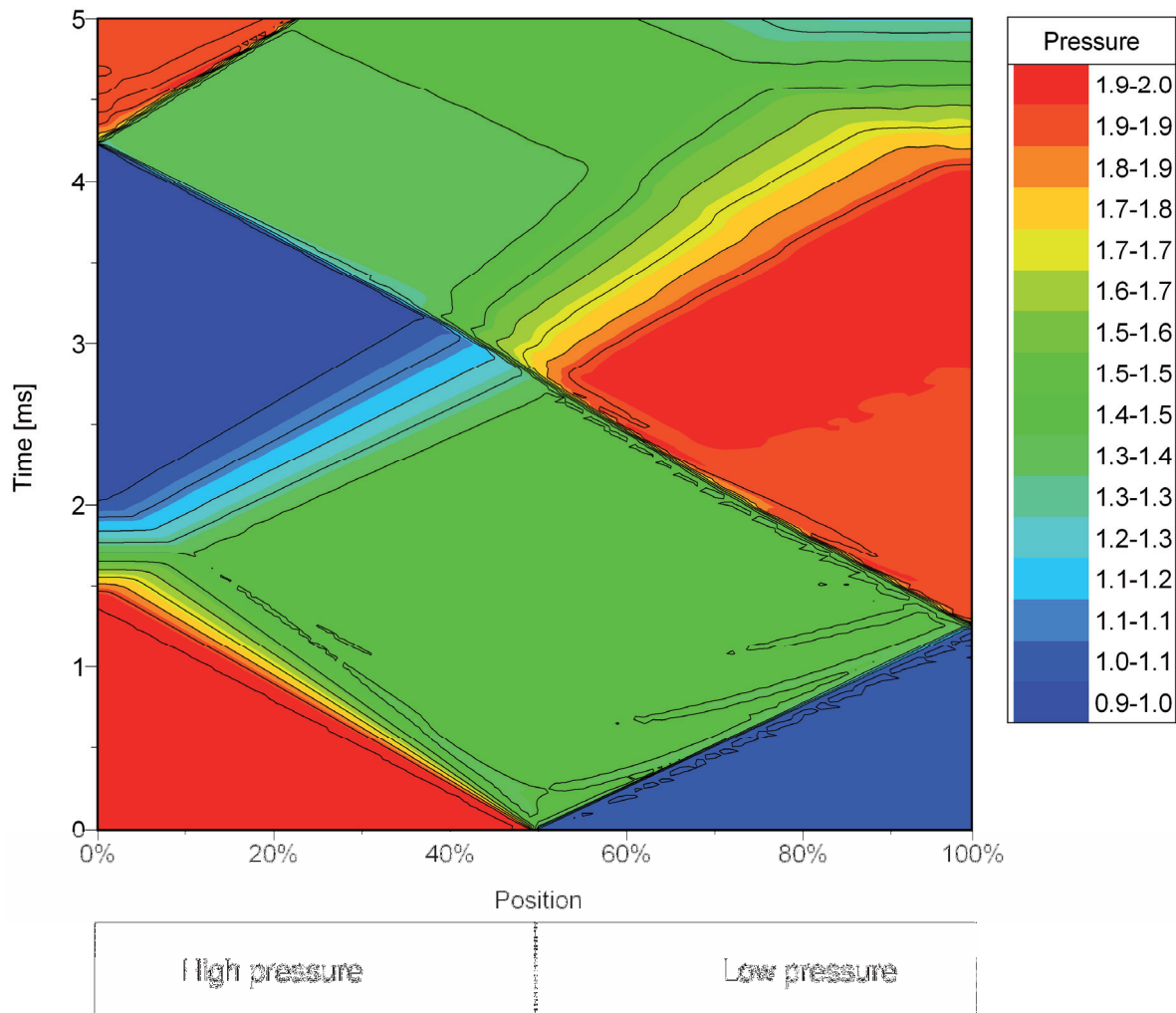
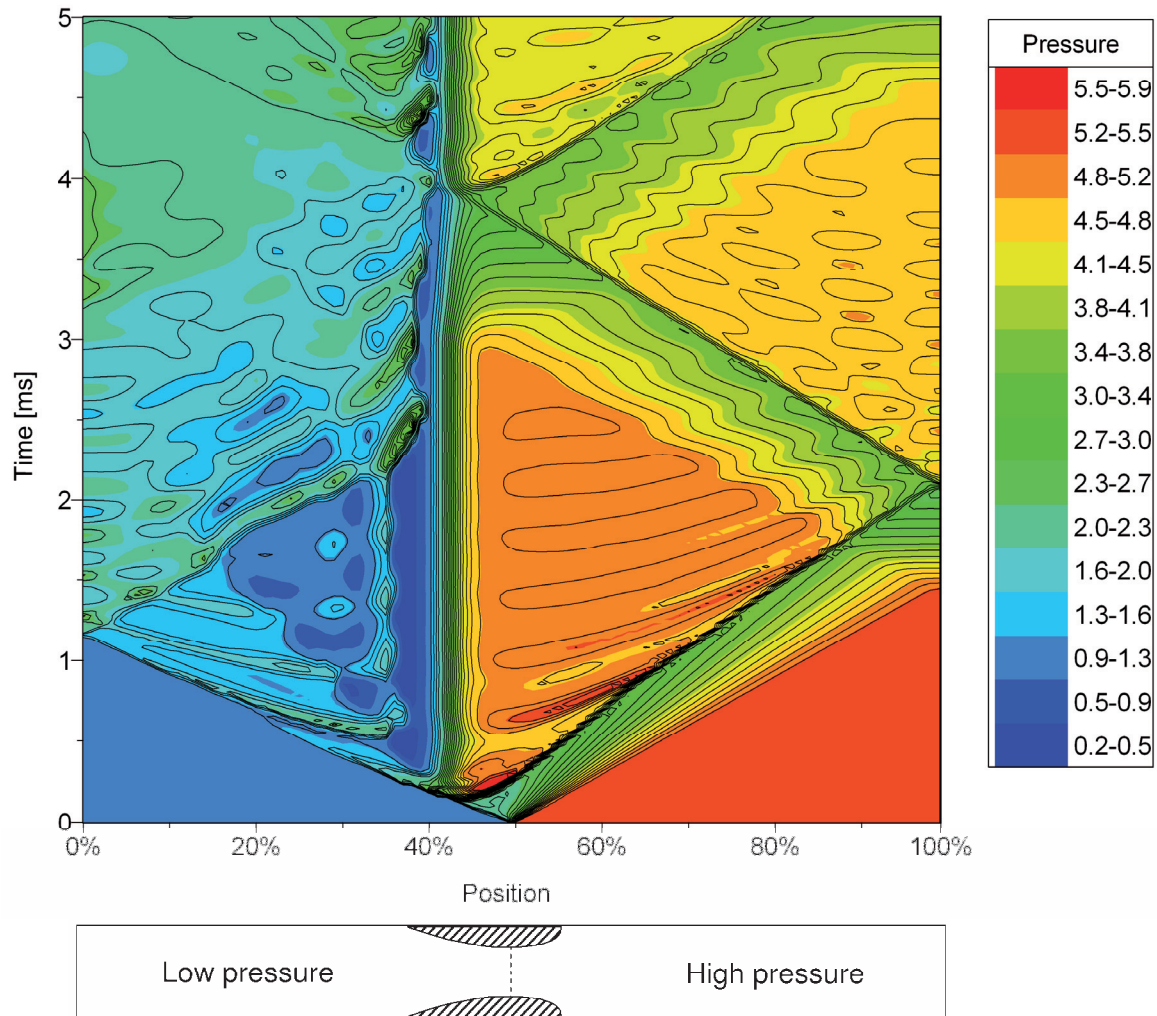


Figure 2.5 – Shock tube pressure development

The example shown in Figure 2.6, demonstrates the flow in a Ludwieg – tube as shown below the figure, in which the valve or diaphragm is slightly upstream of the nozzle (which is similar to the HWK configuration). As can be seen the initial behaviour is similar to a simple shock-tube in that an expansion and shockwave are formed. As the shockwave moves into the nozzle however it is partially reflected and follows the expansion wave at some distance. Behind this compression wave a plateau of relatively constant pressure is formed. This is where the experiments on induction time measurement take place. Another interesting feature that is visible in Figure 2.6, is the choking of the nozzle at approximately 0.25ms. As the flow in the throat can only reach a maximum of sonic velocity (if the pressure ratio is high enough;  $p_0/p \geq 1.89$ , for air – see equation(2.1.16)) the upstream conditions in the nozzle become independent of the downstream conditions. This can clearly be seen by the straight line with constant pressure at about 41% of the total length. This line only changes its direction as the reflected expansion wave in the high pressure region reaches the throat.

The shock wave in the low pressure region is reflected from the closed end and begins to travel upstream into the nozzle region. The flow velocity near the nozzle however, reaches high supersonic speeds and thus the shocks forward motion is stopped and it becomes a normal stationary shock in the exit plane of the nozzle. This is of course not the case in the HWK as it is open to the atmosphere and the shock is not reflected.



**Figure 2.6** – Ludwig Tube pressure development

This concludes the section on flow in a Ludwig – tube. With the above theory it is possible to treat most phenomena that will occur during the experiments of the HWK and hence this theory was used in the evaluation of the experimental data presented in section 4.

The next section will now treat the injection of a liquid fuel into the flow field generated and how a spray is formed as a consequence.

## 2.2 Description of a Spray

### 2.2.1 Introduction

One of the most crucial factors in spray ignition is the generation of the spray and the classification thereof, although the actual spray generation process is not subject to research in this project.

A spray can be generated through a number of different processes, which can be classified in four main categories and several subgroups:

1. Pressure atomizers
  - a. Plain orifice
  - b. Pressure-swirl (simplex)
  - c. Duplex
  - d. Dual orifice
  - e. Spill return
  - f. Fan spray
2. Rotary atomizers
  - a. Disk atomizer
  - b. Cup atomizer
3. Twin-fluid atomizers
  - a. Air-assist atomizers
  - b. Air-blast atomizers

As will be described in section 3.3.1 the injection configuration used in the HWK for this work is a plain orifice atomiser. The advantage of this type of atomiser is that it has a relatively simple geometry, and is cheap and rugged. It is often used in Diesel engines, jet engine afterburners and ramjets.

The disadvantage of plain orifice atomisers however is, that in order to generate a very fine spray, very small orifice diameters are needed (limited to 0.3mm to avoid clogging) and the injection pressure differential (with respect to ambient conditions) has to be quite high [34].

Ideally, one would like to measure all quantities associated with the spray so that a detailed analysis of the processes involved can be undertaken. The parameters of interest in this respect are:

- General liquid properties (e.g. density, viscosity, surface tension)
- Geometry of the injection nozzle
- Injection Pressure
- Temperature of the liquid
- Droplet size distribution
- Mean/average droplet size
- Ambient conditions into which the spray is injected

However, especially the droplet size distribution and mean/average droplet size are difficult to measure in the HWK, currently no system is available that can reliably measure these quantities under the conditions present. The two main reasons for this are the short duration of the experiment and the large temperature gradients that occur once the heated gas behind the expansion wave flows into the test section of the wind tunnel.

For example measurement techniques relying on phase doppler anemometry (PDA) have a very small measurement volume, requiring many droplets to pass through the volume before reliable statistical information about the whole spray is available.

Backlight shadow sizing techniques could be an option in the future, but currently the volume of spray that can be measured with this technique in a “one shot” experiment is too small, especially if small droplets of technical sizes are of interest. Also the large temperature gradients tend to distort regions of the image, complicating the correct sizing of small particles.

Similar difficulties arise with interferometric particle imaging (IPI), where the interference pattern of refracted and reflected light from the droplet is used to determine its size. This pattern is highly susceptible to large changes in refractive index.

Hence, a theoretical approach would be necessary to derive the most vital spray characteristics from the parameters that can be easily measured, such as the geometry of the nozzle, the injection conditions (i.e. injection pressure and temperature), ambient conditions (i.e. flow velocity, pressure and temperature in the HWK) and liquid properties of the fuel injected. Such a theoretical treatment however has not yet been developed, due to the complexity of the spray break-up process; hence the only option available is an empirical treatment of the processes involved.

The following section will describe the challenges involved in a theoretical spray break-up treatment and continue to highlight the most promising empirical approaches developed over the years.

## **2.2.2 Atomisation**

Although there is no complete theoretical treatment of the atomising process, which is the disintegration of a bulk liquid into a spray [34], there are nonetheless many basic concepts that are well understood and which help in the understanding of spray generation.

In atomisation the cohesive forces of a liquid, namely surface tension and viscosity are overcome by external forces, causing larger portions of the liquid to reorganise into smaller drops in order to keep surface energy to a minimum. In general the external disrupting forces that promote break-up are of mechanical and aerodynamic nature. The mechanical forces arise due to interactions between the fast flowing liquid and the discharge orifice, while the aerodynamic forces arise due to velocity differential between the jet and/or droplet with the surrounding atmosphere.

Hence, the spray break-up process can be categorised in two mechanisms; primary spray break-up or atomisation, which is characterised by the amplification of initial disturbances in the jet surface issuing from an orifice and secondary spray break-up or atomisation. The latter mechanism is characterised by the break-up of drops formed by primary break-up, which exceed a critical size and are disintegrated into smaller droplets by the aerodynamic forces that are exerted upon them [34].

### **2.2.2.1 Primary Spray Break-up**

The most basic case of primary break-up of a liquid issuing from a round orifice is that of almost static drop formation or dripping, where the flow velocity in the nozzle is very low. In this case gravity is the main disruptive force trying to “tear the drop away” from the exit of

the nozzle, while the surface tension force opposes this force and hence constitutes the cohesive element. This means that equating the force of gravity with the surface tension force will describe this system:

$$F_g = F_{st} \quad (2.2.1)$$

$$m_D g = \pi d_0 \sigma \quad (2.2.2)$$

$$m_D = \frac{\pi d_0 \sigma}{g} \quad (2.2.3)$$

The above assumes a cylindrical column issuing from the nozzle. The mass of such a droplet then would equate to a spherical droplet:

$$D = \left( \frac{6d_0 \sigma}{\rho_L g} \right)^{\frac{1}{3}} \quad (2.2.4)$$

For practical applications however this type of drop formation is not relevant as the drops formed in this manner are always of large size and the flow rate is rather low.

Of more interest is the disintegration of liquid jets, where a larger flow rate is involved. This has been the focus of much scrutiny over many years, while the earliest investigation was carried out by Bidone [35] and Savart [36] in the early 19<sup>th</sup> century. Savart's research was the first to supply quantitative data about the disintegration of jets by observing that:

1. With constant jet diameter the continuous jet length is directly proportional to jet velocity.
2. When the jet velocity is kept constant, the continuous jet length is directly proportional to its diameter.

This led to the development of the first theoretical treatment of low speed jets issuing from round orifices, by Rayleigh [37]. His approach was based on the comparison of the surface energy ( $E_S$ ) of the disturbed and undisturbed jet configuration. This was based on the assumption that small initial disturbances in the jet must be the starting point of instabilities in the jet, eventually leading to disintegration.

$$E_S = \frac{\pi \sigma}{2d} (\gamma^2 + n^2 - 1) b_n^2 \quad (2.2.5)$$

Where

$$\gamma = \frac{2\pi}{\lambda} \quad (2.2.6)$$

Equation (2.2.5) describes the potential energy of a disturbed jet configuration with respect to the undisturbed equilibrium condition. Since a liquid system always minimises its surface energy, as long as  $E_S$  is positive, the system is stable (more energy would be needed to acquire the new disturbed configuration). If on the other hand  $E_S$  is negative, another configuration with less energy content exists and hence the current configuration is unstable.

By inspection of equation (2.2.5), there are two cases:

1. The system is always stable to disturbances which are nonsymmetrical i.e.  $n \gg 1$
2. The system is unstable if,  $n = 0$  and  $\gamma < 1$ , which leads to:

$$\lambda > \pi d \quad (2.2.7)$$

Hence, Rayleigh found that a jet issuing from a round orifice is always unstable to disturbances, which are greater than the jet diameter. This is of course under the condition that the jet is mainly controlled by surface tension and not viscosity, as equation (2.2.5) makes no allowance for the latter.

Furthermore Rayleigh not only realised that any disturbance, which satisfies equation (2.2.7) will grow, but also that there is a type of disturbance which will grow fastest.

Rayleigh was the first to treat jet break-up as a dynamic problem. With this assumption in mind, Rayleigh assumed the constant  $b_n$  in equation (2.2.5) to be proportional to the exponential growth of a disturbance:

$$b_n \sim e^{qt} \quad (2.2.8)$$

Rayleigh then went on to show, that the maximum growth rate is given by:

$$q_{\max} = 0.97 \left( \frac{\sigma}{\rho_L d^3} \right) \quad (2.2.9)$$

And consequently that:

$$\lambda_{opt} = 4.51d \quad (2.2.10)$$

As in equation (2.2.4), this means that a cylindrical section of  $4.51d$  will detach from the continuous jet, to form a round droplet:

$$D = 1.89d \quad (2.2.11)$$

This very significant result expands the initial idea of quasi static droplet formation discussed initially, to the drop formation in slow jets issuing from a round orifice.

Later experimental results by Tyler [38] confirmed Rayleigh's analysis, even though real jets are viscous, turbulent and influenced by aerodynamic forces. Tyler measured the relationship between optimum wavelength and drop diameter to be:

$$\lambda_{opt} = 4.69d \quad (2.2.12)$$

$$D = 1.92d \quad (2.2.13)$$

Which show a remarkably close resemblance to the pure theoretical results from Rayleigh as can be seen in equation (2.2.10) and (2.2.11) respectively.

The theory of Rayleigh was later extended to viscous liquids, by Weber [39]. The jet velocity in this case, was still low however. Weber found that for a nonviscous liquid:

$$\lambda_{\min} = \pi d \quad (2.2.14)$$

$$\lambda_{opt} = \sqrt{2}\pi d = 4.44d \quad (2.2.15)$$

This is again fairly similar to Rayleigh's original theory. For viscous fluids however Weber found that:

$$\lambda_{\min} = \pi d \quad (2.2.16)$$

$$\lambda_{\text{opt}} = \sqrt{2\pi d} \left( 1 + \frac{3\mu_L}{\sqrt{\rho_L \sigma d}} \right) \quad (2.2.17)$$

It is interesting to note that minimum wavelength that is required to produce instability is the same for both the viscous and nonviscous case.

Weber attributed this instability (quite similar to Rayleigh) to the formation of dilational waves (see Figure 2.7) in the jet. But Weber also continued to study the influence of relative air velocity to the jet and found that an increased relative air velocity leads to a reduction in both the minimum and optimum frequencies (here for 15m/s):

$$\lambda_{\min} = 2.2d \quad (2.2.18)$$

$$\lambda_{\text{opt}} = 2.8d \quad (2.2.19)$$

Weber attributed this change to another mode of jet oscillation, namely sinuous waves (see Figure 2.7) of the entire jet, induced by the air velocity. Further increases in relative air velocity lead to further reductions in frequency [34].

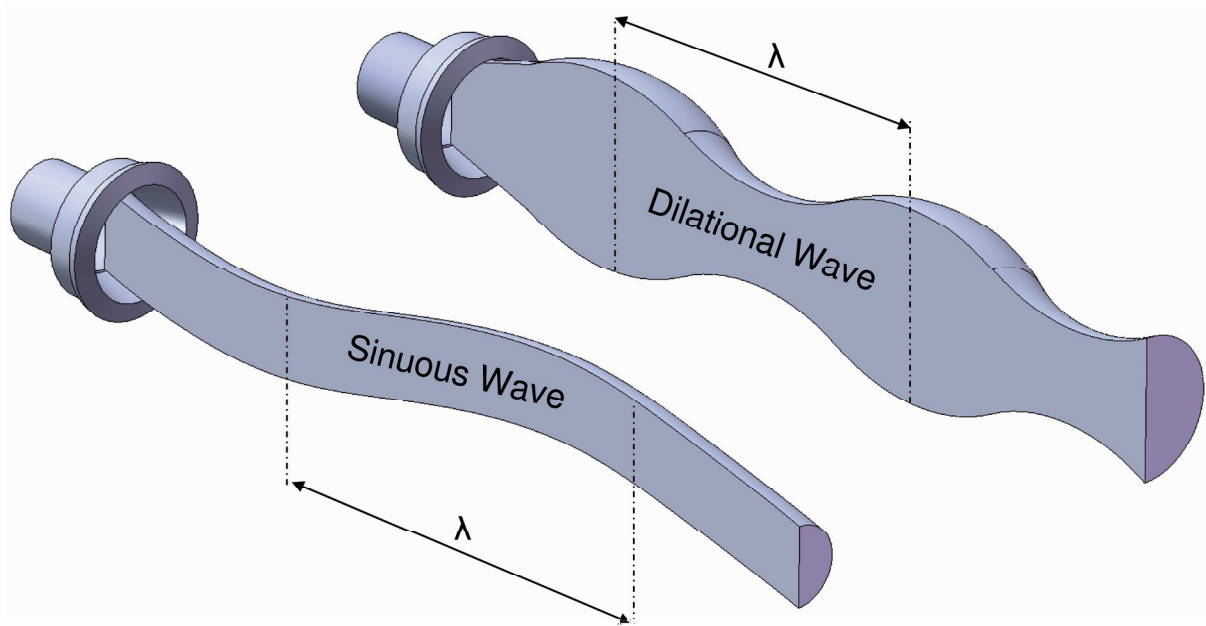


**Figure 2.7** – Rotationally symmetric disturbance (dilational wave), and jet disturbance (sinuous wave)

Further, since the breakup of a droplet in a flowing air stream (or a moving droplet within stagnant air) is controlled by dynamic pressure, surface tension and viscous forces, Weber set out to define a non-dimensional parameter that would define this phenomenon. He found that for liquids with low viscosity the breakup is mainly controlled by dynamic pressure,

$$\Delta p = \frac{1}{2} \rho_A u_R^2 \quad (2.2.20)$$

and surface tension forces, which are related to  $\sigma/D$ , forming the non-dimensional group known as the Weber number [34]:

$$We = \frac{\rho_A u_R^2 D}{\sigma} \quad (2.2.21)$$

A high Weber number indicates that the deforming external forces due to relative droplet velocity are high compared to the consolidating forces from surface tension and droplet breakup is more likely.

Weber's theoretical approach was confirmed experimentally by Haenlein [40], who further separated the results into four distinct categories of jet break-up.

1. Jet break-up and droplet formation without the influence of air. (Rayleigh's Theory)
2. Jet break-up and droplet formation with the influence of air in a dilational wave manner (low relative air velocity).
3. Jet break-up and droplet formation with the influence of air in a sinuous wave manner. (higher relative air velocity)
4. Jet break-up and droplet formation, immediately downstream of the nozzle, also known as atomisation (very high jet velocity).

This classification was further improved upon by Ohnesorge [41], who conducted a dimensional analysis on a large number of photographs of sprays, to discern between the influence of different forces acting upon the spray.

His analyses lead to the development of the Ohnesorge Number:

$$Oh = Z = \frac{\sqrt{We}}{Re} = \frac{\mu_L}{\sqrt{\rho_L \sigma d_0}} \quad (2.2.22)$$

With the Ohnesorge number and a more recent analysis by Reitz [42], who compiled and compared his own work with that of many other workers, a precise classification of a spray into one of four operating regimes is possible:

1. Rayleigh jet breakup
2. First wind-induced breakup
3. Second wind-induced breakup
4. Atomisation

These four categories constitute the current standard for the classification of the primary breakup mechanism. The droplet size produced becomes progressively smaller, as one advances from the first category to the next, while the jet velocity becomes progressively larger.

The above relationship however has a drawback: since Ohnesorge conducted his analysis only under atmospheric conditions, it is not applicable to high pressure environments.

A work by Czerwonatis et al. [43], where the equation (2.2.22) was modified to include the high pressure regime remedied this problem.

$$Z^{**} = Oh_L \sqrt{We_G} = \frac{\sqrt{We_L \cdot We_G}}{Re_L} = \frac{\eta_L \nu}{\sigma} \sqrt{\frac{\rho_G}{\rho_L}} \quad (2.2.23)$$

The above relationship also includes the effect of elevated ambient pressure and allows the classification of the droplet breakup mechanism in any environment and an example of this can be seen in Figure 2.8, which also indicates the spray breakup mode of the experiments in this study.

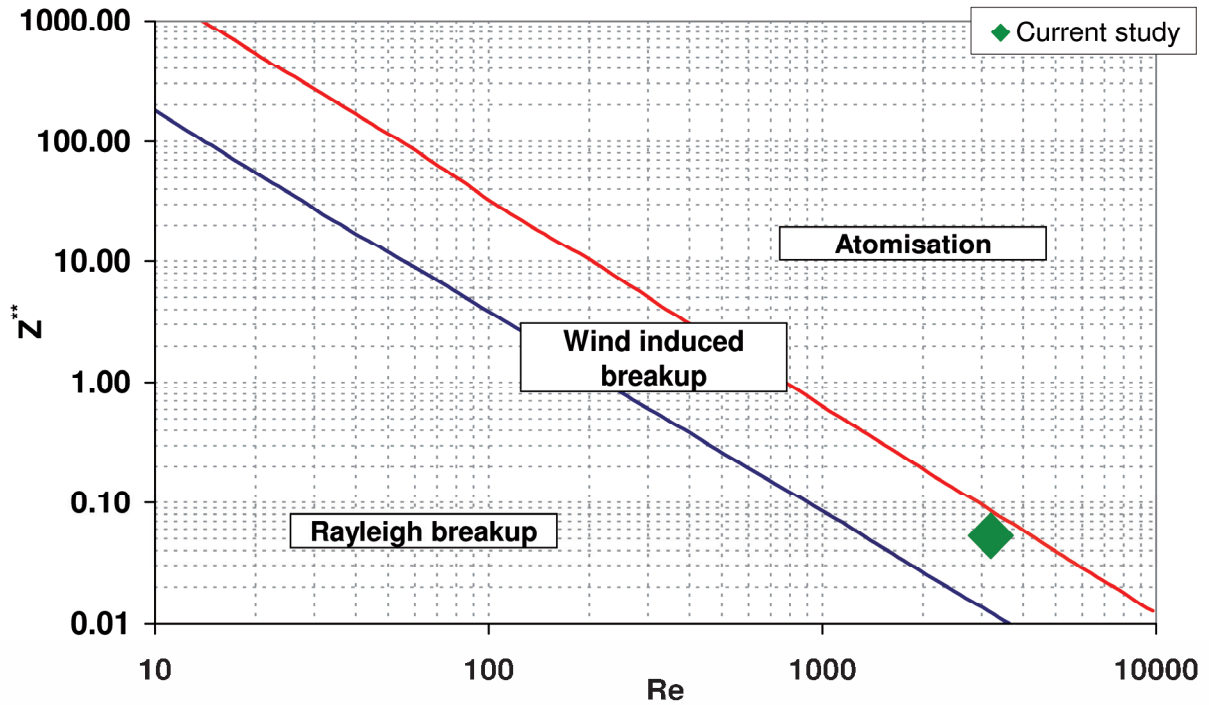


Figure 2.8 – Spray primary breakup classification (with current study indicated - green)

### 2.2.2.2 Secondary Spray Breakup

Once the spray has been created in the primary breakup, the ensuing droplets may still be too big to keep integrity, due to the aerodynamic forces acting upon them. This further disintegration of droplets is known as secondary spray breakup [34].

In this case there are three main forces, which act upon the droplet. Two of these are of stabilising nature (i.e. they keep the droplet from breaking up), while one is destabilising the droplet. The former are internal pressure and surface tension, while the latter are aerodynamic forces. Since the internal pressure is dictated by the surroundings of the droplet and remains constant, any change in aerodynamic pressure on the droplet surface has to be compensated by surface tension.

$$p_I = p_A + p_\sigma \quad (2.2.24)$$

If the external pressure on the droplet becomes too large and cannot be compensated by  $p_\sigma$  the droplet will start to deform and will eventually break up into smaller droplets, which have a higher stability as can be seen by inspection of equation (2.2.25).

$$p_\sigma = \frac{4\sigma}{D} \quad (2.2.25)$$

The drops will continue to subdivide until they are small enough to compensate the aerodynamic forces acting upon them. Hence there must be a critical droplet size, which demarks the boundary between a droplet just small enough not to break up anymore and one which is just too large. This leads to the conclusion that a spray may have many droplet size classes below the critical droplet size, but none (given enough time) above it.

In essence there are three main types of droplet breakup, according to Tanner et al. [44] (see Figure 2.9):

1. Bag breakup
2. Stripping (shear) breakup
3. Catastrophic Breakup

These three categories are distinguished by the Weber number. Bag breakup occurs in ranges of  $6 < We < 80$ , stripping breakup in a range of  $80 < We < 350$  and catastrophic breakup occurs when  $We > 350$ .

The two main phenomena driving these types of droplet breakup are known as Rayleigh-Taylor (R-T) instability and Kelvin-Helmholtz (K-H) instability [34].

R-T instability occurs when two immiscible fluids of different densities interact and the denser fluid is pushed by the lighter fluid (in this case air acting upon the fuel). The inertial forces of the fluid oppose the deformation. Once such disturbances are established they grow exponentially [34].

K-H instabilities on the other hand, are caused by the shear between the droplet and the surrounding moving air [34].

It is important to note that for all these cases, it is the relative velocity of the air with respect to the droplet that determines the Weber number. Hence, when the droplet first enters the airflow the relative velocity and Weber number are high (both due to the airflow and the

velocity of the injected droplet). The relative velocity will then decrease as the droplet trajectory approaches the direction and magnitude of the surrounding flow.

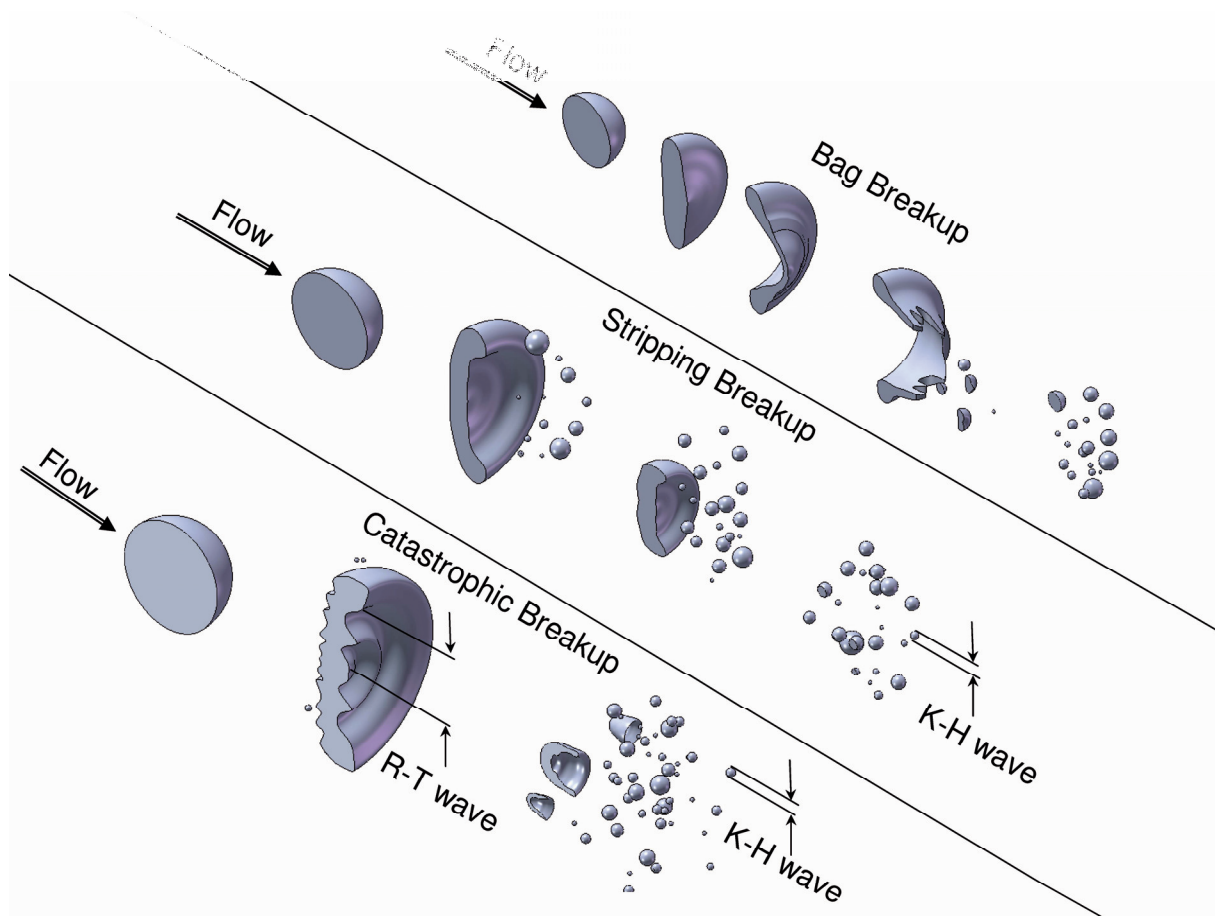


Figure 2.9 – Droplet breakup modes according to Tanner et al. [44]

As can be seen the breakup of droplets in a flow field is determined by many factors and since most flow fields of practical significance also contain turbulence, these local velocity fluctuations further complicate matters. This is also the reason for the afore mentioned absence of a complete theoretical model for spray generation, there are simply too many factors influencing the process.

Nonetheless the previous descriptions can give a general classification as to the overall nature of the spray. The next two sections will discuss how the drops occurring in a spray can be classified and also show some empirical methods that can be used to glean some insight into the drop size distributions that can be expected of a certain injection configuration.

### 2.2.3 Spray Characterization

In the previous section it was shown, that the process of spray generation is a heterogeneous one, where there is not one droplet size but rather a large number of different droplet sizes, which are distributed about some mean droplet size. Figure 2.10 shows some mean droplet sizes which can occur in nature for comparison, while most technical sprays for practical applications produce sprays in the range of a few micrometers to about  $500\mu\text{m}$  [34].

Almost homogenous sprays can only be created under special circumstances, and do not occur under the JICF (Jet in Cross Flow) configuration under consideration in this work.

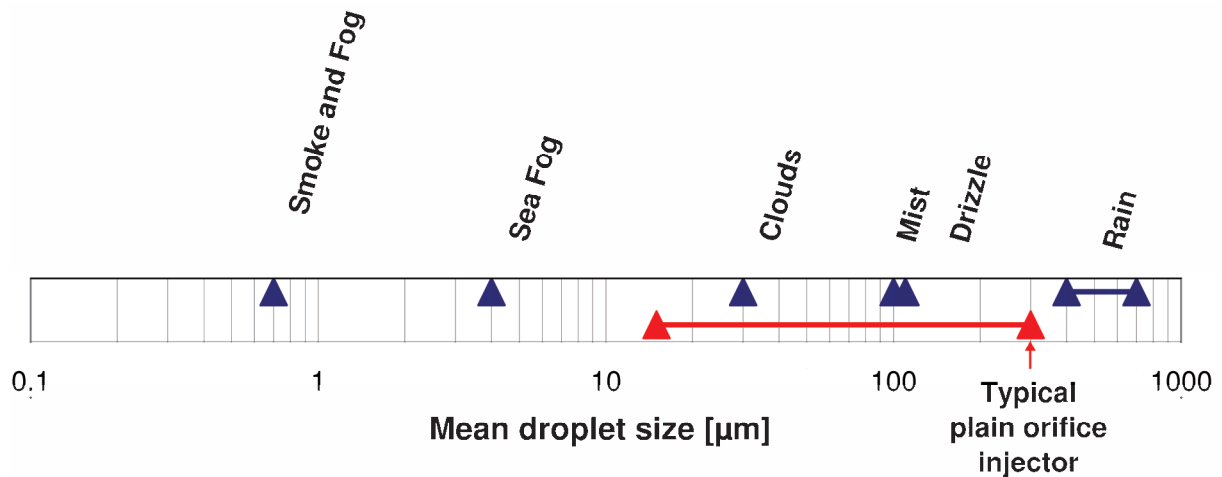


Figure 2.10 – Spray spectrum in nature [45]

Since sprays with the same mean droplet size might still be two completely different sprays due to the distribution of the other classes of droplets, a standardised method for classifying sprays is required. This section will briefly describe the methods used to classify sprays and introduce definitions that will be used throughout this work.

### 2.2.3.1 Mathematical Description of Spray Data

One way to classify a spray is to organize the droplets into different size categories and represent the result graphically. This is known as a histogram. In its most simple form the number of drops (falling into a certain predefined size category) are counted and a resulting bar diagram is a representation of the spray. An example of this is shown in Figure 2.11. Here a hypothetical spray of 2360 drops is categorised in size groups of 20 μm.

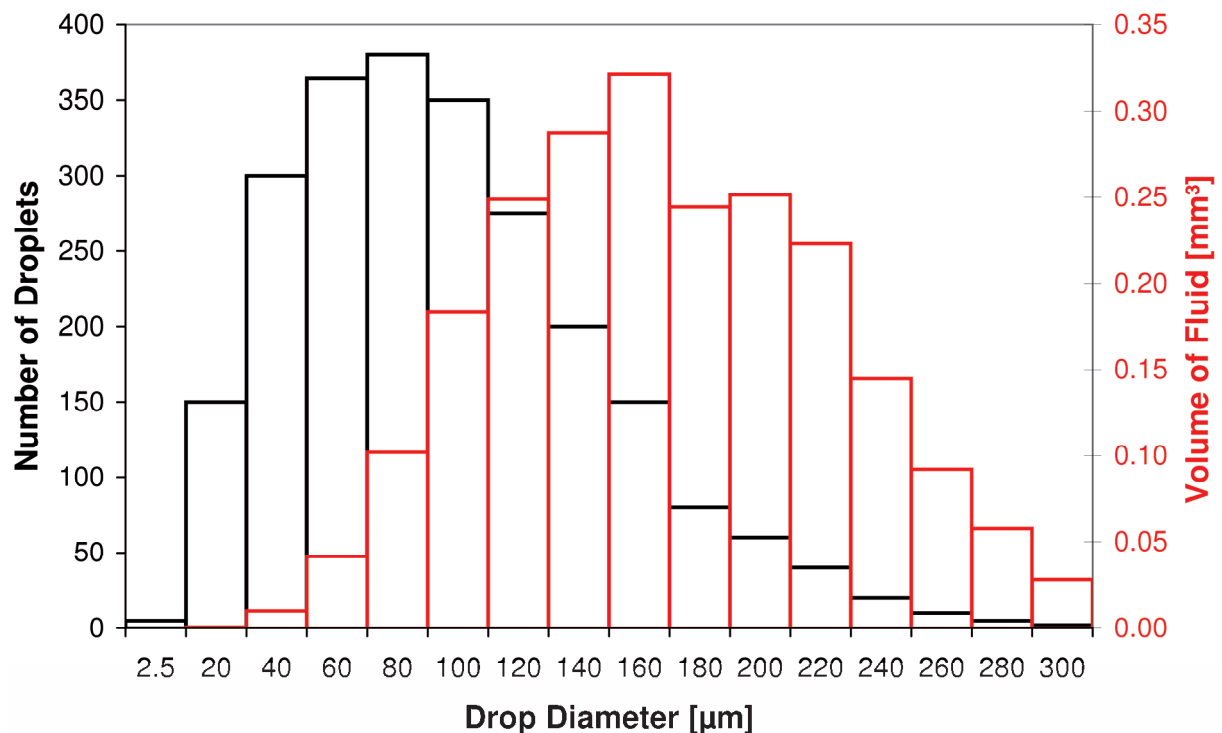


Figure 2.11 – Example of a drop size histogram

In some cases (especially combustion for example) it can be more useful however, to represent the spray not in terms of number of droplets but in terms of volume (or mass). In this case the same spray has a histogram that is skewed to the right as larger drops contain most of the fluid volume (see Figure 2.11).

This representation can also be normalised with the total number of drops or the total volume respectively. The area enclosed by the graph must then equal one.

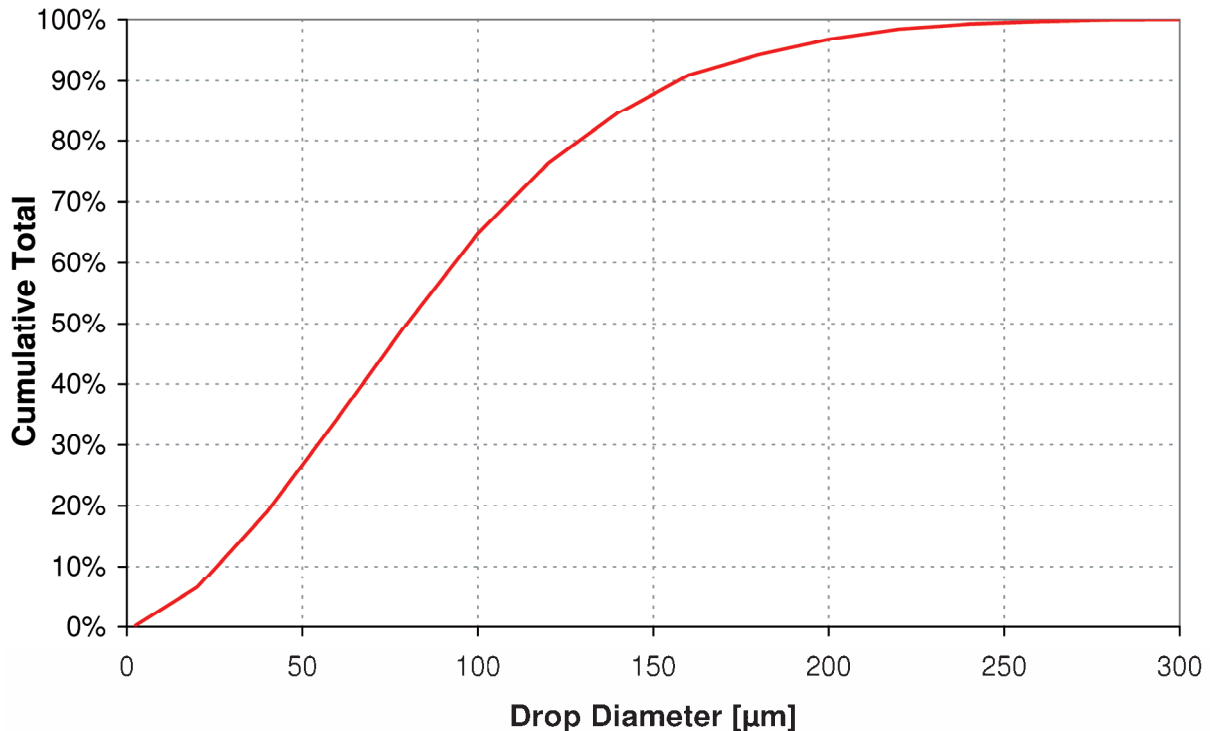


Figure 2.12 – Cumulative total

If the number of samples is large enough the interval for each size class can be reduced and the bar graph becomes a curve. This is then known as the frequency distribution curve.

Another useful parameter that is indicative of the type of spray that is present and can be used to further compare sprays is a cumulative distribution curve. An example of this is shown in Figure 2.12 (again for the above hypothetical spray). This type of curve is in essence only the integral of the frequency distribution curve. In this case it is often sensible to normalise this information with the total number of droplets or mass (flow) so that the resulting curve represents the percentage of the spray.

The above representation of the spray in terms of histograms or frequency distribution curves has the disadvantage that it assumes almost complete knowledge of the spray (i.e. droplet sizes and number are known). This information however is very difficult to obtain. Especially in the case of this study where the entire spray generation and measurement thereof must be completed in a few milliseconds, in a hot – high pressure environment.

In order to overcome such difficulties many researchers have endeavoured to describe the spray with mathematical distribution function, which should in general be able to perform the following tasks [34]:

1. It should adequately fit to the drop size data
2. Allow an extrapolation of drop size data with only a few real measurement points
3. Allow for the calculation of mean and representative drop diameters

#### 4. Consolidate the large amounts of data

As was described in the previous sections there is no complete model for the generation of a spray. Due to this deficiency many functions have been proposed that can be used to represent spray. These have been mainly proposed based upon empirical or probability considerations. The most common distributions are the normal, log-normal, Nukiyama-Tanasawa, Rosin-Rammler and Upper-limit-function/distribution [34], all of which have their limitations and should be tested against experimental data wherever possible.

For this work, the Rosin – Rammler [46] distribution was used, as it is fairly powerful and is still the standard function used to describe spray droplet distributions due to its mathematical ease of use and adaptability. It is given by the following formula:

$$1 - Q = e^{-\left(\frac{D}{X}\right)^q} \quad (2.2.26)$$

Where  $Q$  is the liquid volume fraction (or percentage of droplets containing drops of smaller diameter than  $D$ ), and  $D$  is the droplet diameter.  $X$  and  $q$  are constants and must be determined from the experimental data. For most sprays  $q$  lies between 1.5 and 4 [34]. It indicates the spread of the spray; the larger  $q$  the more uniform the spray will be and in the case of  $q = \infty$ , the spray is monodisperse.

Typically,  $q$  is determined from a graph as shown in Figure 2.13, where the slope of the line through all data points is  $q$ . In this case the data is again taken from the hypothetical spray mentioned above. The value of  $X$  is the representative diameter, where  $Q=0.632$  (from  $1-Q=\exp(-1)$ ) or 63,2% of the total liquid volume is contained in droplets of smaller diameter.

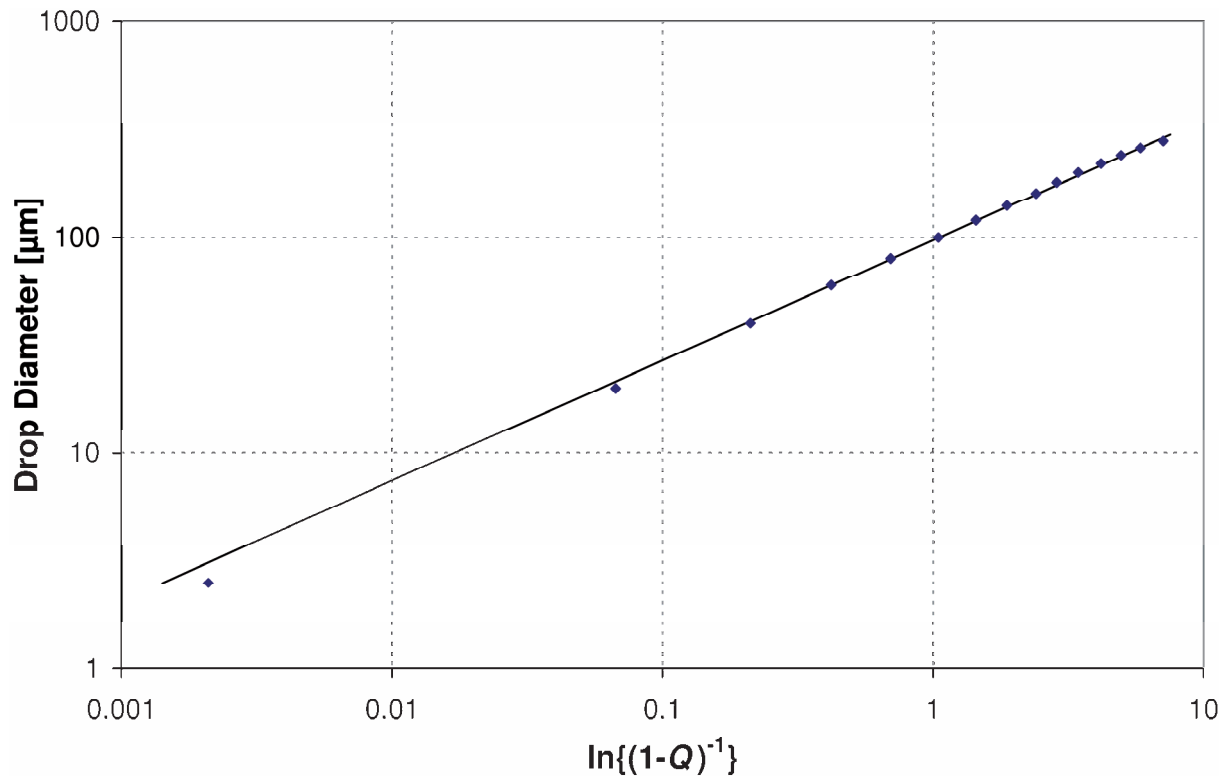


Figure 2.13 – Rosin-Rammler data plot

The final result of such a plot can be seen in Figure 2.14, where the frequency distribution curve resulting from a Rosin – Rammler distribution is displayed against the data points of the hypothetical spray used throughout this section.

Figure 2.14, also displays a number of representative diameters, one of which ( $X$  or  $D_{0.632}$ ) was already mentioned above in the calculation of the Rosin – Rammler function and one mean diameter: the Sauter Mean Diameter (SMD). These different representative and mean diameters are helpful for the discussion and mathematical treatment of sprays and shall now be introduced in more detail.

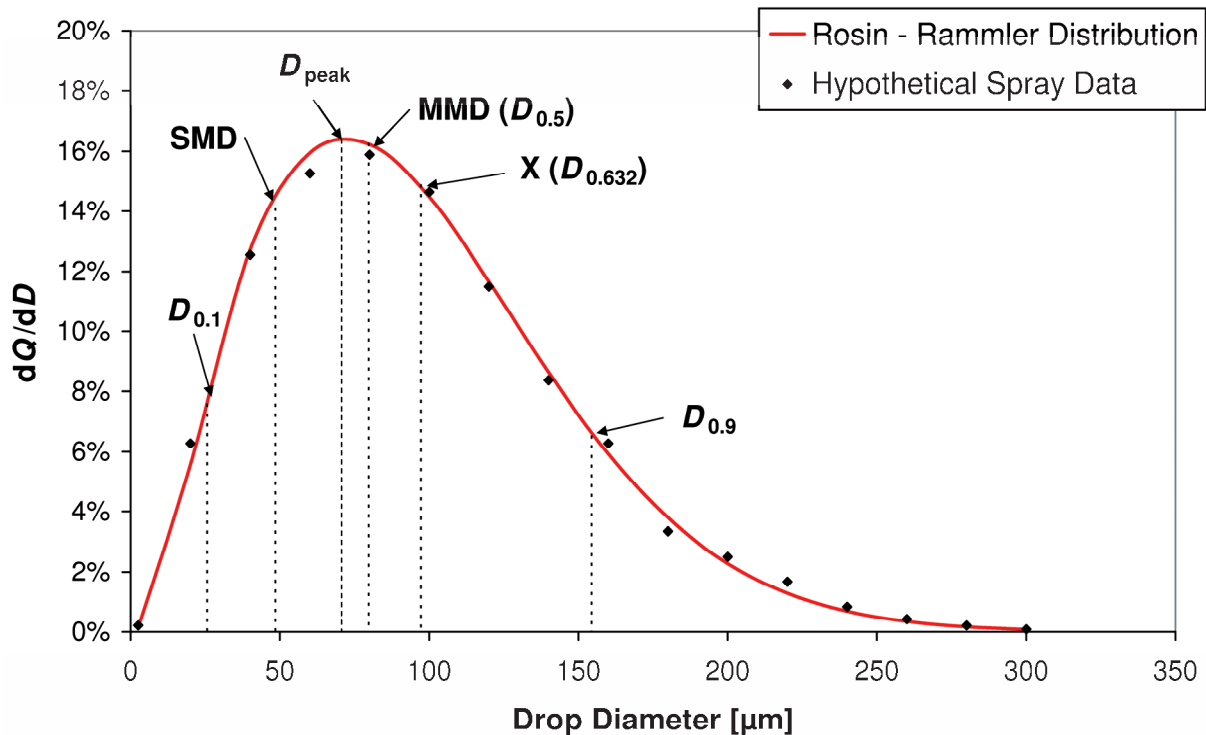


Figure 2.14 – R-R function with representative diameters indicated

Mugele and Evans in 1951, set out to standardize mean diameters of the droplets in a spray. Their standardized notation is still in use today and conforms to the following formula [47]:

$$(D_{ab})^{a-b} = \frac{\int_{D_0}^{D_m} D^a \left( \frac{dN}{dD} \right) dD}{\int_{D_0}^{D_m} D^b \left( \frac{dN}{dD} \right) dD} \quad (2.2.27)$$

The arithmetic mean diameter hence is defined as follows:

$$D_{10} = \frac{\int_{D_0}^{D_m} D \left( \frac{dN}{dD} \right) dD}{\int_{D_0}^{D_m} \left( \frac{dN}{dD} \right) dD} \quad (2.2.28)$$

But from this definition many other mean diameters are possible depending on which field of interest one is focusing on. In the case of this study this is the SMD, which is most interesting in reacting and combusting systems [34]. The SMD represents a drop whose ratio of volume to surface is equal to that of the whole spray. It can easily be seen that this can be especially important in the description of combusting sprays, as it relates the droplets volume to its surface area, which is the only interface for mass and energy transfer in droplet combustion. Hence, since the ratio of volume to surface is of special interest, with the definition given in equation (2.2.27) the SMD must equal:

$$D_{32} = \frac{\int_{D_0}^{D_m} D^3 \left( \frac{dN}{dD} \right) dD}{\int_{D_0}^{D_m} D^2 \left( \frac{dN}{dD} \right) dD} \quad (2.2.29)$$

Of course equation (2.2.27) can also be written as a summation if a histogram with size classes is considered instead of a frequency distribution curve.

$$D_{ab} = \left[ \frac{\sum N_i D_i^a}{\sum N_i D_i^b} \right]^{\frac{1}{a-b}} \quad (2.2.30)$$

The following Table shows some commonly used mean diameters and their applications [34].

<i>a</i>	<i>b</i>	<i>Order</i> ( <i>a + b</i> )	<i>Symbol</i>	<i>Name</i>	<i>Expression</i>	<i>Application</i>
1	0	1	$D_{10}$	Length	$\frac{\sum N_i D_i}{\sum N_i}$	Comparison
2	0	2	$D_{20}$	Surface area	$\left( \frac{\sum N_i D_i^2}{\sum N_i} \right)^{\frac{1}{2}}$	Surface area controlling
3	0	3	$D_{30}$	Volume	$\left( \frac{\sum N_i D_i^3}{\sum N_i} \right)^{\frac{1}{3}}$	Volume controlling e.g. hydrology
2	1	3	$D_{21}$	Surface area – length	$\frac{\sum N_i D_i^2}{\sum N_i D_i}$	Absorption
3	1	4	$D_{31}$	Volume – length	$\left( \frac{\sum N_i D_i^3}{\sum N_i D_i} \right)^{\frac{1}{2}}$	Evaporation, molecular diffusion
3	2	5	$D_{32}$	Sauter Mean Diameter (SMD)	$\frac{\sum N_i D_i^3}{\sum N_i D_i^2}$	Mass transfer, reaction
4	3	7	$D_{43}$	De Brouckere or Herdan	$\frac{\sum N_i D_i^4}{\sum N_i D_i^3}$	Combustion equilibrium

**Table 2.2** – Table of mean diameters [34]

In addition to the above definitions, there is also another helpful definition of useful representative diameters, which should not be confused with the mean diameters in Table 2.2:

$$D_{Vf} \quad (2.2.31)$$

Where  $Vf$  is the volume fraction, such that  $Vf$  of the total liquid is present in drops smaller than this diameter  $D$ .

For example  $D_{0.1}$  is the drop diameter, below which only 10% of the total spray volume is present. Or 10% of the total volume/mass is located in droplets smaller than this diameter. Accordingly  $D_{0.5}$  is the diameter of a droplet such that 50% of the total spray volume is located in drops smaller than this diameter.  $D_{0.5}$  is also known as the Mass Median Diameter (MMD).

One final definition is  $D_{Peak}$ , which represents the droplet with the highest occurrence frequency in the frequency distribution curve.

All of these and some other examples of such representative diameters were shown in Figure 2.14.

These representative diameters can now be used to glean some insight into the drop size dispersion (i.e. the range of drop sizes in a spray).

One such parameter is the droplet uniformity (DUI) index proposed by Tate [48], which is defined as follows:

$$DUI = \frac{\sum_i V_i^{\ell} (D_{0.5} - D_i)}{D_{0.5}} \quad (2.2.32)$$

It takes account of all droplet size classes and indicates the spread relative to the MMD.

Another definition that can be used to indicate the spread of the spray is the relative span factor,  $\Delta$  which uses the 10<sup>th</sup> and 90<sup>th</sup> percentile to show the drop size dispersion:

$$\Delta = \frac{D_{0.9} - D_{0.1}}{D_{0.5}} \quad (2.2.33)$$

This can be expanded upon by extending the boundaries upwards – then called the dispersion boundary factor,  $\Delta_B$  which might become useful in estimating the maximum diameter:

$$\Delta_B = \frac{D_{0.999} - D_{0.5}}{D_{0.5}} \quad (2.2.34)$$

All of the above definitions can be very helpful in describing a spray more completely. This is necessary as only one parameter such as the SMD for example is often insufficient to describe the whole spray. Two sprays with completely different distributions might nonetheless still have the same SMD, so it is important to have more than just one parameter present to describe the spray fully and be able to draw conclusions.

Also, it should be noted that in the absence of a full theoretical model of spray formation no one distribution is superior over another, but rather that one distribution may fit the

circumstances of the experiment better than another, and hence care should be taken, when comparing data from different experiments which use different distributions.

## 2.2.4 Empirical Methods

Finally, in the absence of a theoretical model for determining the parameters of a spray a priori to the experiment this section will give a brief overview of the empirical formulations, which have been developed.

These of course cannot give full data of the spray but rather only some parameters, so that a comparison is possible. In the case of this study a plain orifice atomizer was used and the following table will give an overview of the available formulas for this type of atomizer [34].

<i>Equations</i>	<i>Investigators</i>
$SMD = \frac{500d_0^{1.2}v_L^{0.2}}{U_L}$	Merrington and Richardson [49]
$MMD = 6d_0 \text{Re}_L^{-0.15}$	Panasenkov [50]
$SMD = 3330d_0^{0.3} \mu_L^{0.07} \rho_L^{-0.648} \sigma^{-0.15} U_L^{-0.15} \mu_G^{0.78} \rho_G^{-0.052}$	Harmon [51]
$D_{0.999} = d_0 We_L^{-0.33} (23.5 + 0.000395 \text{Re}_L)$	Miese [52]
$SMD = 47d_0 U_L^{-1} \left( \frac{\sigma}{\rho_G} \right)^{0.25} \left[ 1 + 331 \frac{\mu_L}{(\rho_L \sigma d_0)^{0.5}} \right]$	Tanasawa and Toyoda [53]
$SMD = 2330 \rho_G^{0.121} Q^{0.131} \Delta P_L^{-0.135}$	Hiroyasu and Katoda [54]
$SMD = 3.08 v_L^{0.385} (\sigma \rho_L)^{0.737} \rho_G^{0.06} \Delta P_L^{-0.54}$	Elkotb [55]

**Table 2.3** – Table of empirical droplet diameter estimates

All of the above relations are only valid for the injection of a fuel into a quiescent atmosphere. Unfortunately, no such data exists for JICF, which is the case in this work. Hence, the above equations were used only to have some insight into the absolute maximum droplet size that can be expected in the JICF configuration. As the relative velocity between gas and liquid are much higher, droplets will tend to be smaller than indicated by the above equations (see section 2.2.2.2).

## 2.3 Single Droplet Ignition

### 2.3.1 Introduction

The results of the experimental study are meant for the validation of the “spraylet” code that is being developed at the ZARM combustion group. The spraylet code will bridge the gap between a commercial CFD code and an in house developed single droplet combustion model with detailed chemical kinetics. The CFD code will code calculate physics (e.g. spray – flow interaction and evaporation), while the spraylet code will compute all reactions and mechanisms up to ignition. The connection between the two will then be achieved through extracting characteristic single droplet trajectories from the spray and applying the varying boundary conditions along these paths on the single droplet combustion domain. Once an ignition is detected a corresponding location can be found somewhere along the trajectory. A compilation of these locations from several trajectories will then result in a plane of ignition.

Until the end of this work however, the spraylet code, the development of which is perused in a different project (Bio-Spray) was not yet available. It was hence decided, as an intermediate step, to compare the experimental results with a previous version of the single droplet ignition simulation, the CVS. This code simulates chemistry and physics of a single droplet within an enclosure of constant volume without any external interaction. Consequently, the CVS simulates a monodisperse equidistant spray. The closed vessel code is a development of Moriue et al. [56] and was used in an unmodified version for this work.

The following section will give only a brief overview of the theory involved in the CVS, for more detailed information the avid reader is pointed to works from M. Tanabe et al., O. Moriue et al. and Schnaubelt et al. [29, 30, 32, 57, 58] amongst others.

### 2.3.2 Brief Overview

The CVS is based on a single cold droplet that is suspended in an enclosure, which is closed against mass, species and energy transfer (see Figure 2.15). The vessel is filled with a quiescent hot gas and the size ratio between vessel and droplet determines the overall mixture ratio. This model is a prerequisite for the ignition simulation of small, technically sized, droplets as such droplets would not undergo ignition in an infinite volume prior to the fuels dissipation to fuel/air ratios below the flammability limit.

Since technical droplets are of very small size, the effect of convection and other anisotropic properties (thermal diffusion, momentum transfer, radiant heat flux etc.) can be neglected, leading to spherical symmetry and hence a one-dimensional model with spherical coordinates, which is sufficient to describe the processes that occur up to droplet ignition. The model itself is fully transient and for this purpose the liquid and gas phase are subdivided into a one dimensional grid, with 21 nodes in the liquid phase and 71 nodes in the gas phase. Since most chemical reactions and high gradients in the physical gas characteristics occur close to the droplet surface, the grid in the gas phase is exponential, while it is linear in the liquid phase. Hence the individual grid points in the liquid phase are given by:

$$(0 \leq r_i \leq R_s) \quad r_i = R_s \frac{i}{N_l} \quad \text{where } i \in [0, N_l] \quad (2.3.1)$$

While the individual grid point for the gas phase are given by:

$$(R_s \leq r_i \leq R_v) \quad r_i = R_s \left( \frac{R_v}{R_s} \right)^{\frac{i}{N_g}} \quad \text{where } i \in [0, N_g] \quad (2.3.2)$$

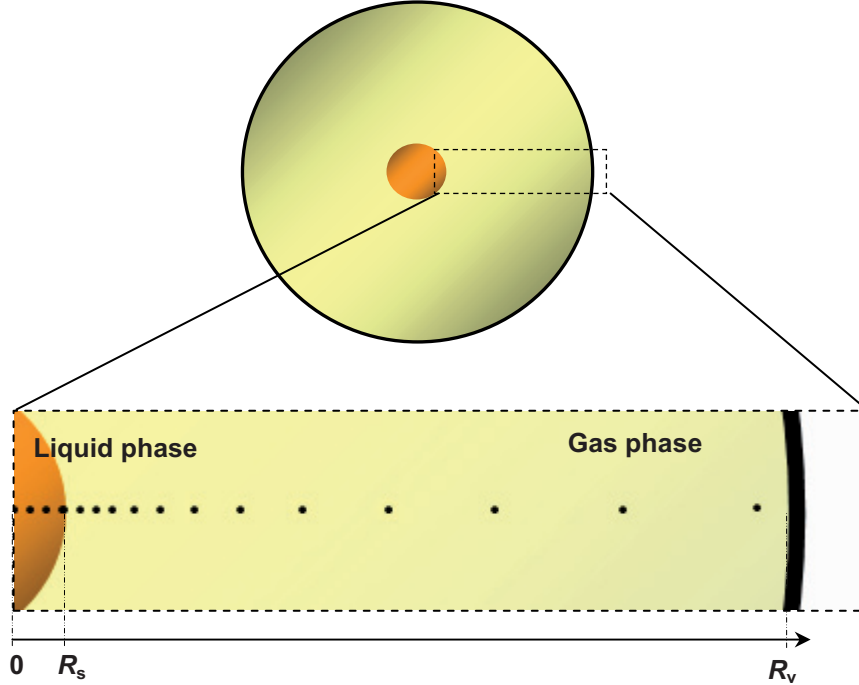


Figure 2.15 – Closed vessel droplet ignition model

The initial conditions are then applied to the liquid droplet and the gas phase. These include equivalence ratio, temperature and pressure. The equivalence ratio within the liquid phase is always one (n-heptane in this case), as the droplet evaporates and  $R_s$  reduces, the grid within the liquid phase shrinks (i.e. the grid points move closer together). At a certain predefined point (in the current study 0.5% of  $R_s$ ), when the droplet reaches critical minimal size the droplet is removed from the simulation domain and symmetry conditions are applied at the grid point  $R_s$  and calculation of the gas phase will commence normally. For the liquid phase, continuity, heat flow and state will be solved:

$$\frac{\partial \rho}{\partial t} + \text{div}(\rho \cdot \mathbf{u}) = 0 \quad (2.3.3)$$

$$\rho c_p \left( \frac{\partial T}{\partial t} + \mathbf{u} \cdot \nabla T \right) = \text{div}(\lambda_c \cdot \nabla T) \quad (2.3.4)$$

$$p = Z \rho R T \quad (2.3.5)$$

where  $\lambda_c(T)$ ,  $c_p(T)$  and  $Z(p, T)$ .

From the above equations it can be seen that the pressure is assumed spatially constant but is allowed to vary with time. Temperature on the other hand is not only dependent on time but also location, allowing the surface layers closer to the gas phase boundary to become heated and a temperature distribution in the droplet to be established.

The liquid – gas boundary conditions are given by mass/species -, heat flow, continuity, fugacity and temperature:

$$\left. \begin{array}{l} \rho_l \mathbf{u}_l \quad i = fuel \\ 0 \quad i \neq fuel \end{array} \right\} = \rho_g D_i \cdot \nabla Y_i - \rho_g Y_i \left( \mathbf{u}_g - \frac{dR_s}{dt} \right) \quad (2.3.6)$$

$$\lambda_l \cdot \nabla T_l - \lambda_{c,g} \cdot \nabla T_g = \rho_l \mathbf{u}_l h_{vapour} \quad (2.3.7)$$

$$-\rho_l \mathbf{u}_l = \rho_g \left( \mathbf{u}_g - \frac{dR_s}{dt} \right) \quad (2.3.8)$$

$$\psi_l \cdot Y_{l,i} \cdot p_l = \psi_g \cdot Y_{g,i} \cdot p_g \quad (2.3.9)$$

$$T_l = T_g \quad (2.3.10)$$

Two important factors to note are the heat flow and temperature conditions. If the fuel droplet has a lower temperature than the surrounding gas, which is almost always the case, some cooling will occur in the gas phase adjacent to the droplet. Since the vessel is closed to the surroundings no new additional heat can enter the computational domain and the overall temperature will drop slightly. This could become a relevant error if the mixture is set to be very rich (i.e. very small vessel with a large droplet), in which case the total heat capacity of the fuel droplet would be larger than the total heat capacity of the surrounding gas. Also, since the vessel is closed energy taken from the gas phase to evaporate the droplet (enthalpy of evaporation) cannot be replenished from the outside, which can significantly impact the gas phase temperature during the simulation.

This was always taken into account when a simulation was initiated.

For the gas phase two sets of equations are solved, the first one treating the fluid dynamical properties of the problem (i.e. continuity, heat flow, species flow and state):

$$\frac{\partial \rho}{\partial t} + \text{div}(\rho \cdot \mathbf{u}) = 0 \quad (2.3.11)$$

$$\rho c_p \left( \frac{\partial T}{\partial t} + \mathbf{u} \cdot \nabla T \right) = \text{div}(\lambda_c \cdot \nabla T) + q \quad (2.3.12)$$

$$\frac{\partial(\rho \cdot Y_i)}{\partial t} + \text{div}[\rho \cdot Y_i \cdot (\mathbf{u} + \mathbf{v}_{D,i})] = w_i \quad (2.3.13)$$

$$p = \rho RT \quad (2.3.14)$$

In this case, as the gas phase is a non-perfect mixture of multiple species, thermal conductivity is not only dependent on temperature and pressure but also the combined effect of all species properties.

$$\lambda_c(T, p, \sum Y_i) \quad (2.3.15)$$

The same is true for heat capacity and diffusive velocity:

$$c_p = \sum Y_i \cdot c_{p,i}(T, p) \quad (2.3.16)$$

$$\mathbf{v}_{D,i} = \sum D_j \cdot \nabla Y_j \quad (2.3.17)$$

The heat and species produced in the gas phase result from a reduced chemical reaction mechanism for n-heptane with 67 species and 437 reactions, which are each defined by a certain reaction rate.

Finally, reaching the outer boundary of the vessel, which is closed completely against the surroundings and hence the boundary conditions are given by:

$$\frac{\partial T}{\partial r} = 0 \quad (2.3.18)$$

$$\frac{\partial Y_i}{\partial r} = 0 \quad (2.3.19)$$

$$v = 0 \quad (2.3.20)$$

This concludes this brief overview of the CVS, which was used as an unmodified tool in this work. As mentioned before the reader is referred to the appropriate sources for more information on the CVS.

### 2.3.3 Closed Vessel Simulation Validation

The results of the CVSs cannot be directly compared to single droplet experiments, since a small closed vessel cannot be produced experimentally. A very large vessel however, where the equivalence ratio tends to infinity, can be investigated experimentally, as it resembles a pressurized oven which encloses a small single droplet. This then of course limits the experimental scope to events where the droplet ignites before complete evaporation, but nonetheless many such experiments in 1g and  $\mu\text{g}$  conditions were done [5, 29, 31, 32, 58]. One example of this comparison is shown in Figure 2.16.

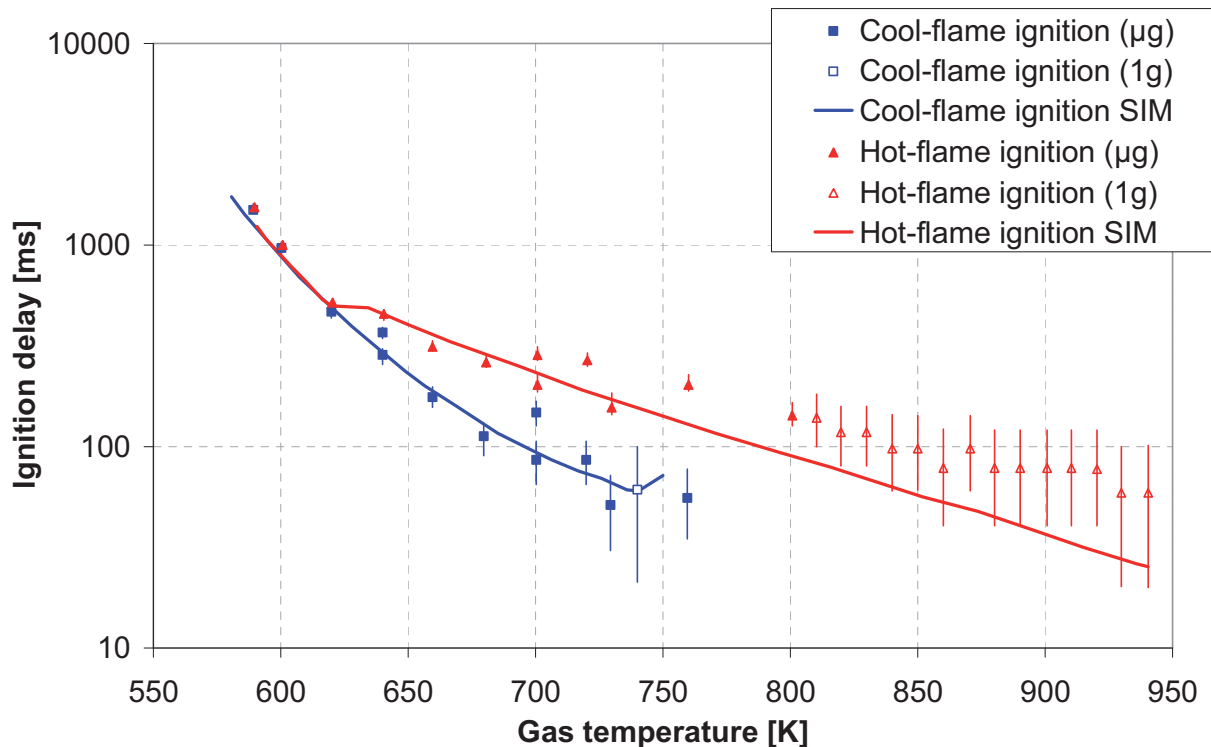


Figure 2.16 – CVS vs. experimental data, n-heptane,  $d_0=0.7\text{mm}$ ,  $p_a=0.5\text{MPa}$  [58]

Since the CVS is based on this special “open vessel” case it was indirectly validated against single droplet experimental data.

However, the results of the CVS were, never before compared to full spray experiments. As was mentioned before this is the next logical step in the development of a full spray ignition

simulation, since the CVS closely emulates a mono-disperse equidistant spray. This will then enable a better understanding of the effects of polydispersivity on spray autoignition, by comparing the mono-disperse CVS experiments to the real spray experiments

The main parameters needed for this type of comparison are pressure, ambient temperature, fuel temperature, overall mixture ratio, droplet diameter and induction time.

The first three of these parameters are simply initial conditions set in the CVS. The overall mixture ratio is determined by the ratio between the vessel size and droplet diameter and is hence also an initial condition. The initial droplet diameter is set to be equal to the SMD of the spray in question.

Ignition was defined to be the instant when any location in the domain reaches at least 1300K (in accordance with the definitions laid out by Schnaubelt et al. [58]), at which point the simulation will terminate. The induction time consequently is the total simulation time.

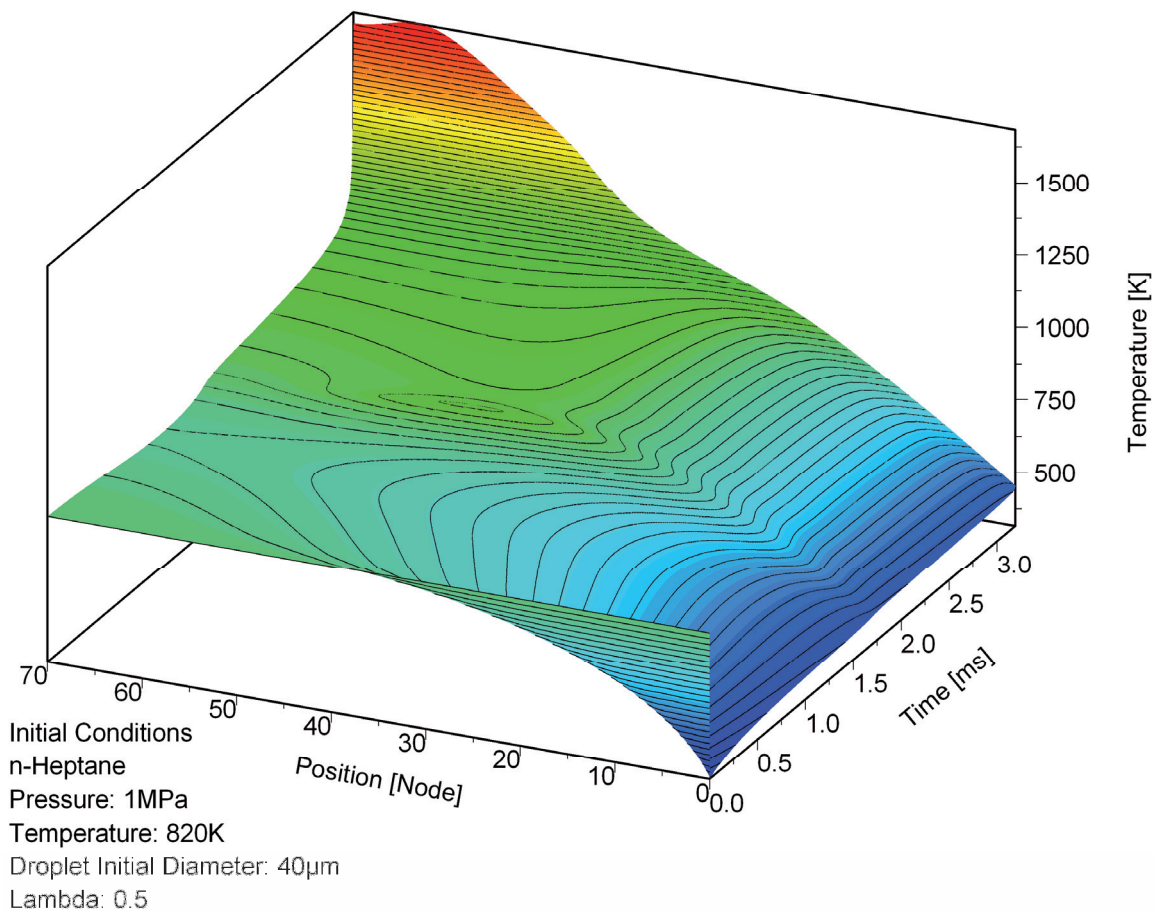


**Figure 2.17** – Gas phase temperature development of a 40 $\mu$ m droplet at  $\lambda=0.5$ , 1MPa and 820K initial conditions

An example of the temperature development of the gas phase in the simulation can be seen in Figure 2.17. Initially, the temperature in the gas phase is uniform according to the preset value (time 0ms). Within the first time step the temperatures at the first gas phase node and last liquid phase node are equalised, since the cold surface of the droplet and especially the energy needed to evaporate the droplet (enthalpy of evaporation) causes a cooling of the gas in the vicinity of the droplet. It can be seen that the temperature reduction in the gas phase near the droplet is significant up to approximately node 30, which must always be kept in mind with respect to the afore mentioned cooling/heat capacity effect. The temperature in the gas phase remains mostly unchanged, while chemical reactions take place which constitute only a minor heat release. An example of the products of these reactions can be seen in Figure 2.18, which

shows the formaldehyde ( $\text{CH}_2\text{O}$ ) concentration in the gas phase. Formaldehyde is a cool flame indicator, a weak blue flame, with only minor heat release that precedes the bright hot flame ignition. The increase in formaldehyde shown in Figure 2.18 at about 2ms coincides with a slight temperature increase seen in Figure 2.17. The final hot flame ignition happens very quickly near the end of the simulation and can be seen by the sharp temperature increase in Figure 2.18. The  $\text{CH}_2\text{O}$  concentration at the point of hot flame ignition drops sharply and a cool flame exists further in toward the droplet, while a hot flame ignites near the outer end of the computational domain.

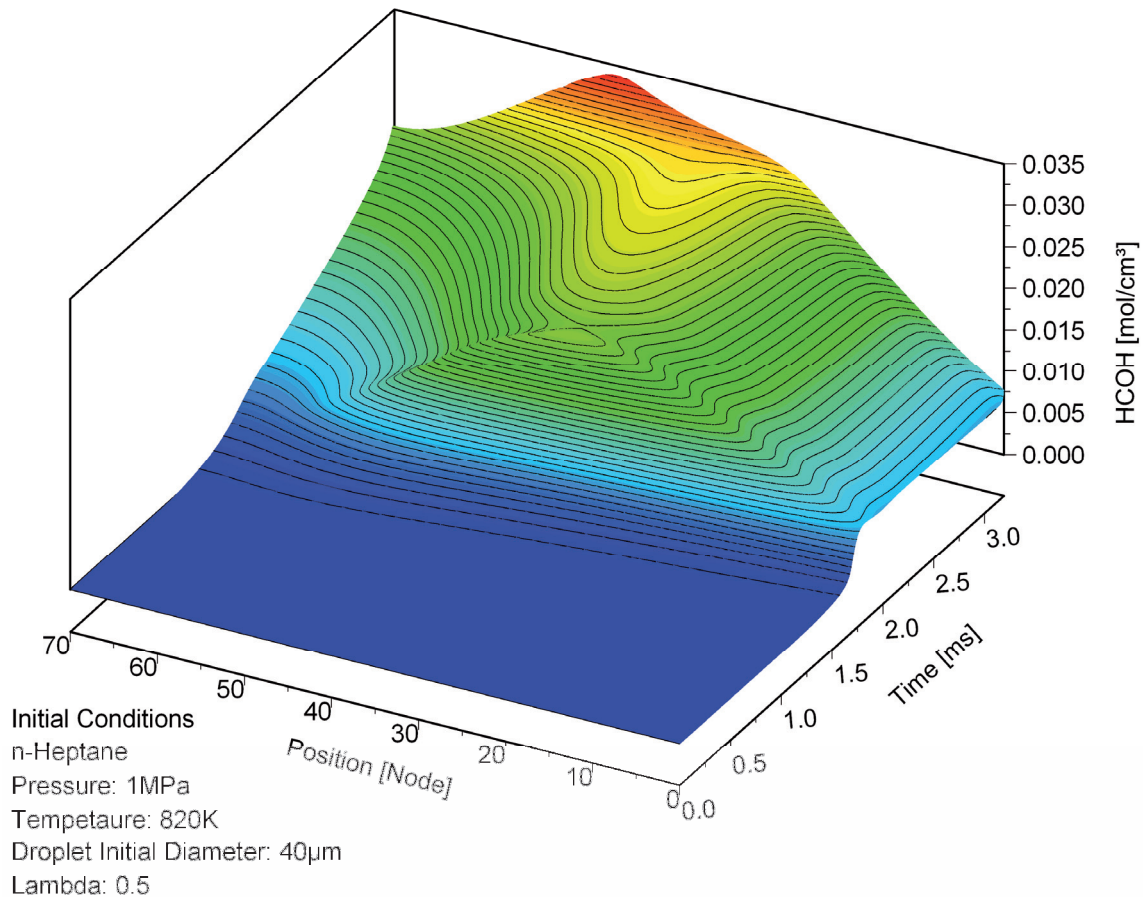


**Figure 2.18** – Gas phase  $\text{CH}_2\text{O}$  development of a 40 $\mu\text{m}$  droplet at  $\lambda=0.5$ , 1MPa and 820K initial conditions

This concludes the short summary and description of the CVS. Armed with the tools and knowledge presented in this and the previous sections the next part of this thesis will concentrate on the experiment (the facility as well as the results) and results from the numerical simulations.

### 3 Experimental Facility

#### 3.1 Introduction

The HWK is a wind-tunnel that functions as a Ludwieg – tube, the basic fluid dynamical laws of which were described in section 2.1. In contrast to normal Ludwieg – tubes however, the flow in the driver section is used for the experiments, while ordinarily the high mach-number flow after the nozzle in the driven section is used for experiments.

The flow in the driver section exhibits high temperature and high pressure with slow to moderate flow velocities. These conditions are similar to those found in many combustion machines (aircraft or power generation turbines for example). The experimental time available is dependent of the length of the driver section, as the conditions behind the established waves are constant until the return of the reflected wave from the closed end.

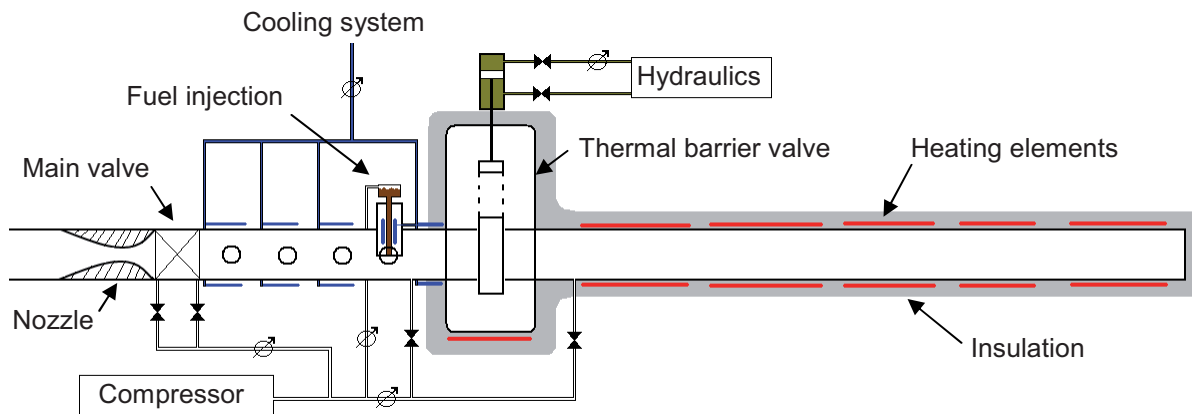


Figure 3.1 – Schematic of main HWK systems

The main components of the facility can be seen in Figure 3.1. The driver section is closed against the surroundings through a fast acting main valve just upstream of the nozzle. The main valve is actuated pneumatically and is fed through the main pressurisation system. The next component upstream is the three meter long test section of the wind tunnel with several observational ports. The fuel injection system is located at the last upstream window of the test section in order to allow sufficient time for the spray to disperse and ignite after injection. The entire test section and fuel injection system are cooled through a water cooling system. This serves two purposes, the first one being mechanical (i.e. preventing distortions of the test section through temperature gradients), while the second reason is to prevent any wall impinging spray to ignite and in doing so falsify the experimental results. In addition to this the large diameter of the test section of 336mm also serves to keep the spray separate from the walls and allows the installation of large test bodies to influence the flow in any desired way.

The test section and the main part of the driver section are separated through a thermal barrier valve. This valve is not airtight but it prevents the heated air from the remainder of the driver section to seep into the test section prior to the experiment. This also serves the purpose of keeping the walls of the test section at room temperature throughout an experimental campaign, for the reasons mentioned before as well as allowing delicate equipment to be installed in and on the test section without the danger of damage or need for additional thermal precautions. The thermal barrier valve (TBV) is opened just prior to the opening of the main valve and start of the experiment via a hydraulics system. This system allows very fast opening times of the TBV (less than 0.5s) in order to minimize convection effects (and

resulting degradation of the thermal profile) once the hot and cold sections of the HWK are connected.

The last main component upstream of the thermal barrier valve is the 40m long heated driver section, which is (as well as the thermal barrier valve) thermally insulated, to prevent heat loss and encourage an even temperature distribution. This section can be electrically heated up to a temperature of 1000K.

Table 3.1 provides an overview of the main operational parameters of the HWK. The next section, will briefly discuss the main components of the HWK and their operating parameters as well as their significance to the operation of the entire system.

<i>Parameter</i>	<i>Range</i>
Operating pressure	2 – 20bar (verified), 2 – 50bar (designed)
Temperature	293 – 1000K
Flow velocity	20 – 85m/s
Experimental time	70 – 130ms
Fuel Injection volume	0.1 – 5ml
Fuel Injection pressure	up to 200bar (absolute)
Fuel temperature	273 – 373 K

**Table 3.1** – Main HWK operational parameters

## 3.2 Overview of Components

The following section provides a short overview of the main components and their operating principle. The verification of correct operation and the effect of most components on the experiments will be discussed in more detail in section 3.7 - Experimental Error, where the correct operation of the main components (with respect to the intended operation described here) will be verified.

### 3.2.1 Nozzle and Fast Acting Valve

The nozzle and fast acting valve shown schematically in Figure 3.1 are shown in more detail in Figure 3.2. These two components are integrated into one main component. The nozzle (red) is used to control the mach number in the test section according to the area law described in section 2.1.2 (see equation (2.1.26)).

The nozzle is interchangeable and currently five different versions of the nozzle are available allowing flow mach numbers of 0.039 to 0.170 to be realised in the test section (see Table 3.2). The actual throat area of the nozzle is composed of the central flow body and the nozzle, as can be seen in Figure 3.2.

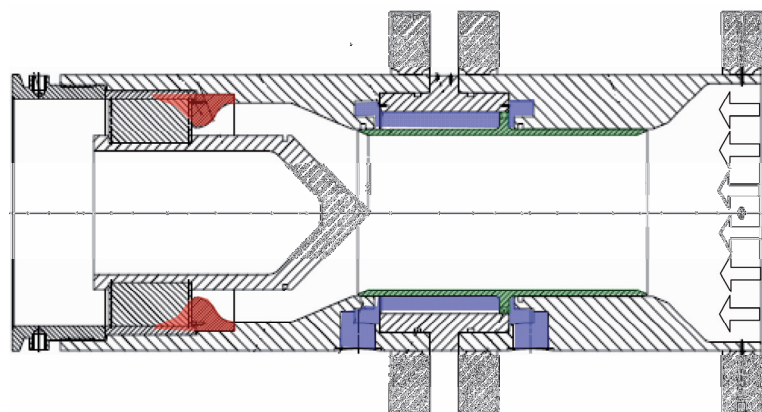


**Figure 3.2** – Fast acting valve and nozzle

The central flow body also acts as main feature of the fast acting valve. This valve is actuated through the main valve sliding ring shown in green in Figure 3.2. In the displayed position the valve is fully open. In the closed position the slider is moved fully to the right and acts as a sleeve to completely close the driver section of the HWK for pressure pre-loading. The slider is actuated via pressurised air (blue areas in Figure 3.2). The compressed air is provided by a reservoir tank that can be pressurised up to 70bar to facilitate different opening characteristics at different operating conditions. The sliding sleeve design of the fast acting valve allows a very fast opening of the entire cross-section of the HWK as the slider can be brought up to significant speeds, before the sleeve leaves the gasket.

<i>Nozzle</i>	<i>Area ratio (A/A*)</i>	<i>Test section mach number</i>
1	15.07	0.039
2	12.03	0.048
3	8.71	0.067
4	8.05	0.073
5	3.48	0.170

**Table 3.2** – List of currently available nozzles

Figure 3.3 shows a plot of the pressure just downstream of the fast acting valve. Initially the pressure in the driven section is one bar (open to the outside atmosphere). Once the fast acting valve is opened a stable operating condition is reached within 20ms verifying the fast opening capability of the valve.

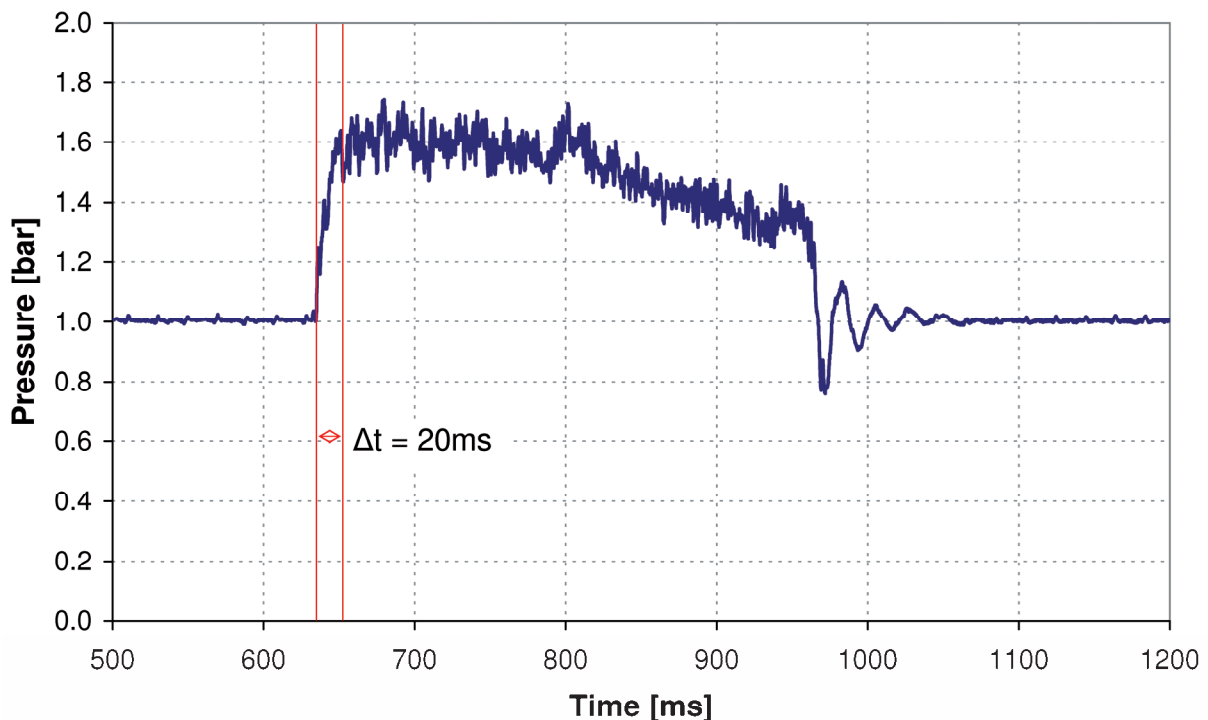


**Figure 3.3** – Pressure after fast acting valve

### 3.2.2 Thermal Management System

The thermal management system (TMS) is composed of four main components, the thermal barrier valve, the heating elements on the driver section, the cooling elements on the test section and the cooling sleeve for the injection section (see Figure 3.4). All of these systems serve a dual purpose: firstly, to regulate and control the conditions in the HWK so that they are appropriate to the experimental parameters required and secondly to maintain structural stability (especially in the vicinity of the driver section sealing gaskets). Due to the large

temperature gradients, large mechanical forces build up in the entire HWK. These have to be minimized and tightly controlled in order to maintain an airtight seal of the HWK. This is accomplished by a combination of the TMS and mechanical means (such as pre-tension loaded bolts and flexible/moving bearings – see Figure 3.5), reducing the loads and distortions.

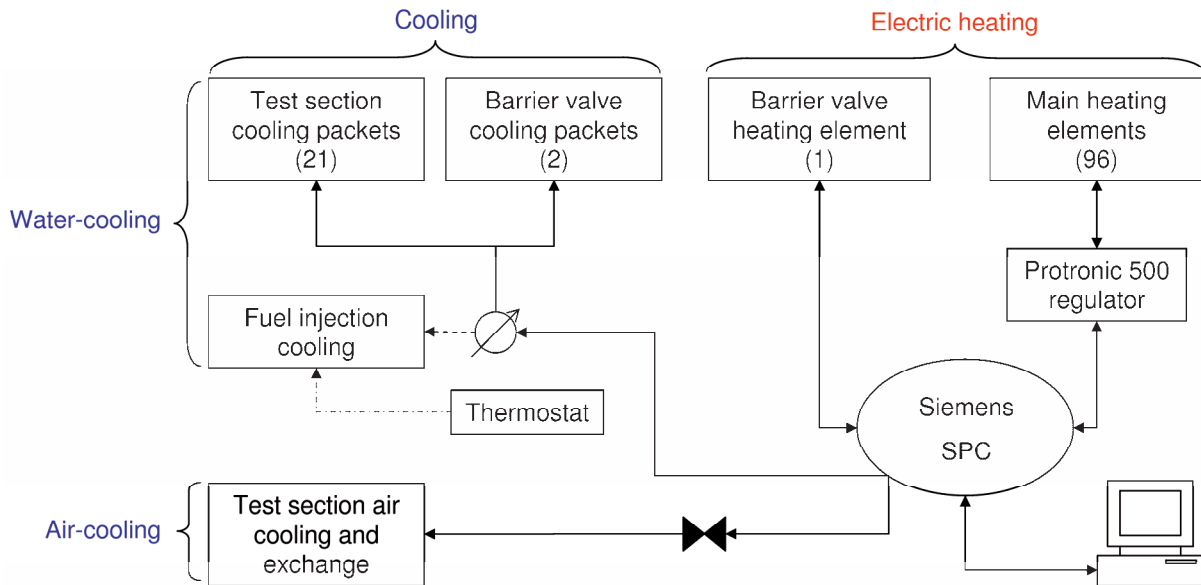


Figure 3.4 – HWK TMS system

The thermal barrier valve serves only to thermally separate the heated driver section and the test section during the heating period. Since this valve is not fully airtight some hot air can seep past the valve in small gaps and cause slow heating of both the valve machinery and test section.

A threefold strategy of cooling and heating is employed to minimise this effect. Firstly, hot air seeping past the thermal barrier valve is forced back into the driver section by a continued replenishment of fresh cold air in the test section and slow draining of hot air in the driver section. Secondly, any heat conduction in the valve material itself is compensated by two cooling packets that are placed at the top of the valve (to prevent overheating of the hydraulics) and the connection flange to the test section.

In addition to this a heating element is placed at the bottom of the thermal barrier valve. Since the heated air that seeps past the valve rises to the top due to convection, a large temperature gradient would build up inside the thermal barrier valve. This gradient is both mechanically as well as experimentally detrimental, and can be reduced by the heating element, which is coupled to the temperature at the top of the valve through a control circuit (Figure 3.5).

During an experiment the test section is flooded with hot gases and depending on the experimental conditions, this hot gas has significant heat capacity, which is slowly offloaded into the metal of the test section after each experiment. This can lead to a gradual temperature increase in the test section (especially the top), which has to be avoided. This is accomplished by two means, first the exchange of all the air volume in the test section right after the completion of the experiment, through the test section air cooling and exchange system. As an additional measure twenty-one cooling packets are distributed evenly along the test section, immediately removing any excess heat from the test section (Figure 3.5).

Another important parameter that has to be kept within tight bounds is the fuel temperature. Since the test section is flooded with heated gases during the experiment some of this heat

also enters the fuel injection system. This might lead to unwanted temperature rises in the fuel and hence the injection system can either be cooled directly via the main water cooling system of the HWK or if an analysis of the fuel temperature dependence is desired it can also be cooled via a laboratory thermostat, allowing a more refined temperature control than the main water cooling system.

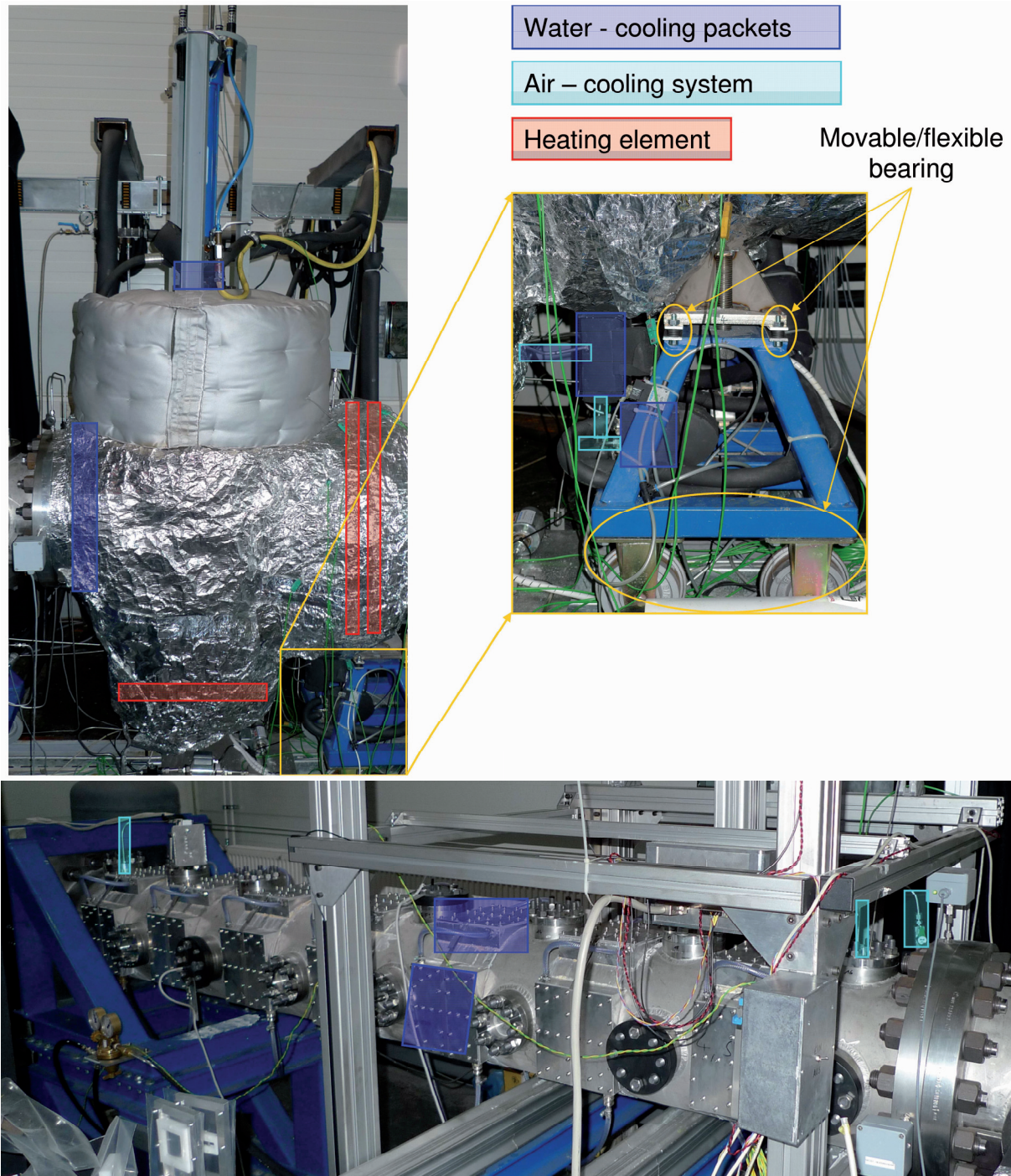


Figure 3.5 – TBV (top) and test section (bottom) with TMS elements

In order to provide the heated air necessary for the experiments the heated driver section is covered with 96 evenly distributed heating elements that consume up to 172kW of electric peak power. These heating elements allow the heated driver section to be brought up to almost 1000K. Since some hot air is leaking through the thermal barrier valve (as was

mentioned before) there is a thermal gradient along the length of the driver section. This gradient is minimized by individually regulating the heating elements in the first quarter, upstream of the thermal barrier valve, compensating for the inevitable heat losses. The heat losses to the surrounding environment are minimized through a thermal insulation layer composed of ceramic wool and aluminium foil. The foil reflects up to 85% of infrared radiation back inwards toward the driver section. The entire TMS is controlled via a stored program controller (SPC) (see Figure 3.4) allowing quick regulation of all relevant parameters.

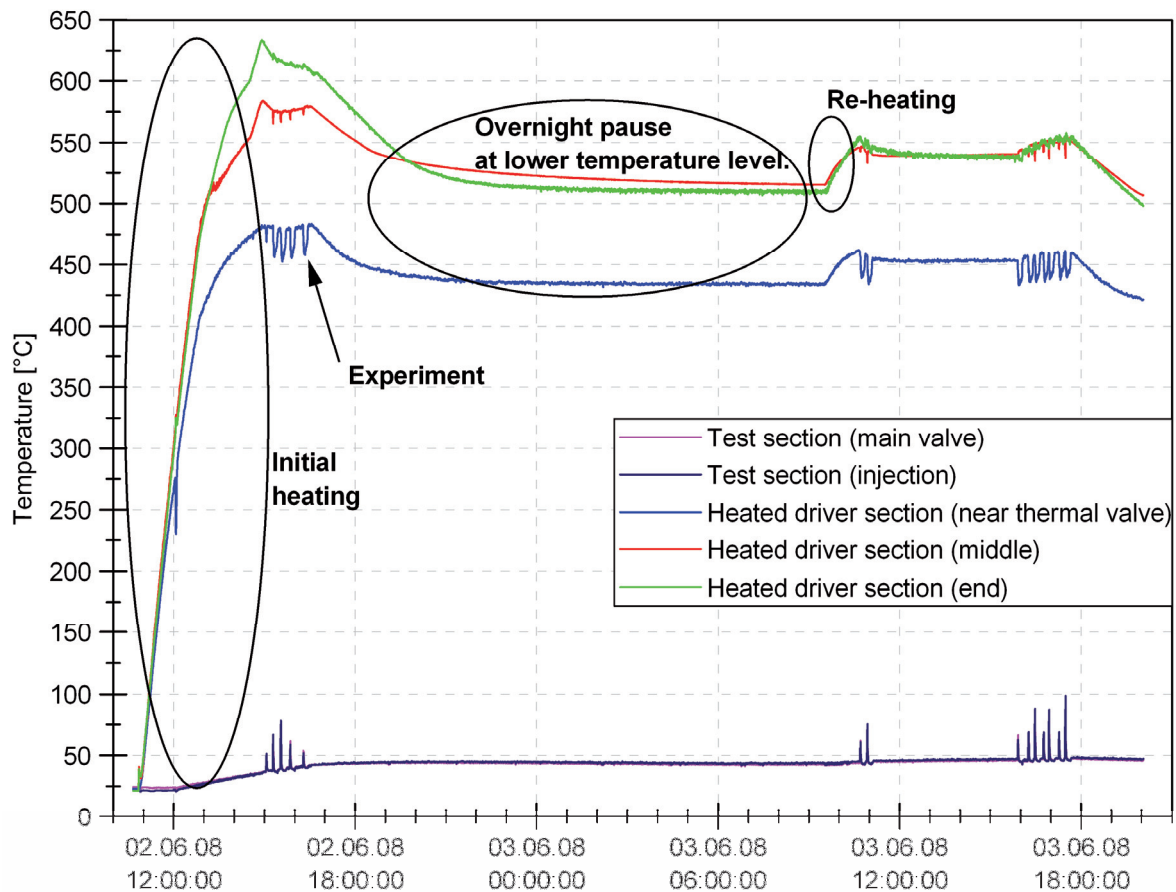


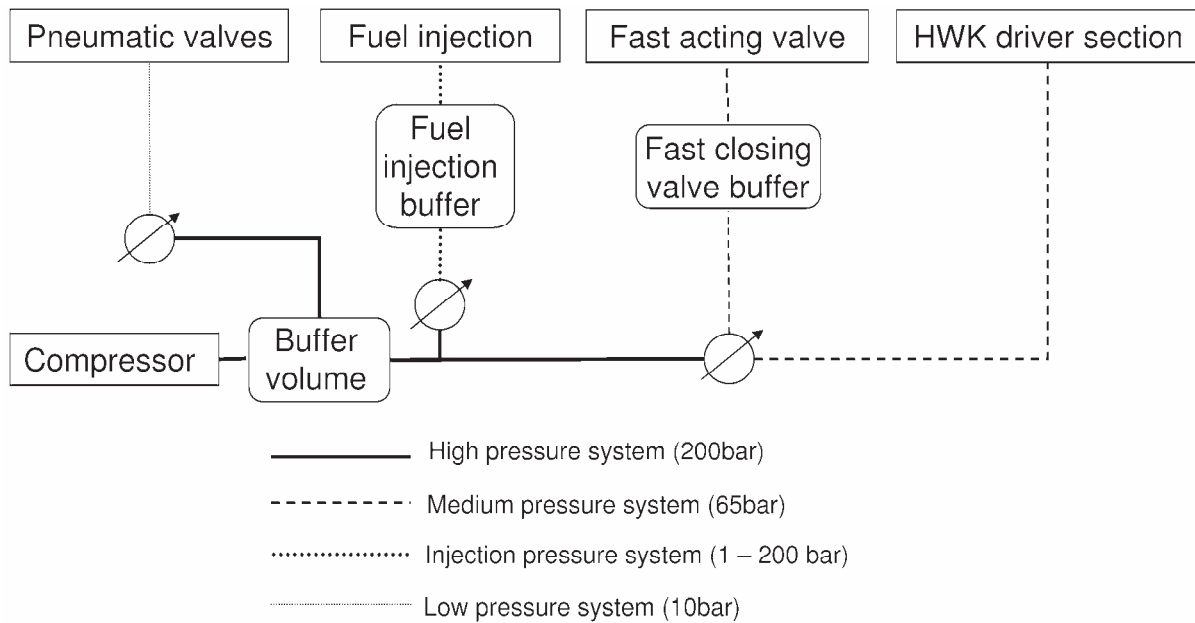
Figure 3.6 – HWK heating profile

Figure 3.6 shows a typical heating profile over a two day experimental campaign with a total of fourteen experiments (spikes). As can be seen the initial heating period takes approximately four hours to reach the desired temperature. The effect of leaking hot air from the heated driver section can be seen, as the temperature near the thermal barrier valve begins to diverge significantly from the overall temperature after about two hours. Also the temperature in the test section increases slightly, but is always kept below 50°C. The heating of the driver section is then reduced overnight for security purposes, but not fully turned off in order to avoid long waiting times for re-heating. After a short re-heating phase of only 1,5h new experiments are conducted. A more detailed look at the temperature behaviour of the HWK and its effect on the experiments will be presented in section 3.7 - Experimental Error.

### 3.3 Pressurisation System

The pressurisation system for the HWK is used to both provide the required pressurised gas for the experiment as well as pressurised air for the operation of various mechanical devices. Hence one high pressure backbone at 200bar supplies three different pressure systems. The first system is the medium pressure system, which provides both the pressure for the HWK driver section as well as the fast moving valve (see section 3.2.1) at pressures up to 65bar. The injection pressure system is used to provide the desired injection pressures and can be regulated at any pressure level up to the maximum pressure of the main pressure backbone. Finally, a low pressure system is used for pneumatically operated valves, which operate various mechanical devices on the HWK.

A significantly simplified schematic of the HWK pressurisation system can be seen in Figure 3.7 – the operation of which and its effects of the experiments will be discussed in more detail in section 3.7 - Experimental Error.



**Figure 3.7** – Schematic of the HWK pressurisation system

### 3.3.1 Fuel Injection System

The fuel injection system is one of the most critical systems in terms of experimental repeatability and stability. The ability to inject varying volumes of different fluids at various pressure levels and to do so consistently is an engineering challenge in itself. As such the injection system has gone through the more iterations and tests than any other component of the HWK.

The current injection system has the ability to inject up to 5ml of any liquid at pressures of up to 200bar and any temperature from 0 to 100°C.

To this end the fuel is manually placed into the injection systems pre-cooled injection tube and this tube is closed. This manual placement of the fuel is done via a syringe with a very long needle (this also allows the exact determination of the amount of fuel to be injected).

The system is then cooled to the desired temperature. Once the desired temperature is reached and all other experimental parameters are set, the fuel is injected into the flow, by opening a magnetic valve to pressurize the entire system. This pressure rise causes a check valve just upstream of the nozzle to open and the fuel is injected into the HWK.

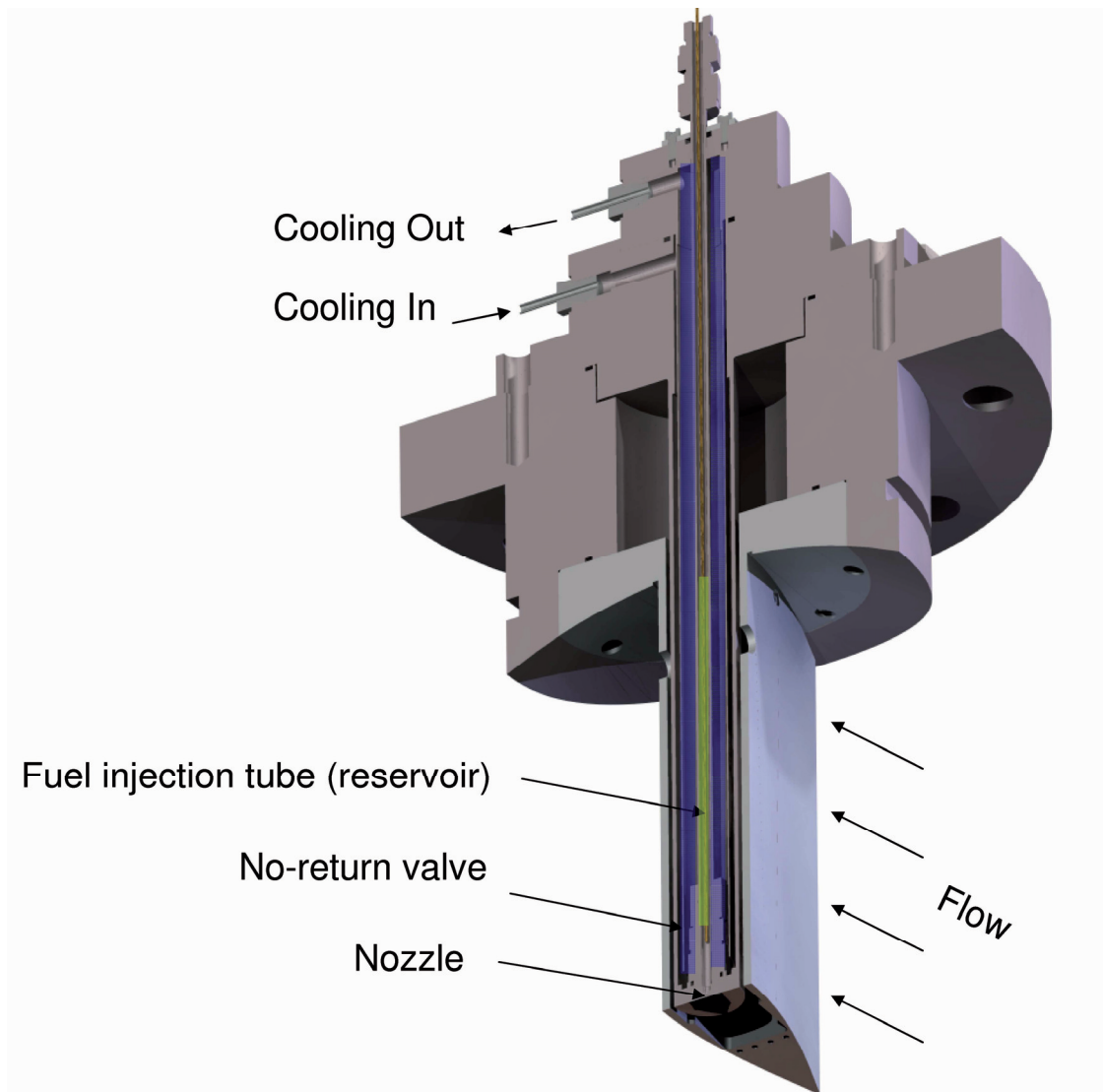
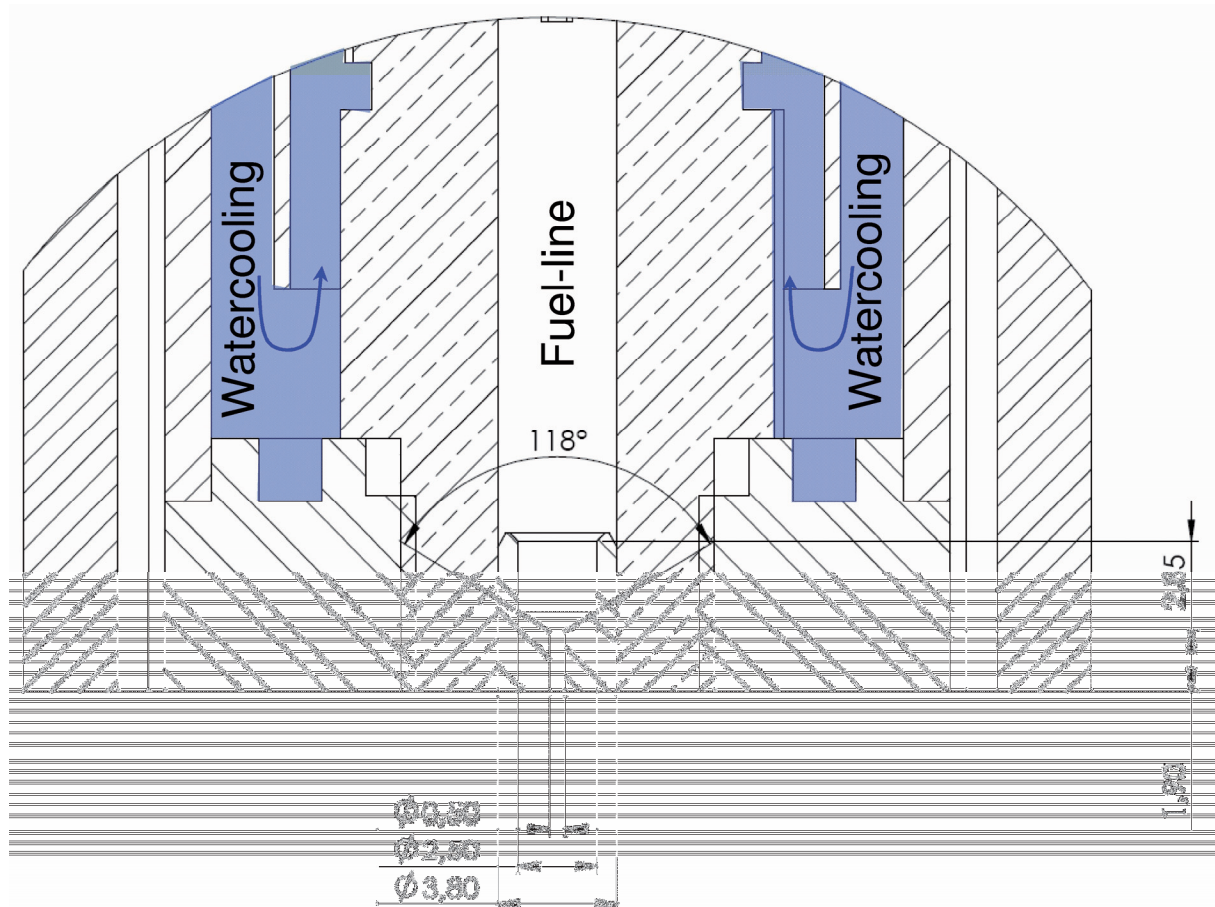


Figure 3.8 – HWK injection system (computer generated image – for visualisation)

To avoid a significant pressure drop in the entire injection system once the magnetic valve is opened, a large reservoir is provided (see Figure 3.7), so that the volume increase and pressure loss due to the injected fuel volume is negligible.

For the experimental campaign of this work the fuel injected is n-Heptane and the injection nozzle is a plain orifice injector with 0.5mm diameter. A more detailed view of the injection nozzle is shown in Figure 3.9. The nozzle itself was constructed from stainless steel (1.4301) and was shrunk – fit into the no-return valve. This ensures that the nozzle can be constructed with tight tolerances, as all sides of the part are accessible to machining, as well as that the nozzle will not deform due to strong temperature gradients as could be the case were the nozzle welded in place.



**Figure 3.9** – Detail cut-out of the injection nozzle and surroundings (all dimension in mm)

The nozzle dimensions were chosen such that the flow exiting the nozzle is as smooth as possible, while being turbulent all the time. The reason for keeping the flow in the turbulent regime all the time is that it is a fairly well defined in this condition [34]. In the laminar and the transition region, the flow exhibits many transient and varying flow conditions. These states are very unstable and can be triggered or destroyed by even the smallest imperfections. In keeping the flow turbulent from the outset, it is ensured that the spray injection parameters are always the same as the turbulent flow regime of a nozzle is fairly stable overall.

There is however one exception to this rule – cavitation; should the local flow pressure fall below the vapor pressure of the liquid, the flow will cavitate, which is usually accompanied by a dramatic decrease in the flow rates of the nozzle. The reason for this is the fact that the regions most prone to cavitation are sharp corners in the flow channel, where the flow has to rapidly change direction. This is usually the case when the large initial fuel line constricts to

the final nozzle diameter (see Figure 3.9). The cavitation bubbles generated at these regions then in turn further restrict the fuel flow, leading to the drop in mass flow rates. In order to avoid caviation, the inlet to the final nozzle opening was tapered and the injection flow conditions were kept within regions where cavitation at such corners could not occur.

Hence the injection flow in this study obeys two main rules:

1. Always well within the turbulent regime to avoid any possible transition phenomena.
2. Flow conditions matched to geometry, so that cavitation is avoided under all circumstances.

### 3.3.2 Ancillary Systems

One of the main problems during the initial operation of the HWK was noise. It was anticipated that normal sonic protection mechanisms would suffice to reduce the noise to manageable levels. During the first experiments it was found that this was not the case. After extensive simulations it was decided to design and construct a large muffling system to minimize the problem. The muffler makes use of acoustic as well as thermodynamic principles.

The supersonic flow exiting the HWK first passes a nozzle to further increase its speed to above Mach 3, creating a high speed flow region at the exit of the HWK preventing any reflections from further downstream to re-enter the HWK and disturb the experiment. In the next step the flow is passed through a diffuser with a central body slowing the flow to subsonic speeds.

The entire flow passages are made of perforated plates behind which absorbing materials are placed (rockwool and gravel). Any reflections are hence significantly reduced. The central flow body was designed in such a way as to produce a maximum of reflections between adjacent walls and as such reducing the incident pressure wave significantly. In addition it prevents additional reflections from later in the muffler assembly from propagating any further into the diffuser assembly.

The subsonic flow is vented through a large standard absorber passage, also composed of perforated sheet and filled with large volumes of sound absorbing material. Finally a rain cover is placed at the top of the assembly; it prevents rain from entering the muffler and is also designed to reflect sound waves back into the assembly.

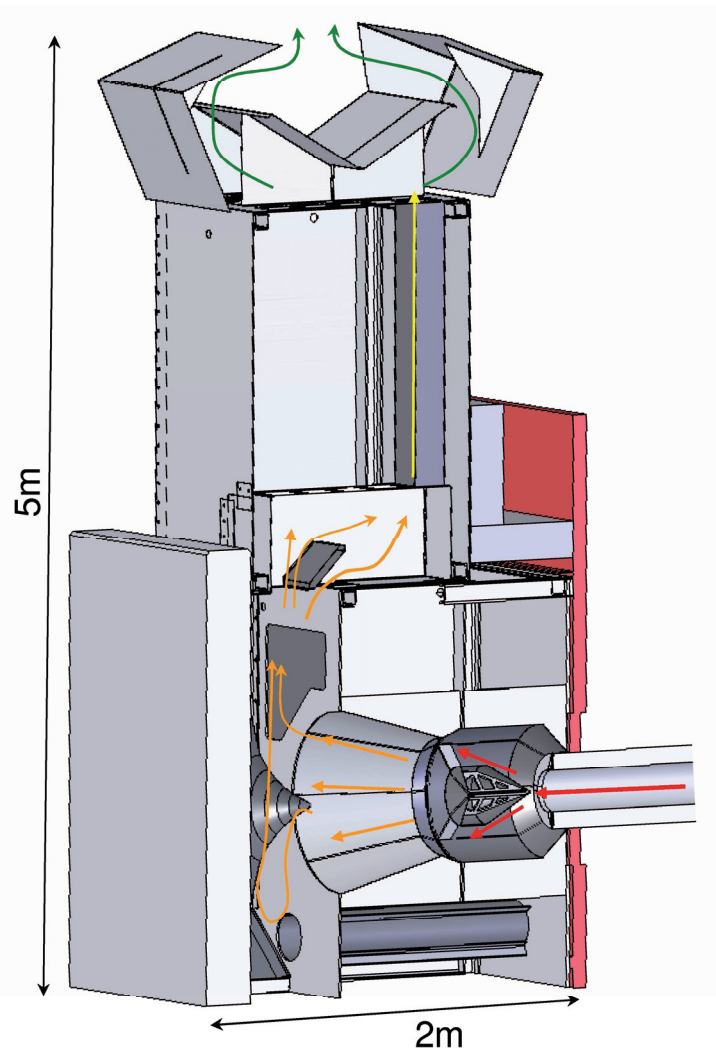


Figure 3.10 – Schematic of the HWK muffler

### 3.4 Data Acquisition

As in any experimental setup, it is of the utmost importance to acquire as much data about the experimental setup and the actual experiment as possible. To this end, the HWK is equipped with a multitude of sensors, which monitor the status of the machine and provide high time resolution data during the experiment.

In total there are over sixty sensors placed on the HWK, which detect temperature, pressure, flow velocity, light intensity and imagery of the experiment in progress, with a sampling rate of up to 10kHz.

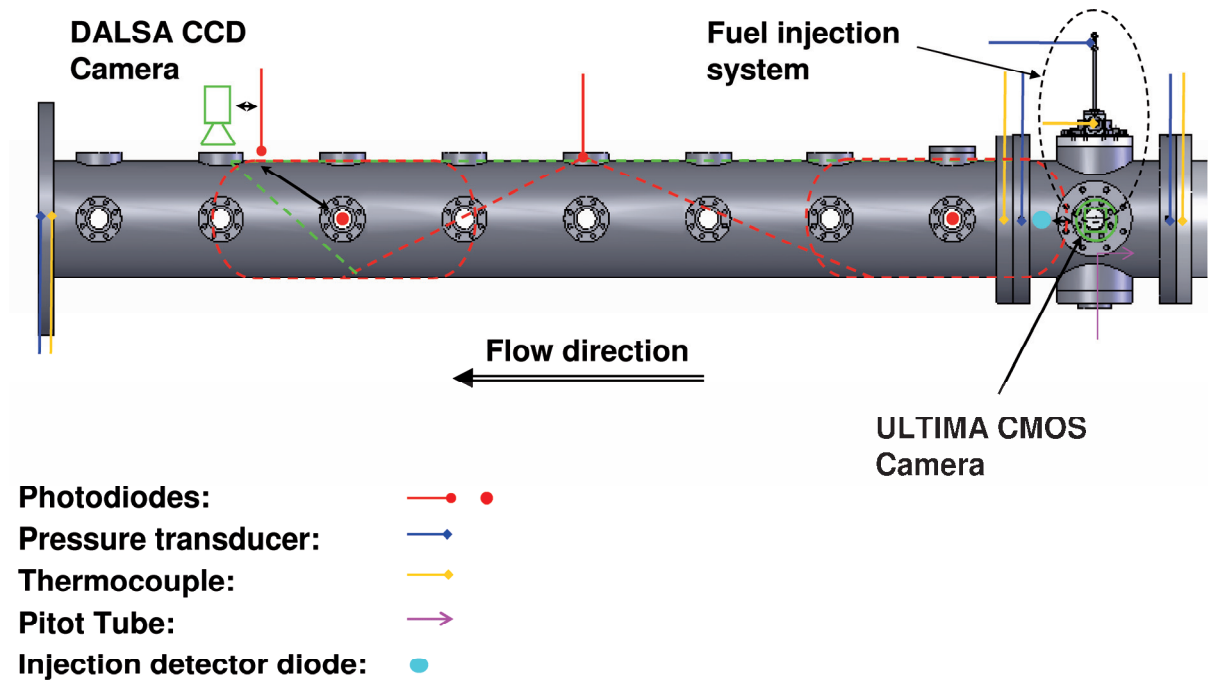


Figure 3.11 – Sensors, their position on the test section and their field of view

The main goal of the experiments in this study is the measurement of the induction time. This is done in the test section, immediately downstream of the injection point. Figure 3.11, shows the types of sensors that are used and their positions along the test section. A schematic of the total data acquisition system can be seen in Figure 3.12.

These sensors perform two main functions, firstly the characterization of the flow and secondly the detection of the spray injection and ignition events.

To perform the first task three pressure and three temperature transducers are placed in the test section. These sensors establish the temperature as well as the static pressure of the flow. In order to measure the flow velocity a pitot tube is used. Since the total experimental time available is only about 100ms it is vital to obtain as much data as possible during this time and hence a high time resolution is required. These sensors are all sampled with 10kHz, allowing a resolution of 0.1ms per data point and 12bit digitization.

The pressure transducers as well as the thermocouples were chosen to have the highest possible response time, so as to support the high sampling by the data acquisition system.

The thermocouples of type – k have a very low response time of only 4ms. This is achieved via very fine wires (0.0127mm diameter), which are welded to larger thermocouple wires and fixed in place with ceramic cement, making the entire assembly very durable. A detailed description of the thermocouple employed can be found in the appendix section 6.1.

The pressure transducers have a large full stainless steel diaphragm in order to withstand the high temperatures they are subjected to. Additionally a custom made temperature compensated amplifier was used to precondition the sensor signals for the data acquisition system. The pressure sensor and its amplifier were chosen and constructed for maximum speed and hence a response time in the millisecond range is possible. A description of the type of sensor employed can be found section 6.2.

In order to detect the point of fuel injection, two methods have been employed for the experiments. The first method was to use a high speed CMOS camera, operating at 8000fps to observe the fuel injection event. This method allows a determination of the injection time to within 0.125ms and in addition this camera allows the observation of the spray structure. The information about the fuel spray overall structure is important for determining the mixture ratio, the exact procedure of which will be explained in section 3.6.1.

To improve on this, a second system was devised. This system used a photodiode, which was focused on the injection location with the appropriate optics, while the entire scene was backlit by a high power LED. At the instant of injection, the fuel jet blocks some of the light from the backlight facility, causing a noticeable drop in the output of the detector photodiode. This photodiode allows the injection to be determined to within 0.1ms (10kHz sample rate). In addition, the LED detection method eliminates the danger of bias, as compared to the manual analysis of recorded injection imagery.

<i>Position</i>	<i>Sensor type</i>
Closing flange – end of heated driver section	3x thermocouple 1x pressure transducer
Rear half of the heated driver section	8x thermocouple
Middle flange – between rear and front half of the driver section	3x thermocouple 1x pressure transducer
Front half of the heated driver section	8x thermocouple
Flange between thermal barrier and heated driver section	1x thermocouple 1x pressure transducer
Thermal barrier valve	10x thermocouple
Behind fast acting valve	1x thermocouple 1x pressure transducer

**Table 3.3** – Additional sensors and their approximate positions on the HWK

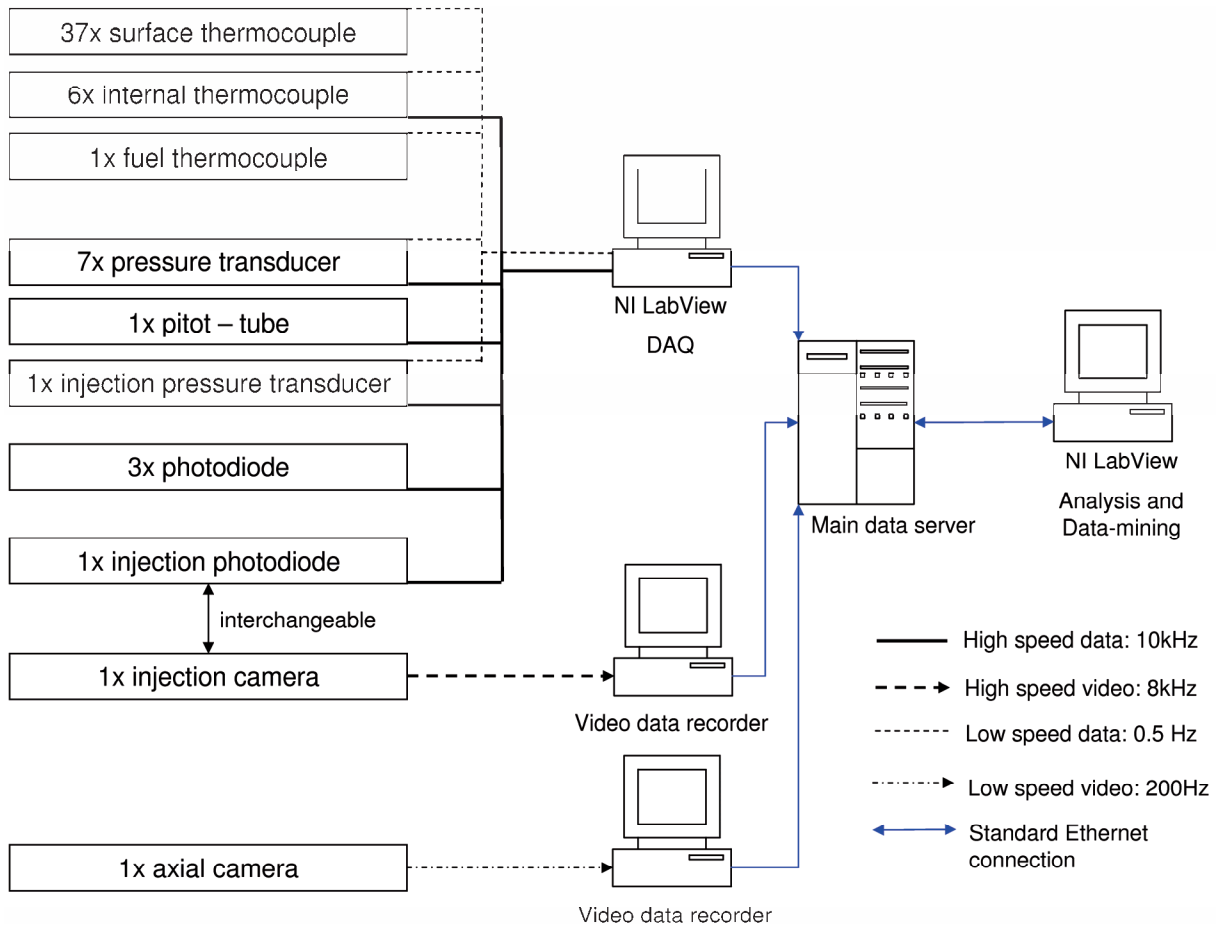


Figure 3.12 – HWK Data acquisition system schematic

To detect the time of ignition, three high-speed, high sensitivity photodiodes (of the same type as the fuel injection detection diode) are used. The location of these can also be seen in Figure 3.11. They are placed in such a way as to have overlapping fields of view. These photodiodes are also sampled with 10kHz, allowing the determination of the ignition event to within 0.1ms. A description of the type of photodiode used and its sensitivity can be found in section 6.3.

The last downstream photodiode is interchangeable with a CCD camera operating at 200fps. If this camera is in operation the photodiode is placed in its secondary location as indicated in Figure 3.11. The top view port (location of the CCD Camera or photodiode), is equipped with a 45° prism, which allows a view along the axis of the HWK.

The CCD Camera is very IR sensitive and hence allows the observation of the spray against the hot background of the HWK and the subsequent ignition event. Since the frame rate of the camera is significantly lower than the rest of the data acquisition system this information is mainly of qualitative interest and is not used to determine the exact time of ignition. Nonetheless the video material obtained from the camera, allowed the observation of many interesting ignition phenomena (see section 4.1.7).

In addition to this fast data acquisition system that is only active for about 3-5 seconds during the actual experiment, a much slower system was put in place to monitor the overall status of the HWK. This system uses some of the fast sensors mentioned above, as well as several other sensors that can be seen in Table 3.3. These are all sampled at 0.5Hz as soon as the HWK enters operational mode and sample for as long as the experimental campaign continues (several days to weeks). The data from these sensors serves a dual purpose, both

providing valuable information on the state of the experimental facility for later use in the analyses, as well as engineering related information for the continued safe operation of the HWK.

### 3.5 Experimental Timeline

Every experiment follows a precise timeline. A simplified example of this can be seen in Figure 3.13. This sequence of events is not only vital for the safe operation of the HWK, but also assures that the experiments are all conducted in a similar fashion and hence repeatability is ensured.

The initial sequence is controlled by the main HWK SPC and starts by initiating a ten second countdown. During this time, all air cooling systems mentioned in section 3.2.2 are shut down (ensuring the settling of the gas) and an alarm is sounded to warn of the imminent experiment. Shortly before the end of the countdown the data acquisition system described in the previous section is triggered. Since this system is in a continuous logging mode with a frequency of 0.5Hz it can take up to two seconds for the system to indicate readiness. Once this is received by the SPC the TBV is commanded to open and once confirmed open by a sensor, the control of the entire facility is relinquished to an electronic cam switch.

The electronic cam switch is operated at 10kHz giving it a resolution of 100µs per cycle. This is much faster than the 20ms per cycle that the SPC is capable of, and enables a timely control of all parameters during the limited 100ms that are available for experimentation.

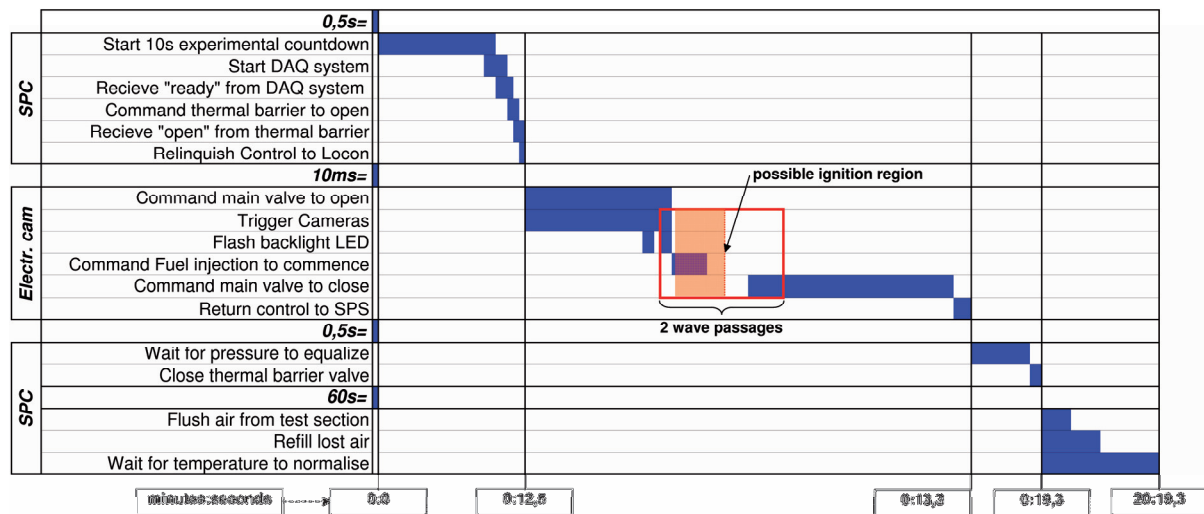


Figure 3.13 – Experimental timeline

The first action of the cam switch is to command the main valve of the HWK to open. This can take several milliseconds, depending on the pressurisation settings of the main valve. At the same time all camera systems on the HWK are triggered to commence recording. Shortly before the injection system is activated, the main backlight system for the injection section (mentioned in section 3.4), is switched off twice. This is done to verify the correct operation of the detection devices (be it cameras or photodiodes) and to synchronise the camera timelines with the main experimental timeline.

Immediately after the last flash of the backlight system injection is initiated and the fuel is injected into the flow following the first expansion wave passage. Ignition can then be observed any time between injection of the first fuel and the return of the expansion wave to the injection section. A second wave passage through the HWK is allowed to occur at this point, during which time the main valve is commanded to close (this again can take several

milliseconds). The second wave flushes any remaining fuel vapour and combustion products out of the HWK. Although this almost doubles the required refill air, it was taken as a precautionary measure to ensure fresh and equal conditions for each experiment. The final command in the electronic cam switch returns the control back to the SPC.

The SPC then monitors the pressure in the HWK, to ensure proper closing of the main vale. Once this is ensured the thermal barrier valve is commanded to seal the heated driver section from the test section.

Upon the closing of the TBV, the air cooling system in the TMS is commanded to circulate fresh air into the test section and remove the heated air from the experiment, by opening pressure relive valves at the top of the test section. This is not only a second measure, to ensure fresh air for the next experiment, but also to remove the heated air as quickly as possible to minimize the thermal stresses on all components of the test section. At the same time the air in the HWK is replenished for the next experiment.

The final step in the HWK experimental timeline is to wait for the required temperature for the new experiment. This can take several minutes depending on the amount of air replenished and settings for the new experiment.

### 3.6 Data Analysis and Handling

The data acquired by the data acquisition system is stored for further analysis in a central server system (see Figure 3.12), which runs a MySQL database. This database does not only contain the raw data and logging files of each experiment but also more than 75 parameters pertaining to the setting of the HWK, as well metadata (more than 120 sets per experiment) resulting from the analysis of each experiment. The database as well as the data analysis program and retrieval GUI (LabView environment), where specially written as part of this thesis in order to facilitate a comprehensive analysis of the over 800 experiments that were conducted to date.

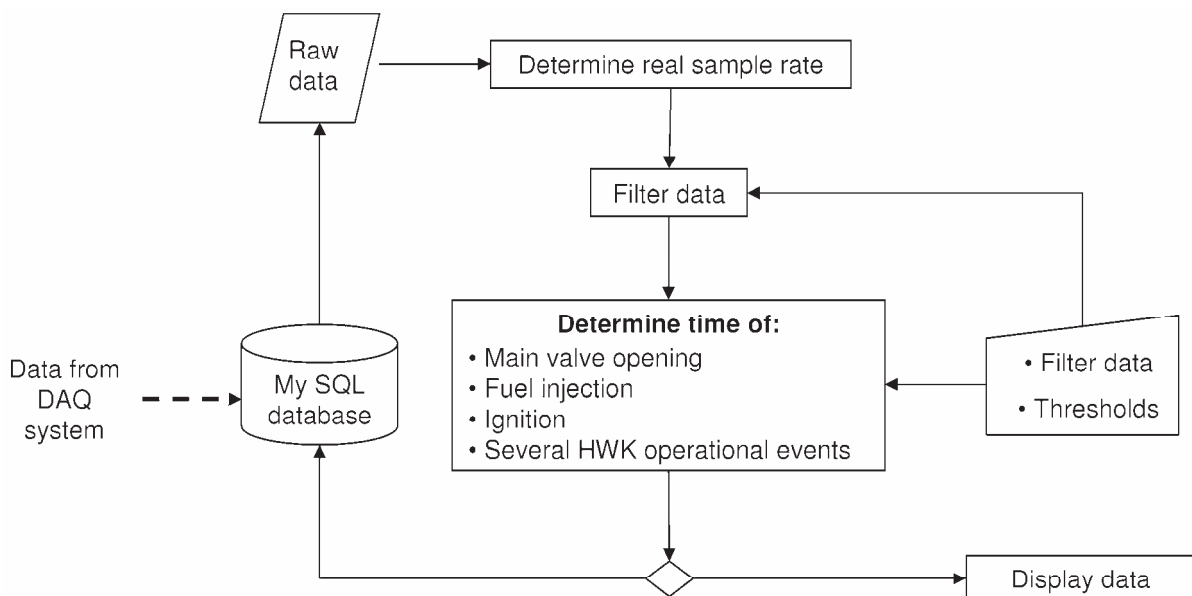


Figure 3.14 – Timing analysis flow diagram

The analysis of the experimental data is split into two parts: a “timing analysis”, used to determine all time critical events during the experiment and a “condition analysis”, which

then extracts and computes all relevant experimental conditions from these timing events. Simplified flow diagrams of the two can be seen in Figure 3.14 and Figure 3.17 respectively.

Since the condition analysis requires data from the timing analysis, the latter always precedes the former in the order of the analysis.

The timing analysis is meant to extract time critical events from the experimental data and starts by retrieving the raw data of the experiment from the database. The first critical parameter to be checked is the sample rate. While the National Instruments Data Acquisition Card was set to record at a constant sample rate of 10kHz, this is not always the case due to different processor loads and other random computing events. Hence the Electronic cam switch system was set to deliver a 5Volt calibrated on/off signal, which is recorded in addition to all channels from the HWK sensors. Since the Electronic cam switch timer signal is supplied by a highly stable signal generator and has a known setting, this signal can be used to calibrate the exact sampling rate that was achieved by the DAQ card. This re-adjusted sampling rate is the used for all further calculations.

The next step in the analysis process is to filter the noisy raw data. Since all sensors were optimised for recording speed their signals can be fairly noisy. This is compensated by digitally filtering the recorder signal. The filtering is done with an elliptic filter, which provides a very sharp transition between the pass- and stopband, as well as minimizing the peak errors in both bands [59].

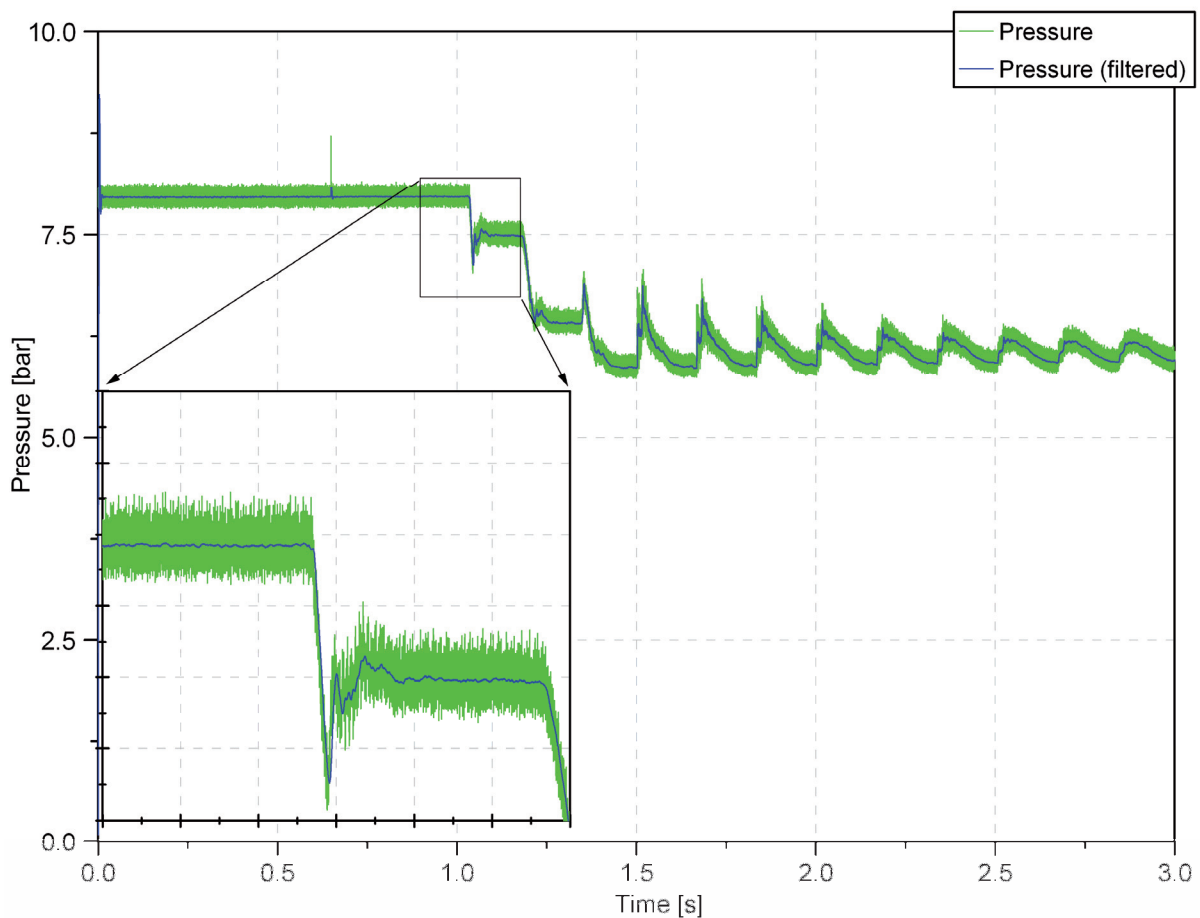


**Figure 3.15** – Effect of elliptic digital filtering (Lowpass @ 200Hz, 1<sup>st</sup> order, 5dB ripples)

The result of such a filtering operation can be seen in Figure 3.15. The graph shows the output of the pressure sensor near the injection point, while the green line is the raw signal and the blue line the filtered result. As can be seen the filtered signal is of much better quality. The

filtering was done as a lowpass filter with 200Hz as cut-off frequency, as it is unlikely that any flow phenomenon will exceed 200Hz at the low flow velocities present in the HWK. The parameters of the filter, as well as the threshold values for the detection of the key events are set manually. The detection of these events is the next step in the analysis and is mostly done with the help of threshold values, manually entered by the user. An example of this can be seen in Figure 3.16. The graph shows the pressure downstream of the fast acting valve and indicates when the main valve has opened. This information is used to determine the opening time of the HWK. The red line indicates the typical threshold value of 1.1bar (10% increase above ambient pressure) that was used in this type of analysis. It is very important to note that this threshold was kept consistent throughout the analysis, in order to maintain comparability.

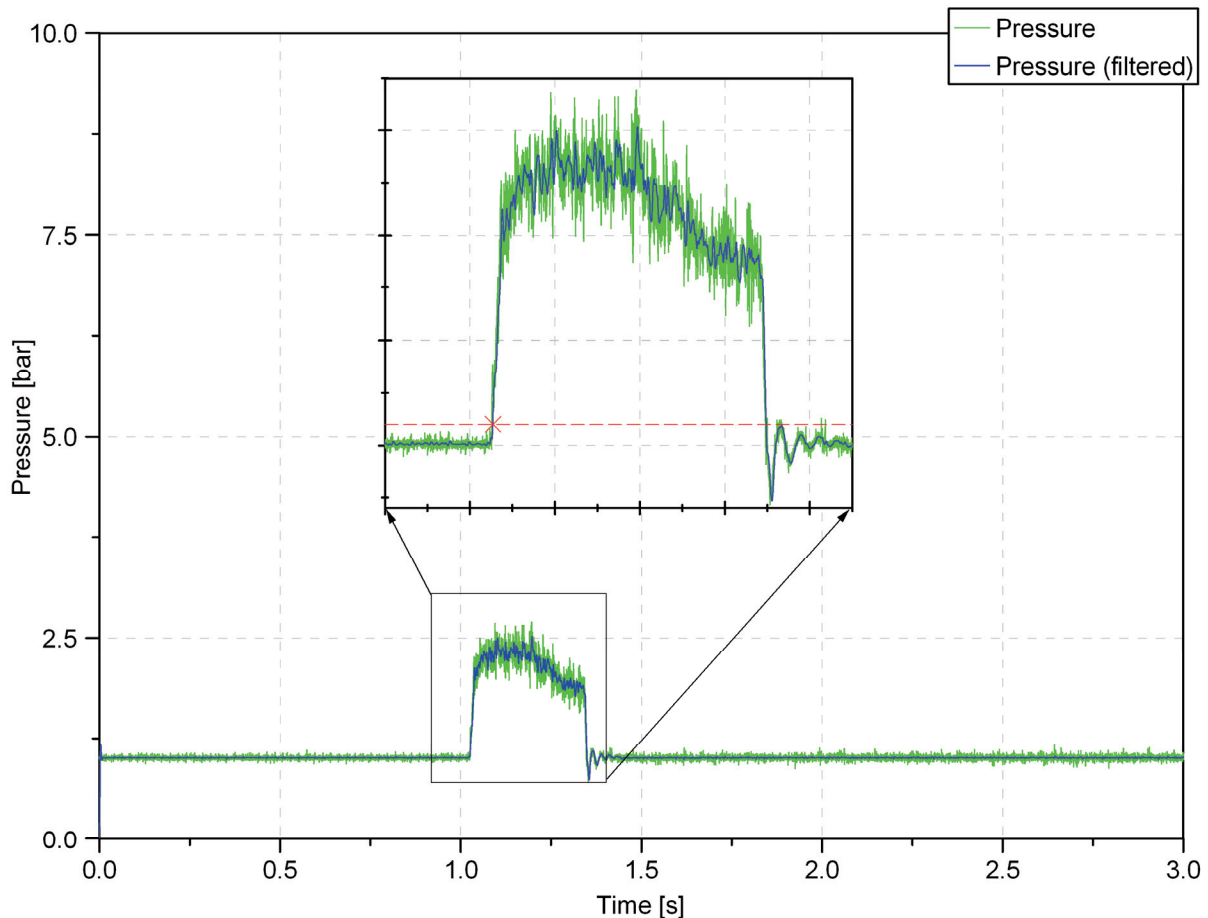


**Figure 3.16** – Pressure downstream of the fast closing valve and threshold value (red)

This type of threshold detection was used for all other timing parameters obtained in the timing analysis, except for ignition time.

Since ignition time is the most critical parameter it was important to ensure that consistency is maintained throughout its detection process. This is especially important as the photodiodes used for ignition detection are also sensitive in the IR spectrum (see section 6.3), and are hence susceptible to the background thermal radiation of the HWK. Since this background is dependent on the temperature set during the experiment, it is variable and consequently a fixed threshold would falsify the results. This is compensated by using a percentage threshold, where an ignition is registered if the output value of the photodiode is a certain percentage above the previous average value. In addition to this the signal is further filtered by a Savitzky-Golay filter [60] (10 side points and of second order) prior to the threshold detection, in order to avoid the detection of unwanted signal spikes. The standard threshold used for detection in this work is an increase of 1% above the previous average.

In addition to the above values several engineering parameters (such as timing marks, valve operational times and mass flows) are extracted from the experimental data at this point. This additional information is not only helpful in the correct and precise operation of the HWK, but also allows a detail verification of the influence of several machine parameters on the experiment. All results of the analysis are then displayed and saved in the database as metadata and can be quickly accessed and searched for further use.

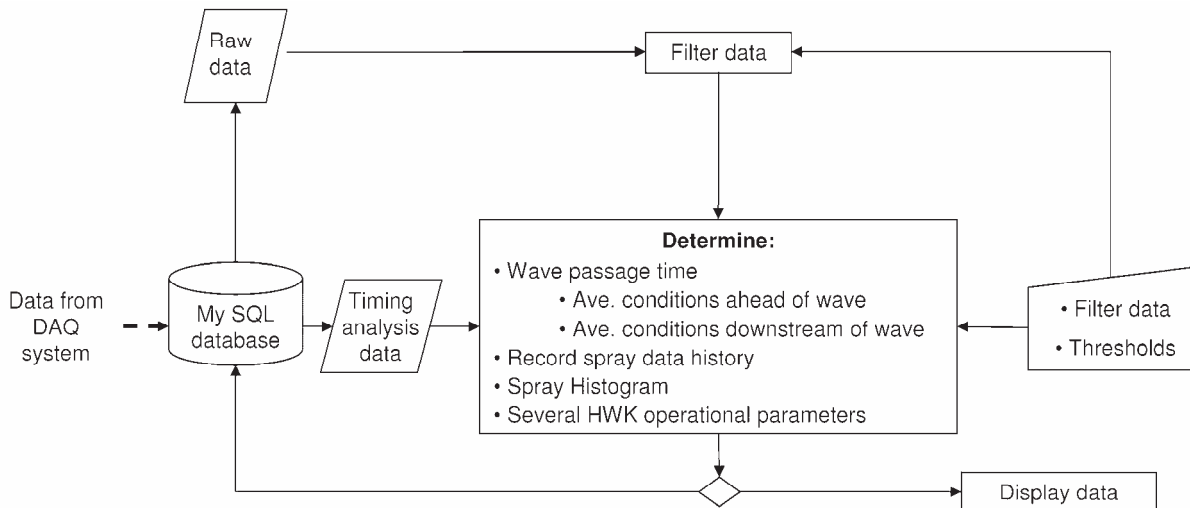
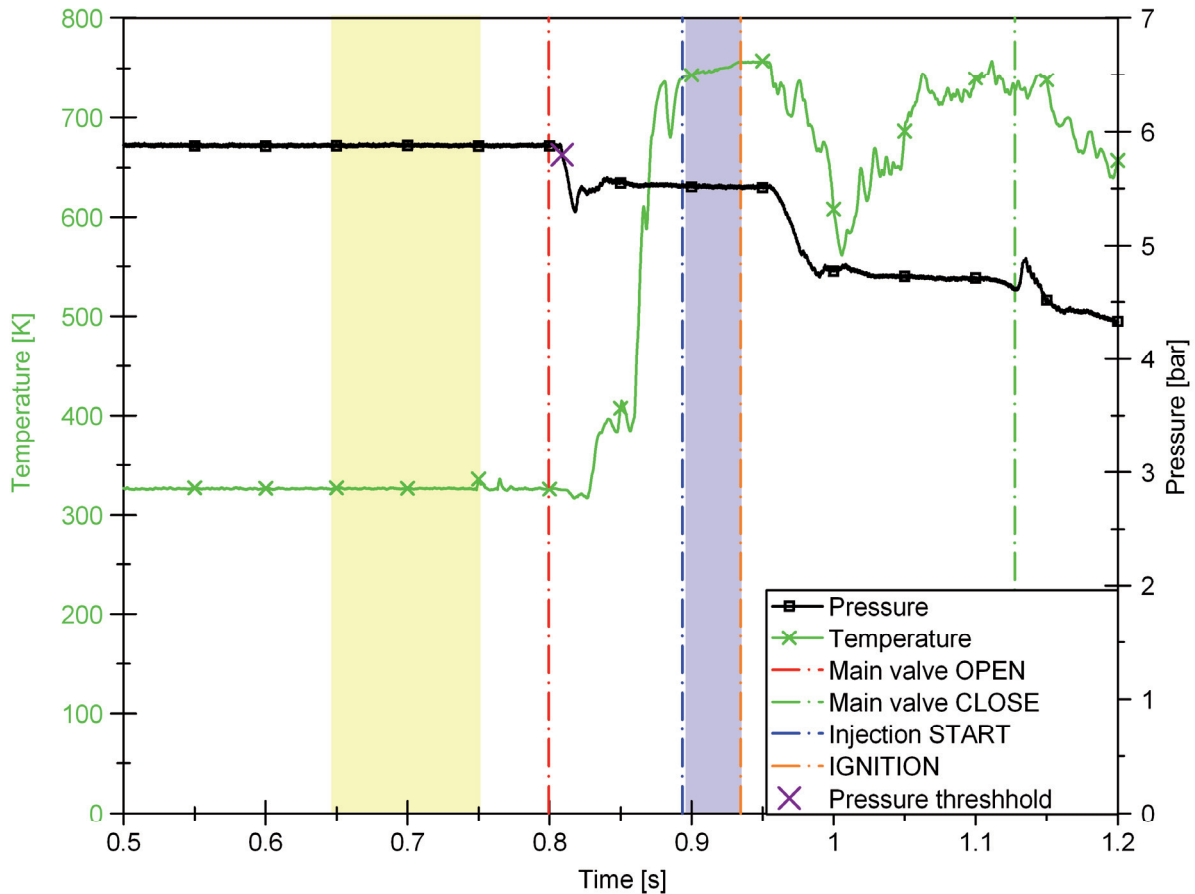


Figure 3.17 – Condition analysis

Once the timing analysis is complete, the conditions during the experiment can be analysed. For this purpose, raw data is again read from the database and filtered in the same manner as the timing raw data. Afterwards, the timing events from the timing analysis are extracted from the database and user specified threshold values are used to extract several parameters from the experiment.

An example of this analysis can be seen in Figure 3.18. The black graph shows the results of the analysis of a pressure curve and was recorded at the injection location. As can be seen the initial pressure, prior to the passage of the expansion wave is 5.87bar. This pressure then drops to 5.5bar after the passage of the wave, which was the desired experimental pressure in this case. The dashed vertical lines indicate timing events extracted from the timing analysis, indicating the opening of the main valve (red), start of injection (blue), ignition (yellow) and closing of the main valve (green). The user defined threshold value for the detection of the wave is indicated with a lilac cross. Around this threshold value the user can specify a “gap” period in which no average values will be taken. This is to ensure that only steady flow conditions are used for finding the appropriate averages. These averages are indicated by the yellow and blue bars. The yellow bar indicates the average pressure before the passage of the wave. In general values from 100ms are averaged, where the end of the averaging period is defined by the beginning of the user specified waiting gap near the pressure jump due to the wave passage.

The second averaging region is the average values that the spray has been subjected to. Hence the averaging is done from the time of injection to ignition. If no ignition is detected a user specified averaging time is used instead. The start of the averaging is always defined by the time of first fuel injection, unless no injection was detected. Then the end of the user specified gap (near the pressure jump) is used as starting point.



**Figure 3.18** – Data analysis software timing events (analysing experiment number 525)

The green graph shows the temperature near the injection point. The same timing data and colour coding is used to indicate the critical events.

As can be seen the temperature in the test section is near 50°C prior to the test (yellow region). Once the main valve is opened it takes almost 100ms for the temperature to reach a stable plateau. This is due to several fluid dynamical effects, which will be discussed in more detail in the next section.

The conditions experienced by the spray (blue region), will be called “spray history” from now on. The spray history for the above experiment is shown in Figure 3.19. The goal for the values of spray history is to be as smooth and even as possible. As can be seen for this example, the flow velocity as well as the pressure can be kept within fairly tight bounds, while the temperature does have a variation (increasing as the experiment continues). The reasons of this will be further explained in the next section. The variations between the maximum and minimum points for each of these curves are also an indication of how well the experiment proceeded and hence are also recorded by the analysis software. These values are known as “spray history variations” and in this case there is a maximum variation of pressure of 0.07bar, velocity varies maximally 0.42m/s and temperature 17.04K. These values provide a further means of comparing experiments and must be kept within the same tight bounds, so as to keep consistency within the individual experiments. Further details on these parameters can be found in the following sections where the estimation of the experimental error will be discussed as well as the section of the discussion of the results.

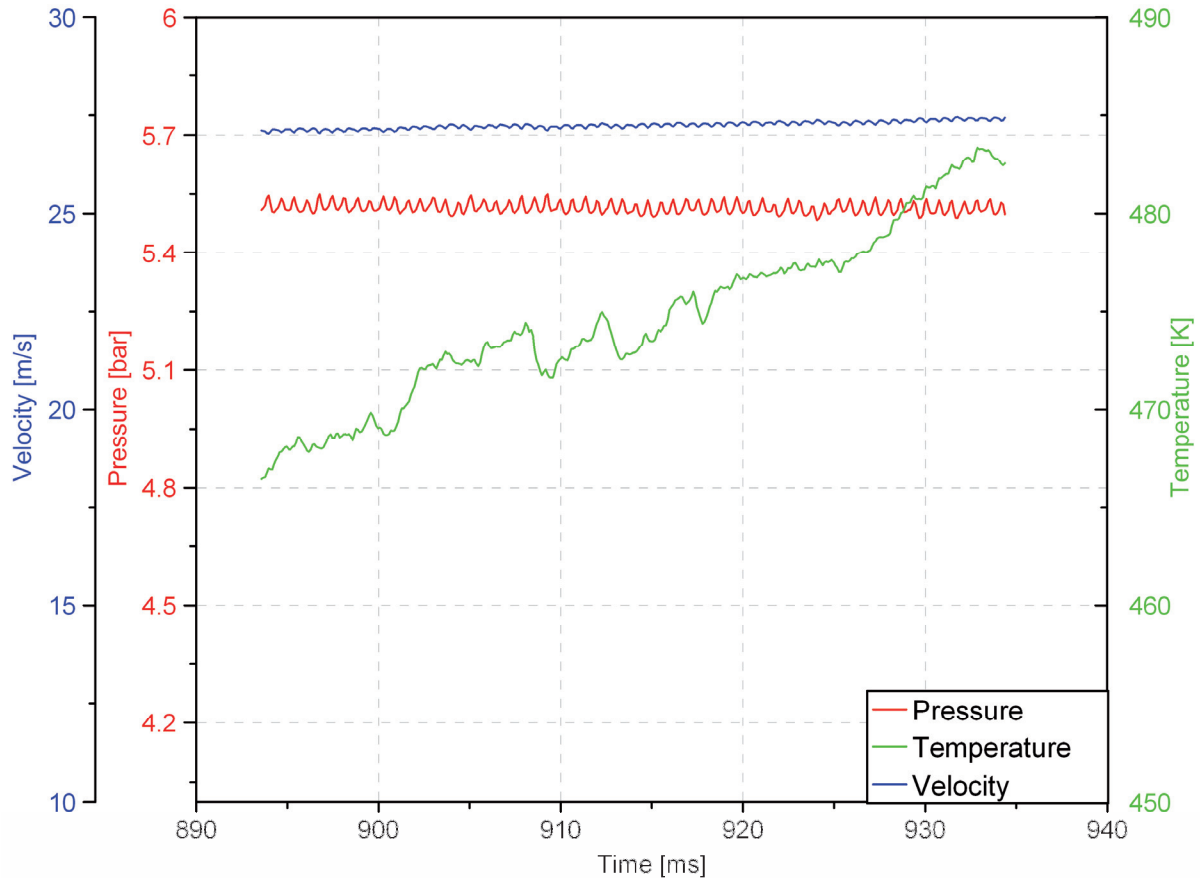


Figure 3.19 – Spray history for experiment 525

Finally, a wealth of additional engineering parameters are extracted and calculated from the experimental raw data, such as speeds of sound in the HWK and data concerning the propagation of the expansion wave. This information (as in the timing analysis) serves both to verify the correct operation of the experiment and helps in the identification of experimental peculiarities.

The entire information from the condition analysis is again both displayed for the user to review as well as saved in the database for later usage.

The advantage of the implemented database system is that all experiments conducted can be comprehensively searched for patterns with any imaginable combination of parameters in a very short time. This allows a very exact analysis of the trends in the experiment and also helps to identify and eliminate factors that might be detrimental to the final results.

### 3.6.1 Determination of the mixture ratio

The exact determination of this parameter is difficult, due to the operating characteristics of the HWK as a blow down Ludwig – tube.

As mentioned above all previous studies on the autoignition of fuels, were done in continuous flow devices or piston machines. These have the decisive advantage that the instantaneous global mixture ratio can be easily determined by directly measuring the inputs of fuel and air. This was possible because the test sections (in the continuous flow devices) are relatively small and the relative amount of fuel injected was large, meaning it was reasonable to assume that the entire air would participate in the combustion process as the fuel spray would

essentially fill the entire cross-section of the test section [7]. Nonetheless this still does not preclude the possibility of locally different mixture ratios in the test section. In fact the general problem of a global mixture ratio is the gross simplification of the local inhomogeneities into one average value.

Quite apart from the problems of a global mixture ratio in any experimental setup, the above procedure of equating entire in- and outflows is not possible due to two reasons in the HWK. First it is not a continuous flow device and as such has no actual inflow of air and second, the test section is very large in comparison to the fuel spray dimensions (to avoid any boundary layer effects).

Hence, if one were to determine the air-mass flow from the free-flow velocity and assume that the entire test-section air column (taking injection time as an indicator) were involved in the reaction with the fuel spray, one would get nonsensical values of  $\lambda > 70$ , which is obviously far too lean to ever yield ignition.

This problem necessitated the development of a new procedure to estimate the global mixture ratio. The main assumption that was made is that only the air in the immediate vicinity of the fuel spray will take part in the chemical reactions and hence is the only air volume/mass flow that should be considered for the calculation of the global mixture ratio. This assumption leads to the following procedure for the determination of the mixture ratio:

1. Use of the injection images to determine the fuel injection structure.
2. Identify appropriate theoretical/empirical models for the overall spray distribution in a JICF configuration.
3. Calibrate these models using the actual experimental image data
4. Calculate the volume that the spray interacts with up to the point of ignition or the end of injection.
5. Calculate the air volume/mass that occupies the same volume
6. Calculate the resulting mixture ratio

The first step of identifying the spray structure was done by using an image of the spray injection event and then using a calibration scale to extract the coordinates of the windward and leeward spray lines (Figure 3.20).

This information is then used to fit the following function to the available coordinate data:

$$y(x) = a \left( q \frac{x}{d_0} \right)^b d_0 \quad (3.1.1)$$

Where  $q$  in this case is the liquid to gas momentum ratio given by:

$$q = \frac{\rho_L V_L^2}{\rho_G V_G^2} \quad (3.1.2)$$

And the constants  $a$  and  $b$ , which have to be determined experimentally.

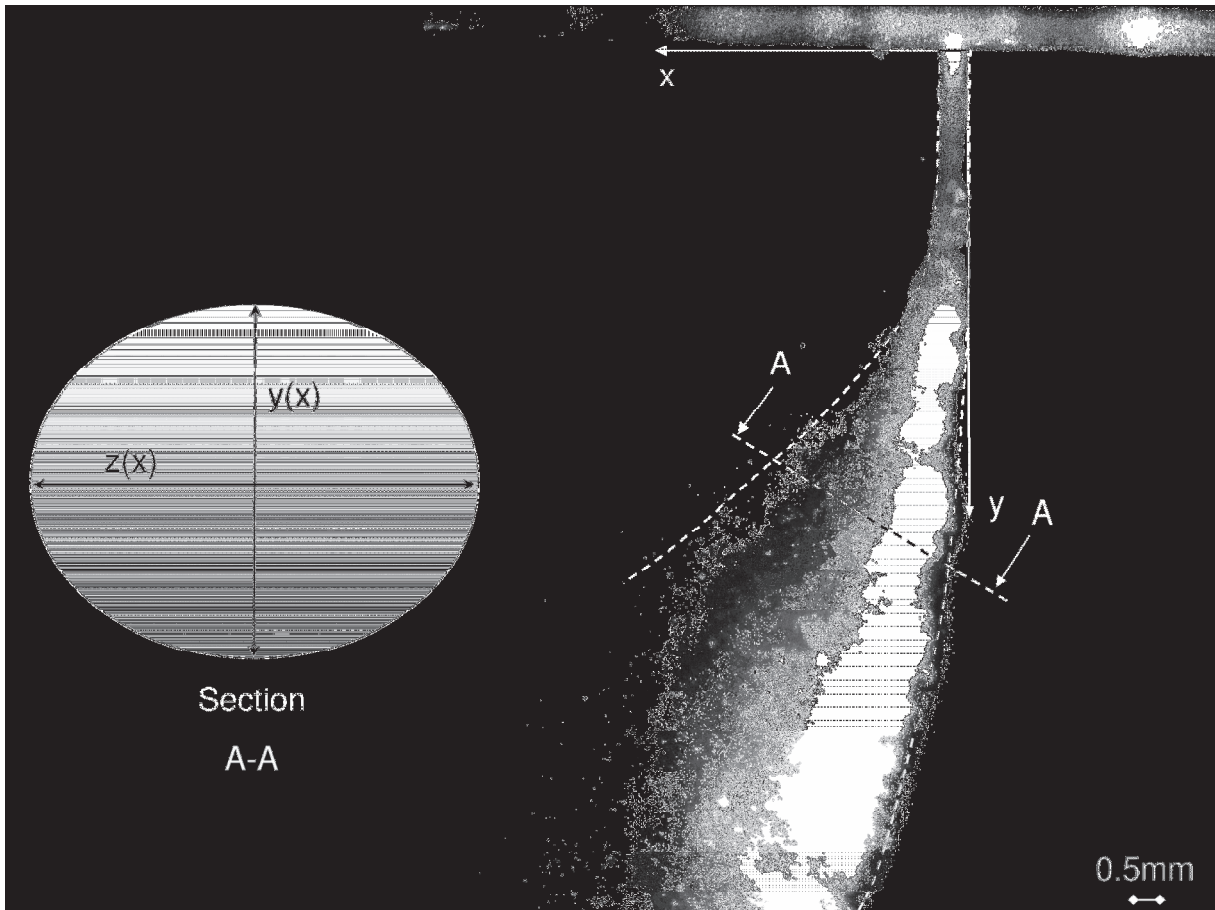


Figure 3.20 – Overall spray structure

The format of the fitting function (3.1.1) is taken from work of Wu et al. [61], who investigated turbulent jets injected ( $q$  range of 4 to 185) into a cross-flow (Mach number 0.2 to 0.4) and found the constants to be 1.37 and 0.5 respectively, with a good fit to their experimental data.

In the current work however, the empirical constants found by Wu et al. are not applicable, since much higher momentum ratios are employed. Nonetheless, the general shape of the function provides a very good representation of the spray trajectory, providing the right constants are found. The constants were found performing a non-linear regression analysis using equation (3.1.1) as a model and the coordinates gleaned from the image data. Both the windward and leeward spray lines (as shown in Figure 3.20) were fitted.

Once the extent of the spray spread in the  $x$ - $y$  plane was determined, the spray dimensions in the  $x$ - $z$  plane also have to be found. Lacking any optical access to this plane, a fully empirical model was employed. Fortunately, the spray dimensions in this plane were found to be only dependent on the momentum ratio by many workers and hence a fairly good result can be expected from such a purely empirical model [62-64].

In addition a paper by Oda et al. [63] investigated JICF configurations, very similar to the ones in this work and found the following fitting function for the spray half width in the  $x$ - $z$  plane:

$$z(x) = Aq^B \ln\left(1 + C \frac{x}{d_0}\right) d_0 \quad (3.1.3)$$

Where  $A = 1.83$ ,  $B = 0.17$  and  $C = 2.8$  [63].

Now that both the maximum dimensions in the x-y and x-z plane can be identified, the volume occupied by the spray can be calculated by assuming a geometry similar to the one shown in Figure 3.20.

Although surface disturbances along the injected jet start very shortly after the outlet and can produce a very fine spray of initial droplets only the ellipsoidal head of the spray was considered. The reasoning for choosing only the ellipsoidal head is shown in Figure 3.21. Most of the spray is contained within the JICF vortex structure and since the mixture resulting from the initial surface disturbances is extremely lean here (locally), it can be neglected.

Finally, by calculating the air volume occupying the same volume as the spray, the mixture ratio can be estimated.

One should always keep in mind that the above procedure only gives a rough estimate of the global overall mixture ratio and that the local mixture ratio can still vary significantly. Nonetheless this estimate gives a benchmark against which other experimental data can be compared.

The reason for these local differences is the very complex vortex structure of a JICF, which is shown in Figure 3.21 and was proposed by Lim et al. in 2001 [65].

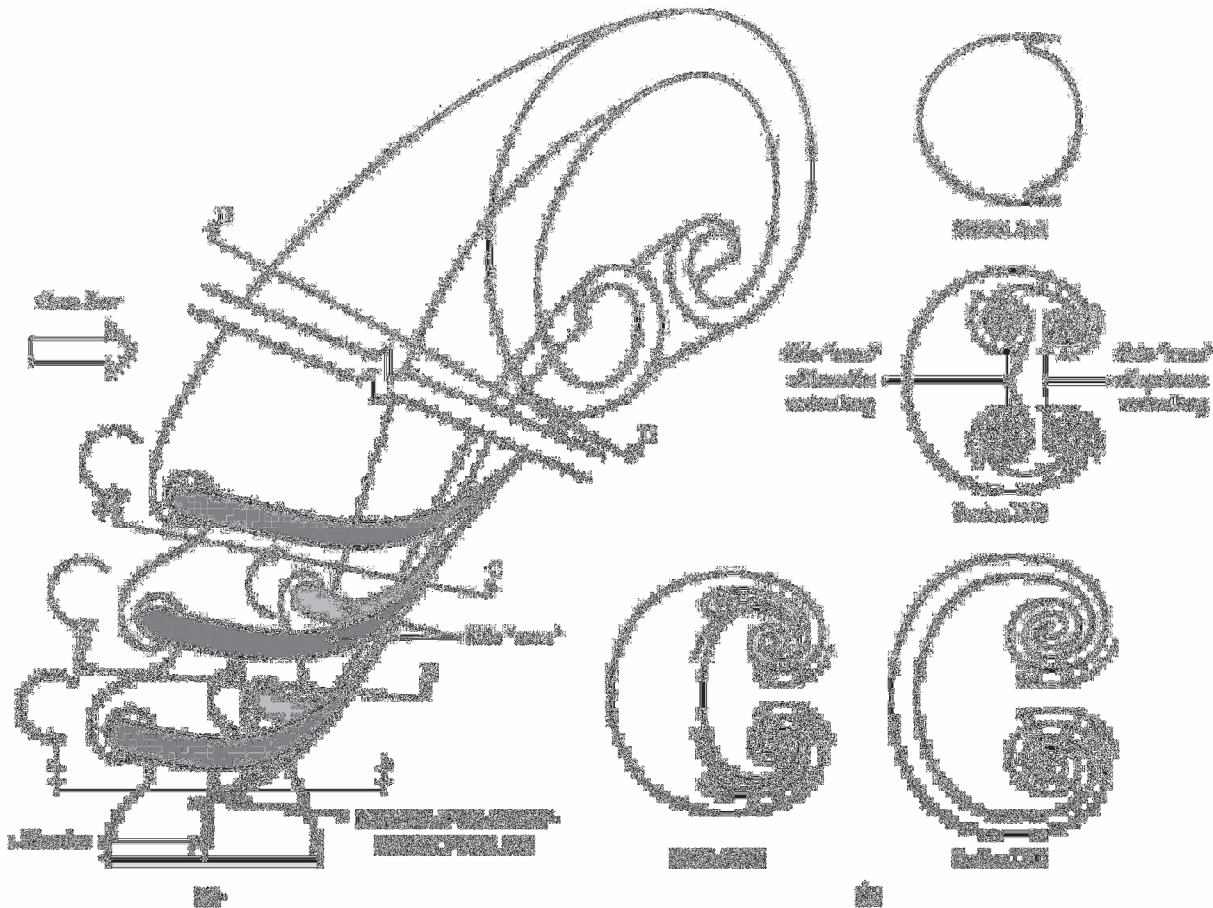


**Figure 3.21** – Vortex structure proposed by Lim et al. [65] (b) shows cross sections of (a) at various locations

Lim et al. arrived at this structure by investigating a tinted water jet entering a water cross-flow.

In the case of a two-phase system, where a liquid jet is injected into a gaseous cross-flow, the overall structure will be similar with the additional interaction of the liquid jet and

evaporating particles with the overall structure of the gaseous flow. The general “kidney” shape of the jet in the far field was also confirmed by other workers [66, 67]. It originates from the two counter-rotating vortices generated early on by the passage of the cross-flow around the jet [65].

These two vortices will most likely cause a local increase in fuel concentration, as many droplets (and fuel vapour) will be caught by these vortex structures and be carried inward, creating two localized strands of fuel rich gas.

As mentioned this local fuel concentration cannot be estimated and only direct measurements could give reliable results on the local lambda distribution. Nonetheless, the overall estimate of lambda and the knowledge in the general structure, explained in this section, will be invaluable for the subsequent analysis of the results.

### **3.7 Experimental Error**

As is the case with any experiment there are many sources of error, which have to be understood and if possible remedied. These sources of error can be of various sources, such as:

- Calibration errors in the sensors
- Electric/electronic interference (for example 50Hz mains interference)
- Design errors in the experimental apparatus
- Operator errors
- Analysis errors (or the compounding of any of the above errors, through the mathematical manipulations necessary for analysis)

In order to avoid these errors many measures have been taken. First of all, all sensors of the HWK were calibrated against highly precise known data. Secondly, the signals of the sensors are automatically searched for obvious electronic interference. In addition as was explained in section 3.5, several redundant timing signals are used to make sure the experimental data can be precisely time – calibrated, one of which is the deliberate flashing of the LED illuminating the injection, prior to each injection, to synchronise the camera and sensor timelines.

The cameras and sensors used for the detection of injection and ignition are also of vital importance. While the ignition was always detected with photodiodes of 0.1ms accuracy, initially, a slow DALSA camera was used to detect injection. This camera had a frame rate of only 200fps, which is sufficient for general observation, but leads to an accuracy of  $\pm 2.55$ ms when determining the moment of injection. With expected ignition times only a few milliseconds to several tens of milliseconds, this was found to be unacceptably imprecise and the camera was replaced, with the high speed camera mentioned in section 3.4. This camera boasts a frame rate of 8000fps and hence with the combined accuracy of the photodiode this leads to a maximum error of  $\pm 0.1125$ ms in the determination of the induction time. This system was later further improved to incorporate a single photodiode for injection detection, decreasing the error further to  $\pm 0.1$ ms.

To guard against operator errors, the analysis software as well as the HWK operational software require precise documentation of all settings. Hence an erroneous setting in the experiment will automatically be documented and if not discovered immediately, will be found during later data analysis. The analysis software itself was tested against dummy datasets, with known configurations and results (which were pre-calculated by hand) in order to eliminate programming errors.

In order to identify the design errors (or operational peculiarities) of the HWK, the three main flow characteristics were tested against theoretical calculations. These three factors are pressure, temperature and flow velocity.

The pressure prior to opening of the main valve is the only operational parameter that can be directly set by the operator of the experiment. The ensuing actual experiment pressure after the opening of the main valve is entirely governed by the established wave system. This wave system in turn is influenced by the geometry and opening mode of the main valve and nozzle. A comparison between the theoretically predicted pressure values (see section 2.1.7) and the experimental values can be seen in Figure 3.22 and it shows a very precise match. Various experiments were conducted at pressures ranging from only 2.5bar to 22bar and the variation between the expected and the measured value is very small. This information was then integrated into the operational software of the HWK, so that the operator could set the initial pressure to the appropriate level, allowing a precise control of the pressure during the experiment.

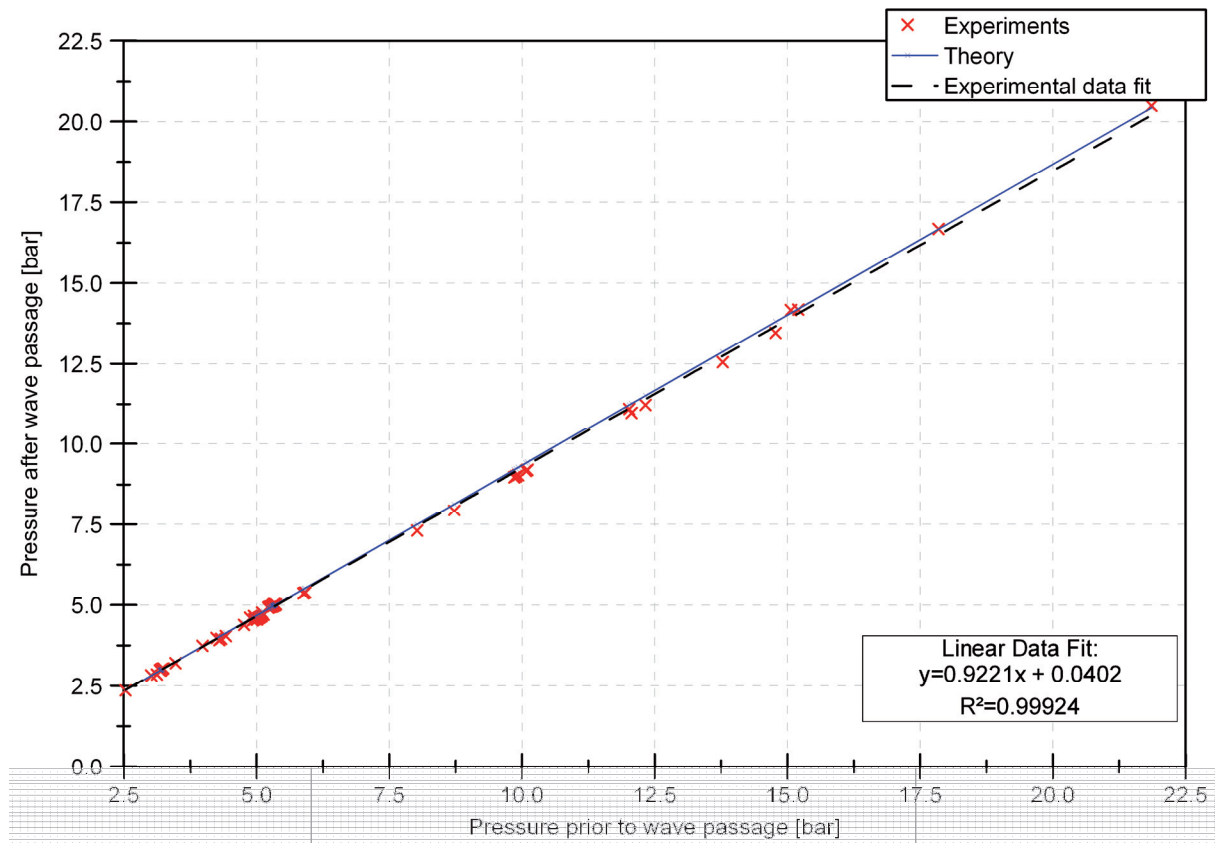


Figure 3.22 – HWK pressure, experiments vs. theory

An identical analysis was also performed for the temperature behaviour of the HWK during the experiment, the results of which can be seen in Figure 3.23.

The temperature characteristics of the HWK are somewhat more complex than the pressure behaviour. While the pressure is the same throughout the HWK, this is not the case with temperature.

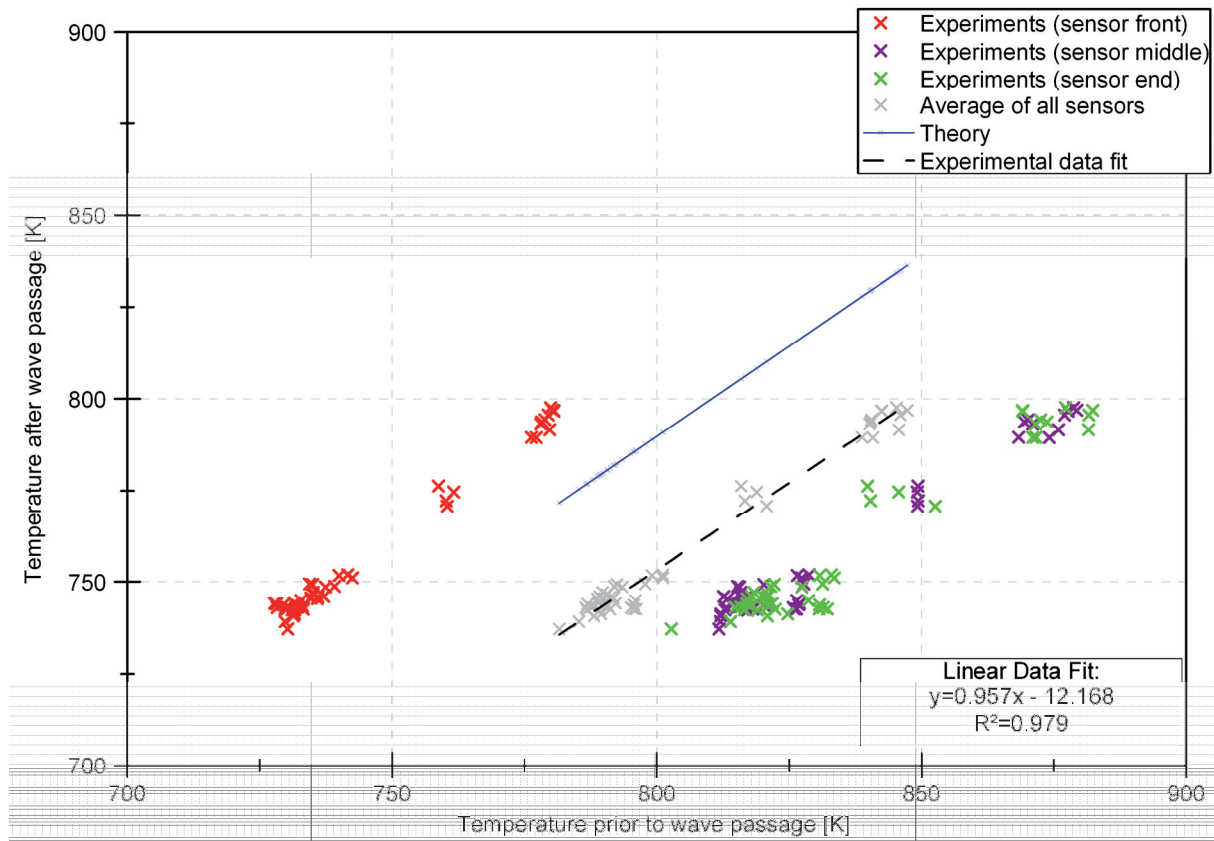


Figure 3.23 – HWK temperature, experiments vs. theory

The three sensors shown here are placed at the front, middle and end of the heated driver section. As can be seen the sensor at the front of the driver section (near the thermal barrier valve) registers a significantly lower temperature prior to the experiment than the remaining two sensors. This is due to the thermal management steps taken to avoid an overheating of the test section (see section 3.2.2). This then leads to a lower average temperature in the driver section.

Applying the theory of section 2.1.7 to the average temperature leads to the results shown in Figure 3.23. It is clear that the theory over-predicts the temperature to be expected during the experiment. Fortunately, the overall behaviour can still be approximated fairly well by a linear regression analysis. As before this information was then also incorporated into the HWK control software allowing a fairly good estimation of the temperature to be expected during each experiment.

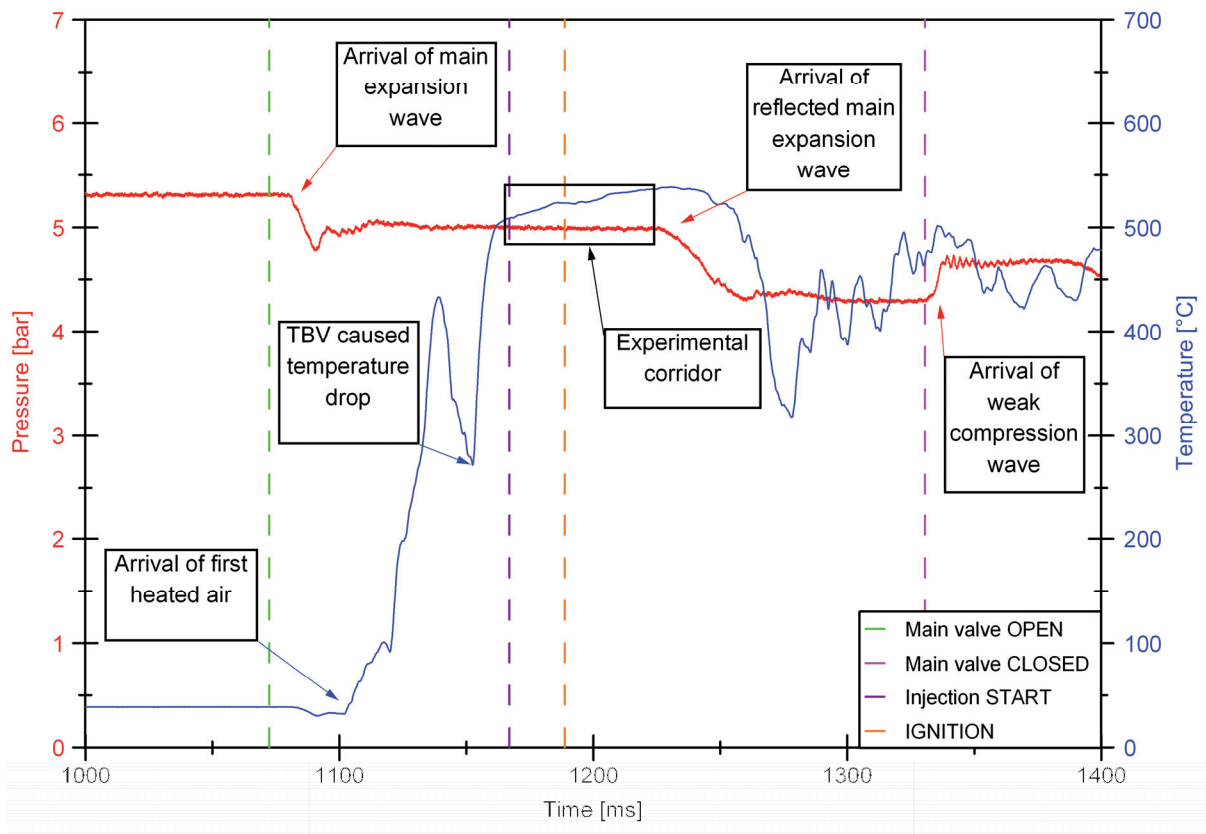


Figure 3.24 – HWK detailed transient behaviour

However, since there is a temperature gradient present, it is worthwhile to examine the thermal behaviour further, in particular the transient behaviour during an experiment. One such example can be seen in Figure 3.24. The events follow the timeline described in section 3.5 and the data shown here originates from sensors located near the injection point.

It was evident from Figure 3.22 that the pressure of the HWK behaves as expected by the theory. This is confirmed in this figure. Shortly after the opening of the main valve the pressure at the sensor location drops to a new level established by the wave system. This pressure then remains constant until the return of the expansion wave to the sensor location at about 1225ms. The expansion wave has fanned out as expected (see section 2.1.5), which is evident by the reduced slope of the pressure drop. After the wave passage a second lower pressure level is established, which is increased again shortly after the closing of the main valve. This increase is caused by suddenly bringing the flow to rest due to the main valve closure and a subsequent weak compression wave that is formed.

The temperature behaviour on the other hand is rather more complex. Initially, the temperature in the test section is about 40°C. The flow induced behind the expansion wave then moves the heated air from the driver section into the test section and the temperature rises sharply. However, since the flow behind the wave only has a velocity of about 25m/s, this rise happens with significant time delay. The temperature then drops again significantly, which was an unexpected behaviour, the cause of which was found to be the TBV.

Stagnant air in the cavities of the valves is initially at the same pressure (but lower temperature) than the rest of the heated driver section. With the arrival of the expansion wave, the pressure in the tunnel is suddenly reduced and the stagnant air in the cavities of the thermal barrier valve is at the higher original pressure level. This then causes this cooler air from the cavities to be jetted into the wind tunnel through the gaps in the thermal barrier valve. This equalizing of the cavities in the thermal barrier valve is responsible for the

temperature drop, before the temperature can rise again to reach the predetermined final experimental value.

From about 1165ms to 1225ms both temperature and pressure are at stable levels (pressure more so than temperature) and this is the corridor within which an experiment can be conducted.

For completeness the injection of the fuel and the ignition instant are also marked in this figure. In order to make sure that the spray is always injected at the right experimental window, only experiments were used for the discussion in the next section, which conformed to the following minimum standards for the spray history variation:

- Pressure fluctuation (peak-peak) max. 0.1bar (equivalent error depending on pressure is between 1% and 3%)
- Temperature fluctuations (peak-peak) max. 25K (equivalent error depending on temperature is between 3.1% to 4.2%)
- Velocity fluctuations (peak-peak) max. 0.75m/s (equivalent error depending on velocity is between 2.3% to 4.7%)

With the above standards a single experiment is within an acceptable tolerance limit to be used for further analysis. However, the question remains whether or not experiments are also comparable amongst each other. While the peak to peak error of two different experiments might be within the above limits, the temperature distribution between the two experiments might be completely different. In order to make sure this is not the case, several experiments were compared. The result of such a comparison of the spray histories of four individual experiments can be seen in Figure 3.25.

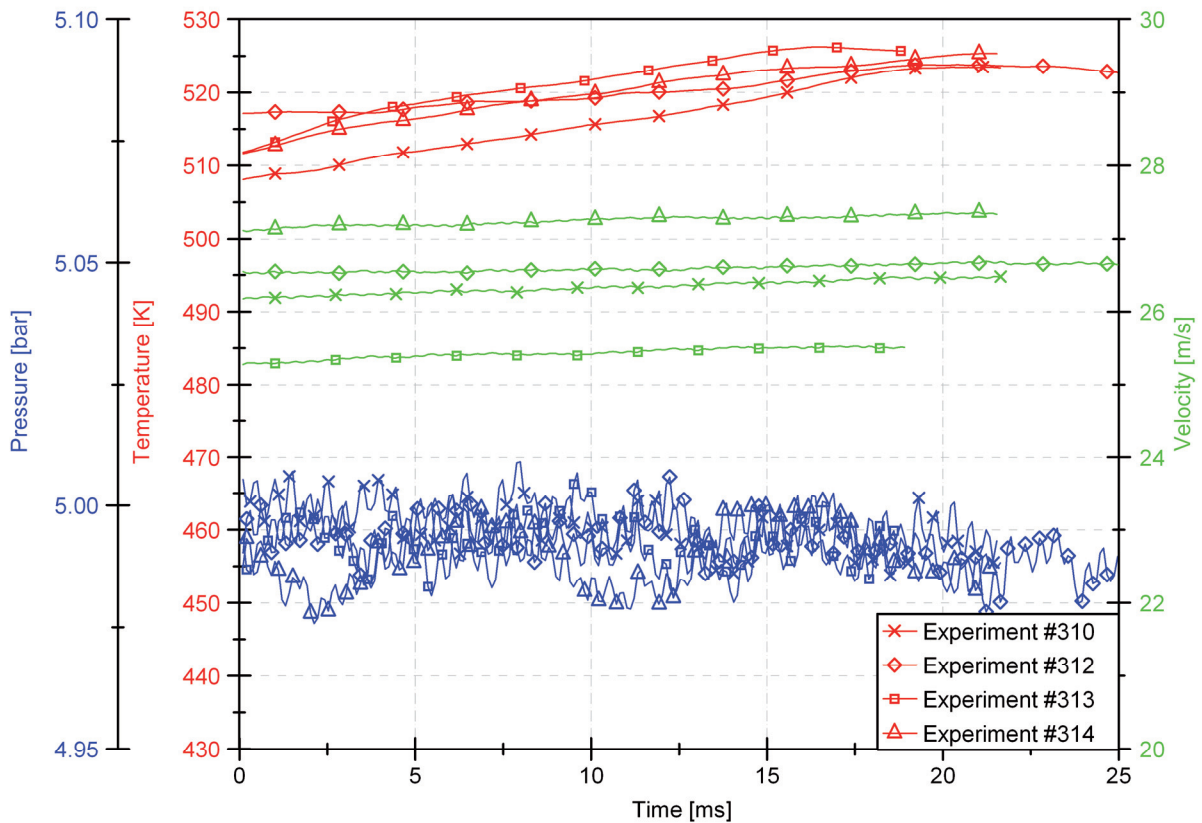


Figure 3.25 – Comparison of the spray histories of several experiments

The figure shows, that the pressure of the experiments remains within a very tight corridor, hence giving very good comparability between experiments. Temperature is also still within acceptable limits, but as could be expected from the results of Figure 3.23, there is a slight variation between experiments. The overall characteristics of each experiment however are comparable (no unexpected peaks or pokes) and hence a good compatibility between each experiment is ensured. The flow velocity also has the same characteristics for each experiment. This is expected since the flow velocity is a derived entity from, dynamic and static pressure as well as temperature (density). This also means that the fluctuations in temperature reappear in these graphs. Nonetheless the flow velocity is within acceptable limits and hence a good comparison is possible.

With the above comparison it is clear, that the experiments can be compared if the mentioned quality parameters are adhered to. As a consequence all results discussed in the following section are within these parameters. As there were numerous small modifications on the HWK during the course of this work, the variations displayed in the diagrams of the next section are calculated individually for each experiment.

## 4 Results and Discussion

Now that the overall problem setting, the theoretical background and the experimental setup have been discussed, this section will present the results of the experiments.

The previous sections showed that there are a vast number of variables, whose effect on autoignition can be investigated. These are (among many others) temperature, pressure, flow velocity, type of gas, type of dispersed phase or fuel, initial temperature of the fuel, injection pressure, injection orifice dimensions and injector assembly dimensions. It was decided to narrow down the variables by leaving some parameters untouched throughout the experimental campaigns, which lead to the following parameter space in which all the experiments of this work were conducted:

- Pressure: 3.5 – 8bar
- Temperature: 625 – 950K
- Gas in the HWK: Air
- Flow velocity: 26m/s
- Fuel: n-heptane (0.5ml per experiment)
- Fuel temperature: 275 – 315K
- Injection: Jet in cross-flow (JICF) through a 0.5mm plain orifice nozzle in the middle of the test section
- Injection pressure differential: 2MPa with respect to the pressure of the flow, leading to an estimated SMD of about 43 $\mu$ m (estimated using experimental data and the experimental relation by Elkotb et al. [55] shown in section 2.2.4)

Even with this limited set of parameters over 1100 experiments were conducted for this study, in order to obtain enough data for analysis. Another reason for the large number of experiments, are the stringent requirements set in the previous section, which reduce the above number of experiments that fall into this category significantly.

On the numerical side over 4300 single droplet ignition experiments were performed for this study. This large number of numerical experiments allowed the creation of a large look-up table that encompasses the entire experimental domain shown above.

This section will first detail the experimental observations, both in a quantitative (induction time) and qualitative way (video footage). Secondly, the numerical results and the methods used to construct the look-up table will be highlighted.

The numerical and experimental results will then be compared and a hypothesis with respect to spray autoignition will be presented and discussed.

## 4.1 Experimental Results

### 4.1.1 General Overview

The first step in the discussion of the experimental results is the comparison of the current experiments with results obtained in previous studies. Many previous studies have been conducted on the autoignition of different types of fuel with the aim of characterising their autoignition behaviour, amongst others by Spadaccini et al. [7, 17, 18, 25], Wolff et al. [23] and Hinkeldey et al. [22]. Since these studies were mostly geared towards finding the autoignition behaviour for these fuels with respect to the Arrhenius equation, so that this relationship could be used in further mechanical designs, mostly real fuel compounds were investigated. The results of these studies were shown in Figure 1.6 and are reproduced here (in a slightly different notation) for convenience (see Figure 4.1). In addition a new study by Wolff et al. also examined the autoignition behaviour of n-heptane and the results of this investigation are also shown in the figure below. The investigation was carried out at 0.8MPa only and hence the data is represented as a line. In general all studies below, which are represented as an area, were conducted at ranges of pressures, while data represented by lines indicates studies conducted at a single pressure level.

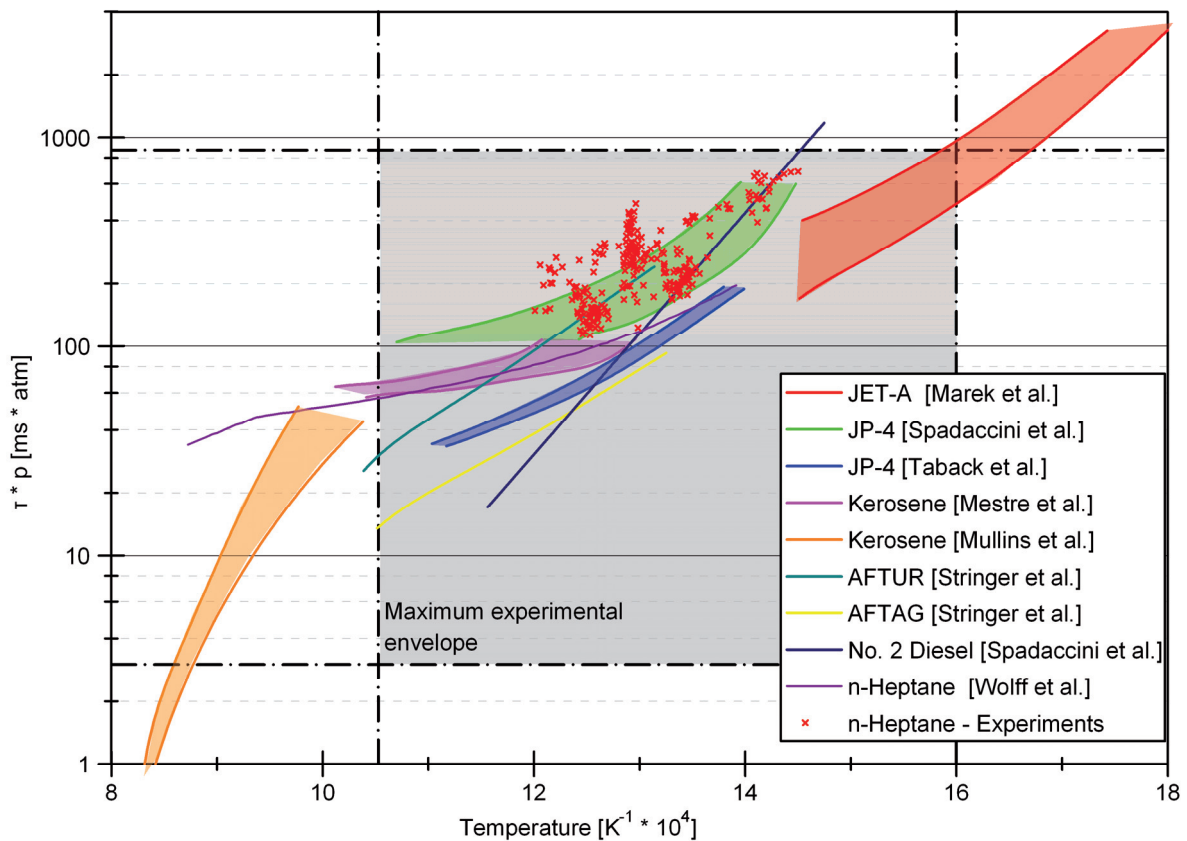


Figure 4.1 – Comparison of the experimental results with other studies

The results of this work and the maximum experimental envelope defined in the introduction were added to Figure 4.1. In contrast to most of the previous studies, pure n-heptane was investigated as opposed to an actual fuel. The reason for this is the complexity of normal fuel compounds such as for example kerosene derived JP-4, which consists of more than 74 different components [68]. It is obvious that such a compound is far too complex for detailed computational analysis (which is required if the final goal of a complete spray simulation is to

be realised), as detailed chemical kinetics would supersede the capabilities of all but the most powerful supercomputers (were such kinetics available in the first place).

Additionally Figure 4.1 shows that the intended function of the HWK, as an experimental facility capable of simulating any other flow device, was achieved. The experiments of Spadaccini, Wolff and all previous researchers in this field have always been done in a continuous flow device [17, 21-23], similar to the one shown in Figure 4.2. The HWK on the other hand functions as a Ludwieg-tube. In the preceding experiments the fuel was always injected in a co-flow direction and allowed to mix and evaporate, while the JICF injection of the HWK is more akin to the injection used in modern gas turbines.

A detailed comparison of the only two n-heptane experiments (this study and Wolff et al.) is shown in Figure 4.3.

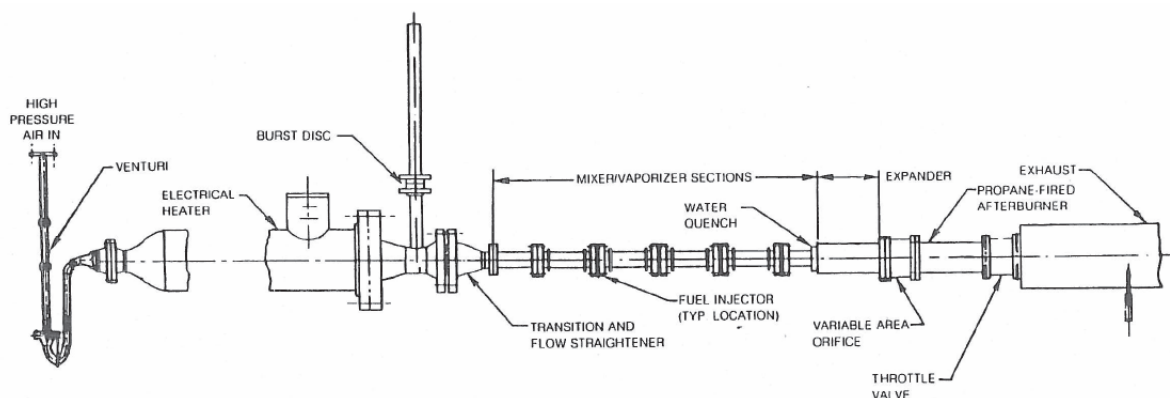


**Figure 4.2** – Schematic of the apparatus used by Spadaccini et al. [7]

The discrepancy in the data can be due to many factors. The most likely candidate however is the injection system used and its corresponding injection pressure. Wolff et al. used a lower injection pressure and a co-flow injection, leading to lower atomisation [23]. This in turn leads to larger droplets, which remain in the hot ambience for longer. In general a lean inhomogeneous mixture tends to have shorter induction times than a lean homogeneous one. The effect of injection pressure on induction time is analysed in detail in section 4.1.3.

Also interesting is the fact that the Wolff et al. data corresponds roughly to lowest limit of the data of the current investigation. This is an expected result as the induction time in the investigation by Wolff et al. was determined from the flow velocity and the position of the flame front. Consequently once the flame is established in a position in the continuous flow the earliest possible ignition delay will be determined. The HWK experiments on the other hand establish a new flow for each data point and consequently the variations in induction time due to inhomogeneties are clearly visible.

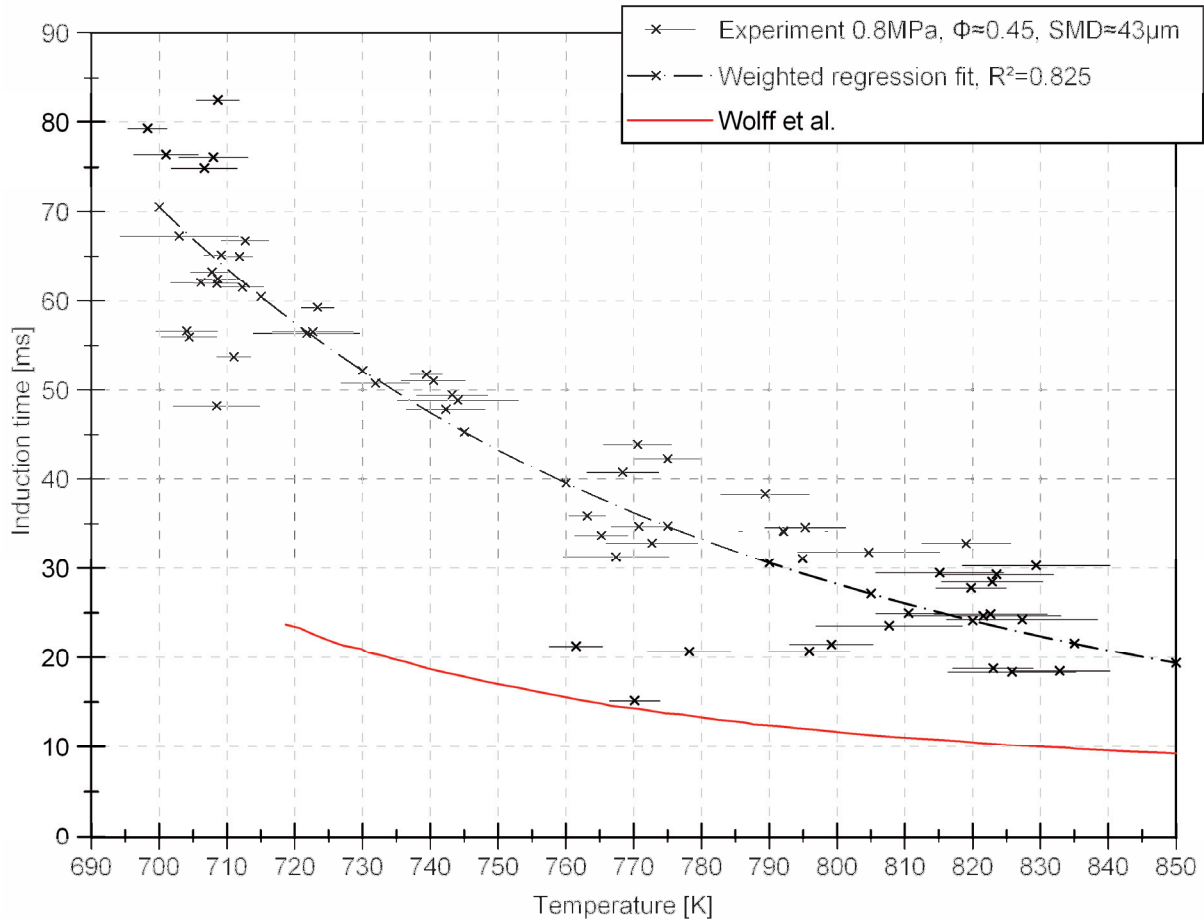


Figure 4.3 – Comparison of current data and Wolff et al.

On the other hand Figure 4.1, which is the standard notation for spray autoignition, only exhibits a broad overview of the results. This representation is sufficient for a first comparison between many different studies, but as the regions (and seldom lines) in the diagram indicate, a large amount of detailed information is lost in this type of representation. For example it is not possible to discern the effect of temperature or pressure alone on the induction time. As a consequence it is necessary to investigate the results in far more detail, which will be done in the subsequent sections.

#### 4.1.2 Effect of fuel temperature on autoignition

Since both ambient pressure and temperature were shown to have a significant effect on induction time by various studies (both single droplet and spray) [5, 7, 29-32, 58], the detailed investigation of these two parameters was delayed until the effect of fuel temperature on induction time was investigated, where information was much less clear.

It was unknown just how much effect a change of fuel temperature of roughly 35K would have on the induction time of a spray. Single droplet experiments suggested that the effect was not insignificant, but this result might be misleading as the drops in these experiments are rather large compared to technical sprays. Another factor supporting the hypothesis that the effect could be small is the enthalpy of vaporisation required. Figure 4.4 shows the enthalpy of formation required for n-heptane for a wide temperature range. Clearly the change in required enthalpy in the applicable temperature range from 380K to 315K is fairly small. A small fuel temperature effect has the possible advantage of reducing the parameter-set defined in section 4 significantly.

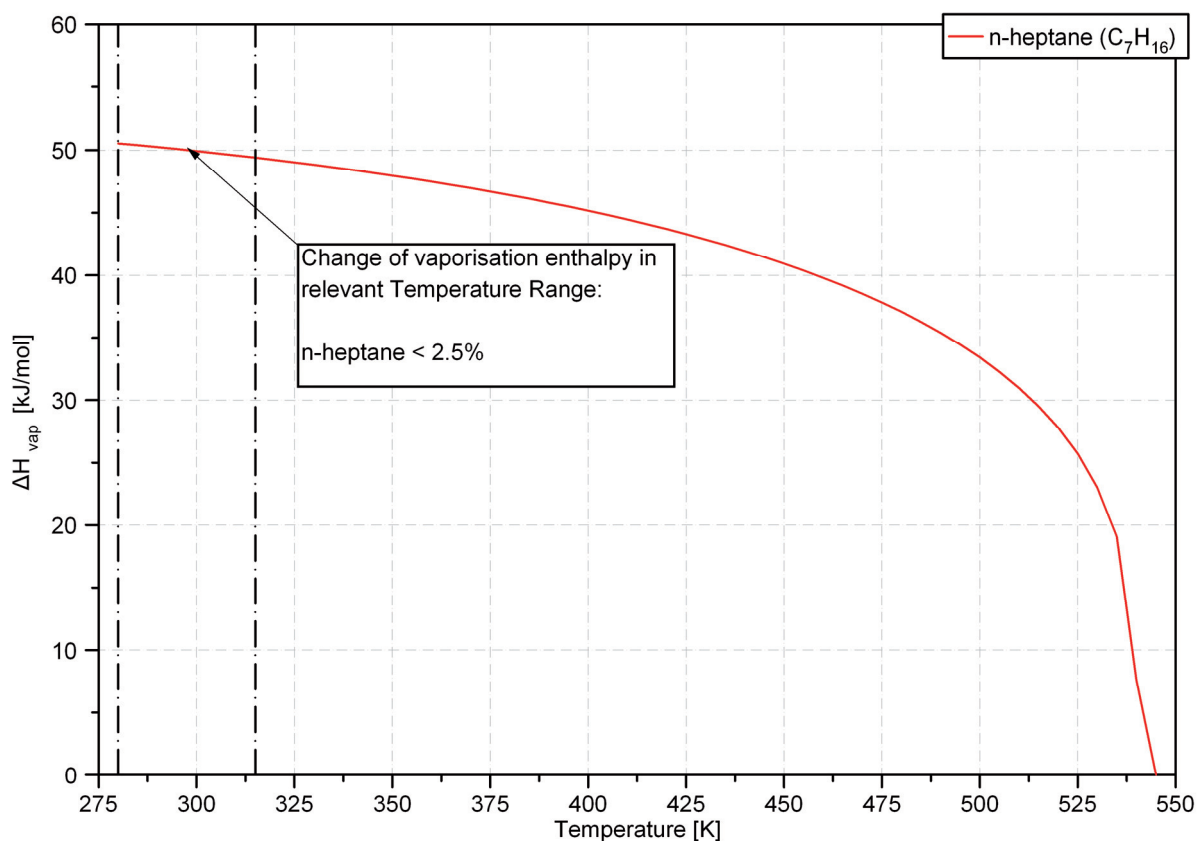


Figure 4.4 – n-heptane enthalpy of vaporisation [69]

The results of the experiments are shown in Figure 4.5 and seem to confirm the above hypothesis. The effect of fuel temperature on the induction time is minimal and no real trend can be discerned. While the last three sets of data seem to suggest a slight reduction in the induction time (as would be expected from the above analysis), the first set of experiments with a fuel temperature of 280K exhibits behaviour contrary to this trend. Also, the results for each individual temperature set vary by a large amount (up to 10ms, or  $\pm 12.5\%$ ). This variation will be discussed in more detail in the following sections, for now it is sufficient to say that it originates from the turbulent nature of the spray ignition process. This further complicates the detection of any trend in the data and hence none is included in the data of Figure 4.5.

As a consequence of these results further experiments were all conducted at the same fuel temperature of 280K. This ensures that the experiments remain comparable, since the effect of fuel temperature (in this limited fuel temperature range) is unclear.

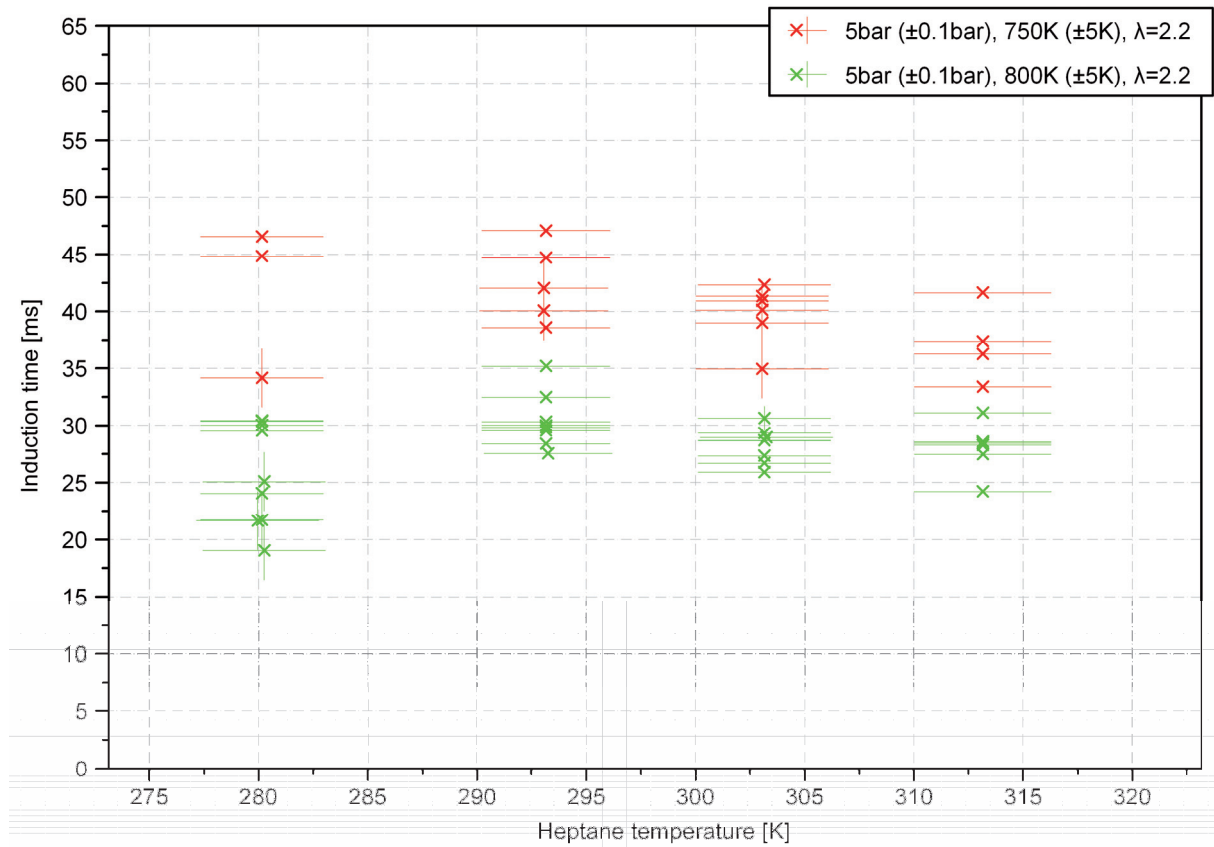


Figure 4.5 – Effect of the variation of fuel temperature on spray autoignition

### 4.1.3 Effect of injection pressure on autoignition

Although the injection pressure differential was chosen to stay constant for this study to limit the amount of experimental data. The reasoning behind this decision will become apparent in this section. The effect of varying injection pressure was nonetheless investigated in a single case so that the importance of this parameter with respect to the remaining experiments could be determined. To accomplish this, the injection pressure differential was varied from 0.1MPa to 2.5MPa above the tube pressure. The results of this variation can be seen in Figure 4.6.

As can be seen the injection pressure differential does not only have a marked effect on the spray structure, but also on the induction time. With increasing injection pressure the spray becomes much finer and the spray penetration increases, which is consistent with spray formation hypotheses from plain orifice injectors [34]. This leads to a reduced overall equivalence ratio, since more volume of air is occupied by the spray.

The effect seen in Figure 4.6 is hence a combined effect of reduced droplet size and increased equivalence ratio. Smaller droplets tend to evaporate more quickly and the remaining single phase mixture tends to have a longer induction time (see section 4.2.2), than a gas-liquid mixture (since rich regions are not present any longer). In addition to this a lean mixture has a longer induction time than a rich one. Since this combined effect cannot easily be separated without further information, it was decided to keep injection pressure constant throughout the rest of this investigation.

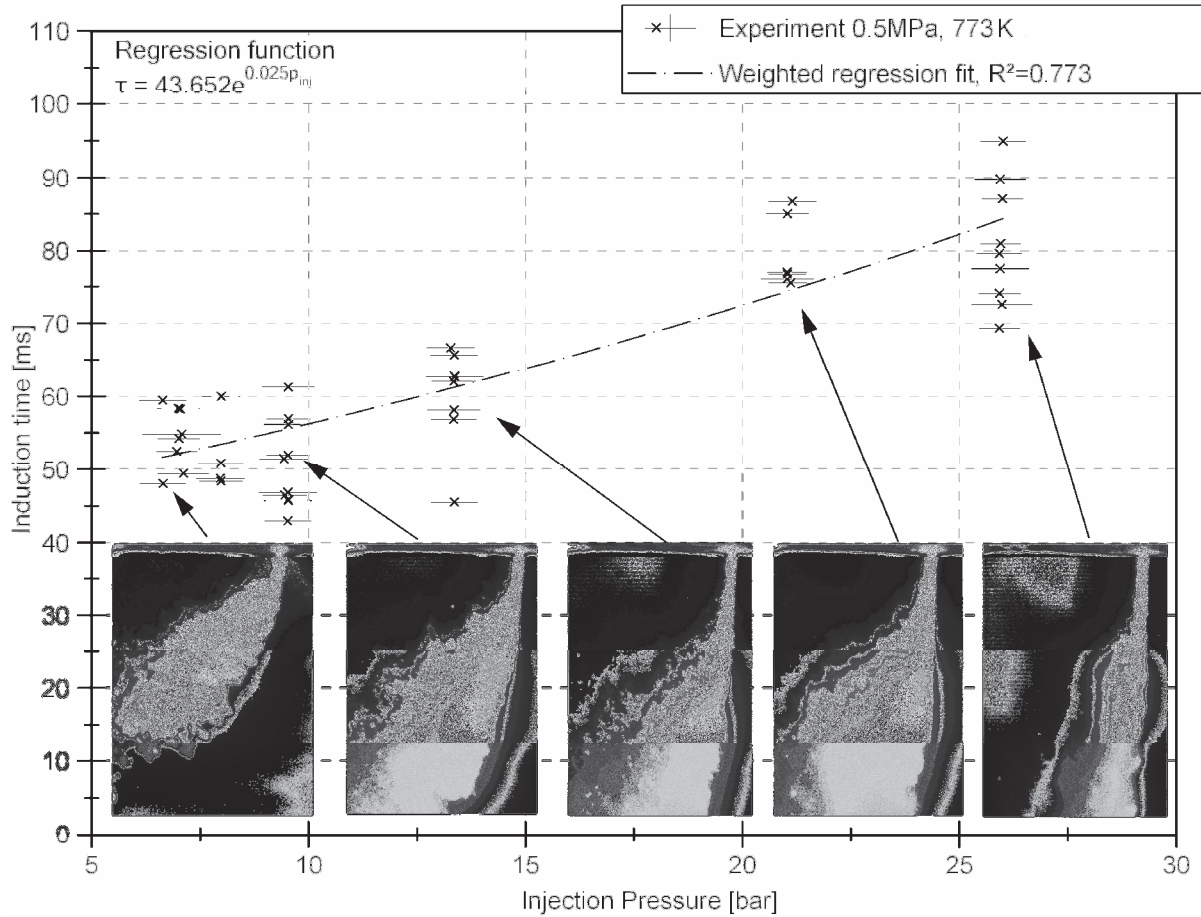


Figure 4.6 – Effect of varying injection pressure on autoignition

#### 4.1.4 Effect of pressure on autoignition

The effect of pressure on the autoignition times is shown in Figure 4.7. This figure shows both the experimental data points (each adhering to the quality requirements mentioned in section 3.7) and an Arrhenius type curve fit to the corresponding data.

For this work the following expanded version of the Arrhenius equation is utilized:

$$\tau_{ign} = A\phi^m p^n e^{\frac{E}{T}} \quad (4.1.1)$$

Where  $A$ ,  $m$ ,  $n$  and  $E$  are empirical values to be determined. While  $E$  is in essence the apparent global activation energy of the fuel in question, unfortunately no reliable data for the global activation energy of n-heptane exists and it must be determined for each experiment. Also the pressure is often quoted in bar and not Pascal, which will also be the convention in this thesis.

The fitting function is constructed using a least-squares nonlinear regression for arbitrary fit functions, employing a modified version of the Levenberg-Marquardt algorithm. In addition a weighting scheme is employed, where the experimental values with higher measurement uncertainty only contribute accordingly to the graph. This additional weighting was necessary since the spray detection system was upgraded during the experimental campaign (see section 3.6), yielding different measurement errors. The results of the data-fit are also displayed in Figure 4.7.

In general the effect of increased pressure is to reduce the induction time. This is due to the combined effects of increased chemical activity and increased thermal characteristics of the surrounding gas (such as higher thermal conductivity for example). The effect seems to be proportional to  $1/p^{1.71}$  or  $n = -1.71$  on average, while it increases towards higher temperatures, almost approaching a value of -2. This is consistent with data from previous studies such as Spadaccini et al. who also reported a value of  $n = -2$  [7, 17, 18].

Interestingly, the experiments conducted at 758K exhibit a longer induction time than the experiments conducted at 748K. While, this behaviour could be expected in single droplet experiments where regions of NTC (negative temperature coefficient) were reported [5], it is not expected in complete spray experiments. The NTC effect was expected to be of too low intensity to be visible in a polydisperse spray. The effect seen here however, is not yet strong enough to justify the postulation of NTC effects in spray autoignition for two main reasons: first, there are too few data points available for the graph of the 758K experiment (especially in the high pressure range) and secondly, this effect was not observed in any of the previous studies.

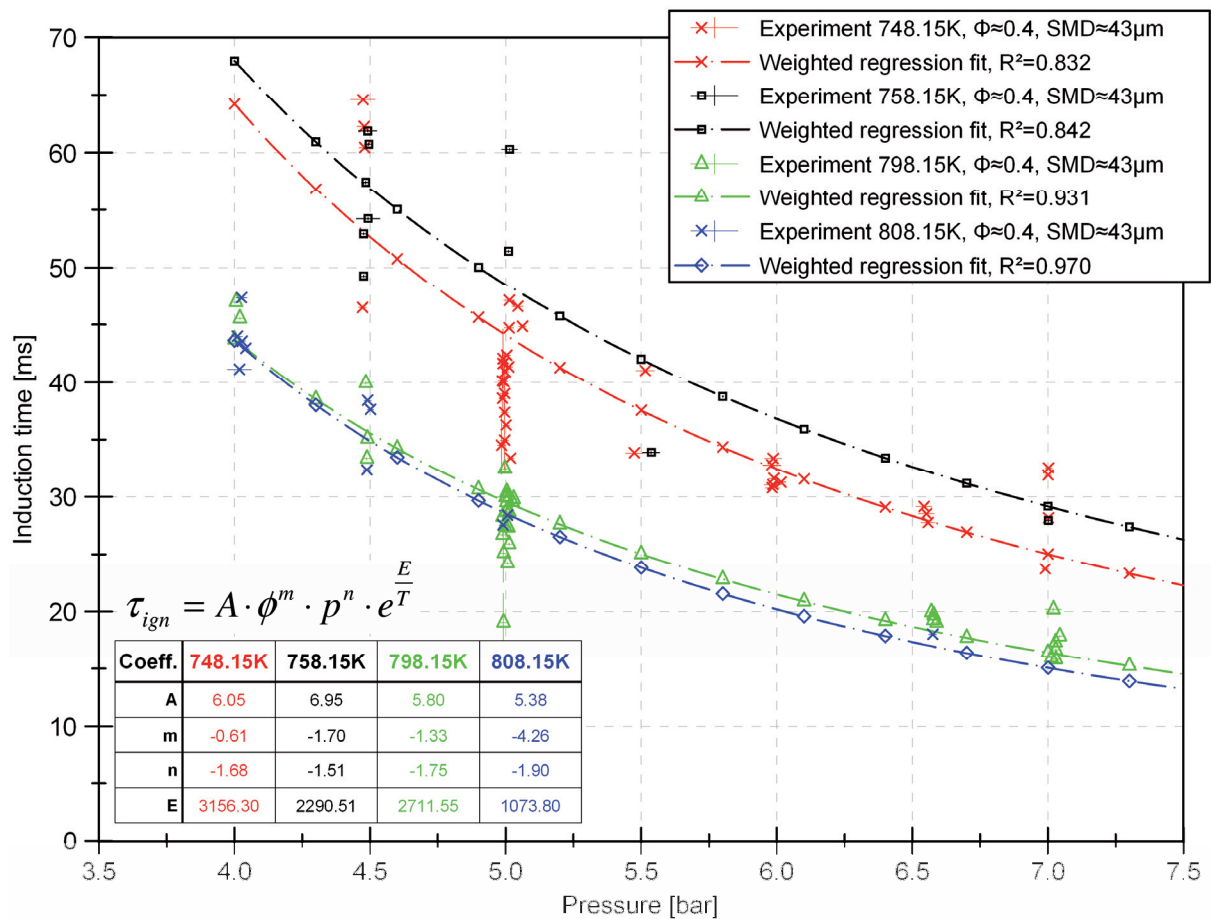


Figure 4.7 – Effect of pressure on autoignition behaviour

The scatter seen in the data of Figure 4.7 is very low in the pressure wise direction, while it is quite high in the induction time direction. The low scatter in pressure is due to the good controllability of pressure in the HWK and the high quality standards set in section 3.7.

The high scatter in the induction time between different experiments on the other hand is probably due to a combination of effects. Some scatter comes from experimental error, but the vast majority of the scatter is due to the polydisperse and turbulent nature of the spray and is intrinsic to spray autoignition. Even though turbulence and spray droplet distribution are essentially random in nature, they can nonetheless be described in overall concepts such as

turbulence intensity and spray droplet distribution. The following sections will describe how these factors (in particular spray droplet distribution) may have an effect on the spray autoignition process. To this end the effect of temperature on autoignition is investigated in the subsequent section and the data is then correlated and compared with respect to both temperature and pressure.

#### **4.1.5 Effect of temperature on autoignition**

The effect of temperature on the autoignition of a n-heptane spray is shown in Figure 4.8. Similar to the previous section the data is fitted against equation (4.1.1), with the same regression procedure. The results of this analysis and the corresponding coefficients are also shown in the figure.

The trend shown in Figure 4.8 clearly shows an exponential decrease of induction time with temperature. The suspected NTC regions from the previous section can not be confirmed. The exponential decrease of induction time with pressure can also be observed in Figure 4.8 implicitly. In the low pressure and temperature range a large reduction in induction time can be achieved, with a relatively minor change in pressure (0.05MPa). As the pressure increases this effect decreases in intensity, so that the same increase of pressure causes only about one fourth the decrease in induction time that was achieved in lower pressure regions.

As in the previous example, there is some scatter in the results due to the multidimensional nature of the problem and some experimental uncertainty. Again the data used for this analysis adheres to the quality requirements mentioned before and hence the uncertainty in terms of temperature is less than 4.2% (even though the displayed deviations look quite imposing). This supports the hypothesis that most of the scatter, results not from poor experimental data, but from the interaction of the spray droplet distribution and turbulent flow. More evidence for this phenomenon is the fact that the scatter is noticeably larger near the low temperature range. Indicating that the local minute differences caused by turbulence and polydispersity have a pronounced effect here, while the importance of these inhomogenities diminishes with rising temperature.

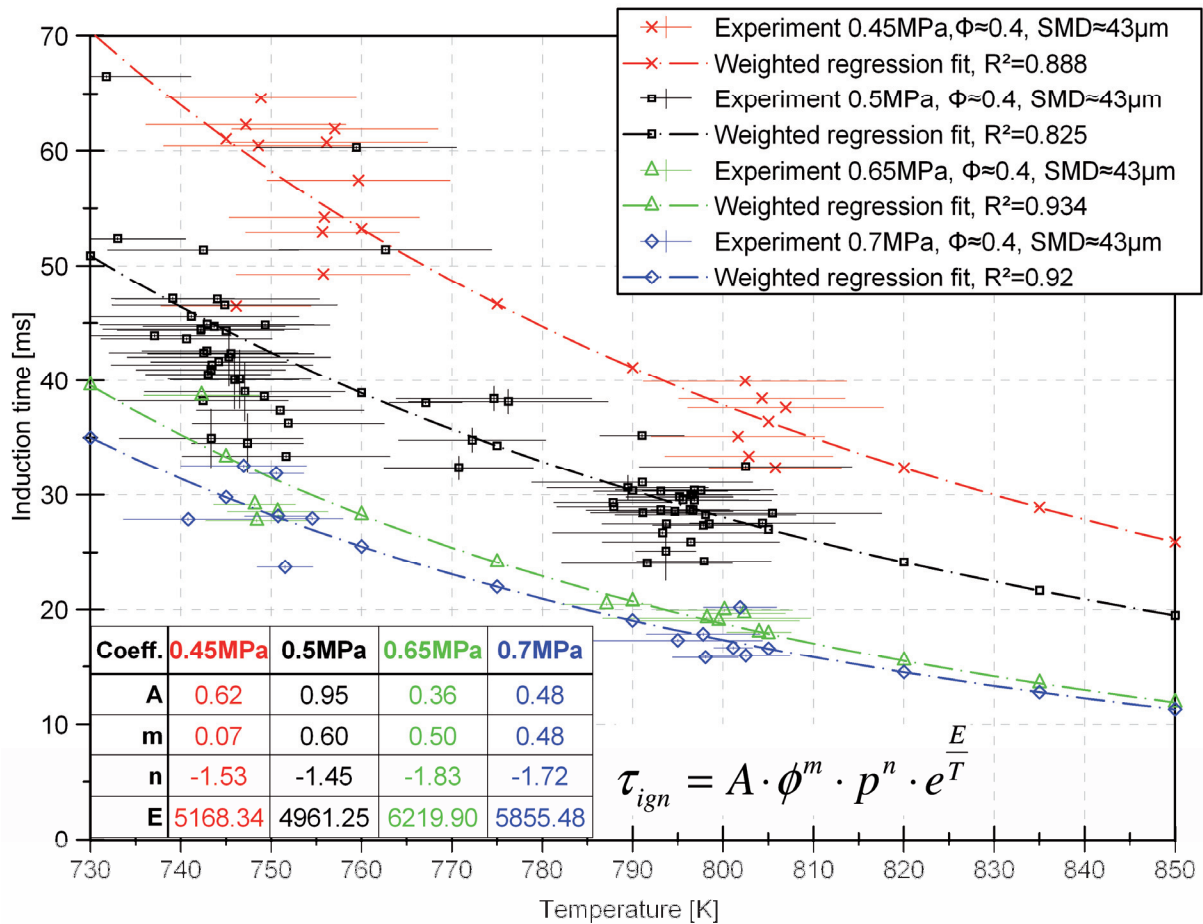


Figure 4.8 – Effect of temperature on autoignition behaviour

#### 4.1.6 Correlation between Pressure and Temperature

Having investigated the effects of pressure and temperature separately in the previous sections this section investigates the correlations between the two. Consequently Figure 4.9, shows both the graphs of temperature and pressure dependence and some exemplary connection between the two.

The unusual behaviour observed in Figure 4.7, where a higher temperature seemed to lead to lower induction times, can easily be identified as a lack of experimental data in the range of about 753K to 763K in the higher pressure ranges, skewing the curve to higher induction times. The same reasoning applies to the data in the range of 803K to 813K and higher pressure ranges.

In general this analysis indicates that the data of Figure 4.8 is better than that of Figure 4.7. This result is not surprising since keeping the pressure closely controlled in any one experiment is much simpler than temperature.

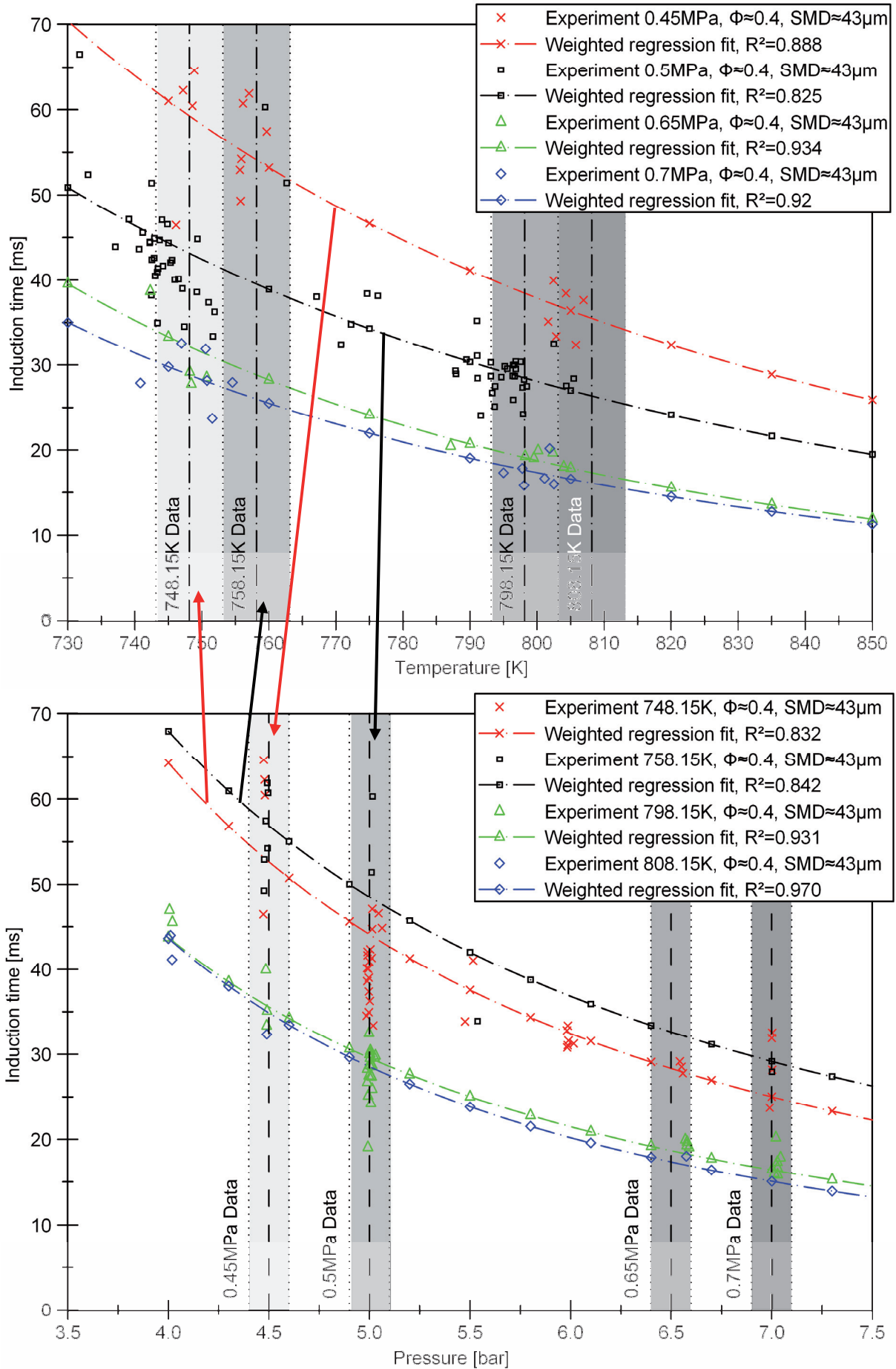


Figure 4.9 – Correlation between pressure and temperature data (deviations omitted for clarity)

If the effect of pressure and temperature is investigated simultaneously the result is Figure 4.10. Here the dark circles indicate all the experimental values of the previous figures and the colour-coded area shows the resulting fit of equation (4.1.1). The fit was again constructed using a minimization of the error with the Levenberg-Marquardt algorithm, but this time with two dependent variables, namely pressure and temperature. The resulting coefficients are also shown in the figure. With these coefficients  $R^2=0.881$ , indicating a sufficient but not a good fit.

The vectors pointing towards the experimental data points serve mainly illustrative purposes, so that the corresponding value in the fit surface can easily be identified. This shows that the deviations of the experiments from the Arrhenius type fit become increasingly large (both in absolute and percent terms), as pressure and temperature decrease. This trend was already observable in both Figure 4.7 and Figure 4.8 and becomes more visible here.

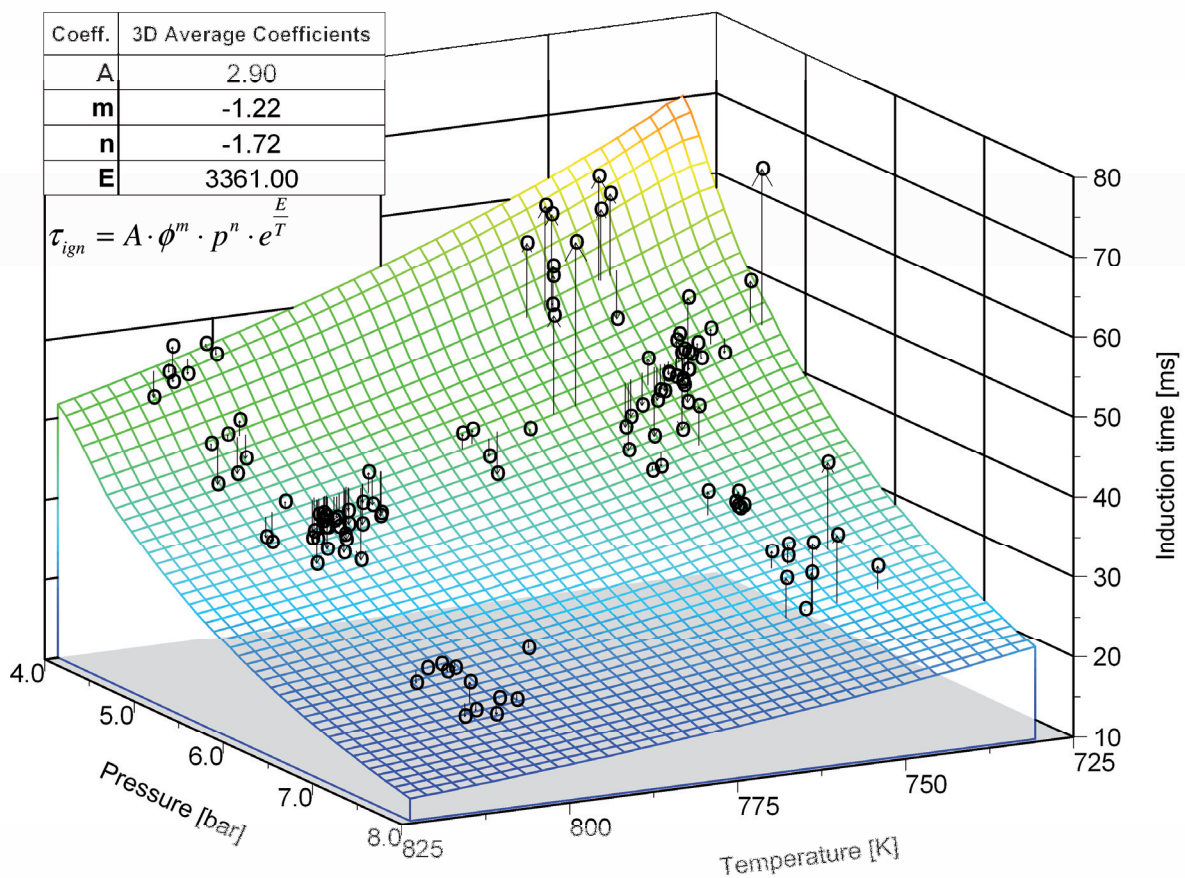


Figure 4.10 – Comparison between experiments and Arrhenius fit (3D)

A more detailed look at the deviation of the Arrhenius – type fit from the experiments can be seen in Figure 4.11. The distribution of the error is (as would be expected) a normal distribution, but it is interesting to note that the entire distribution is shifted at a higher temperature range.

The general shape of the deviation as a normal distribution can be due to two causes, which can not be separated at this point. The first being experimental uncertainty, while the second could actually be due to the nature of spray autoignition.

Since the fuel spray is polydisperse there is one prevailing droplet size ( $D_{peak}$  – see section 2.2.3) and a distribution of smaller and larger droplets around this size class. All of these droplet sizes have a different induction time and hence an ensemble of these induction times

will make up the real spray autoignition time. Consequently the prevailing droplet size will be the most likely to autoignite, but due to turbulence and other non-linear effects in spray autoignition there is also a distinct likelihood that another droplet size with a different induction time might initiate spray autoignition.

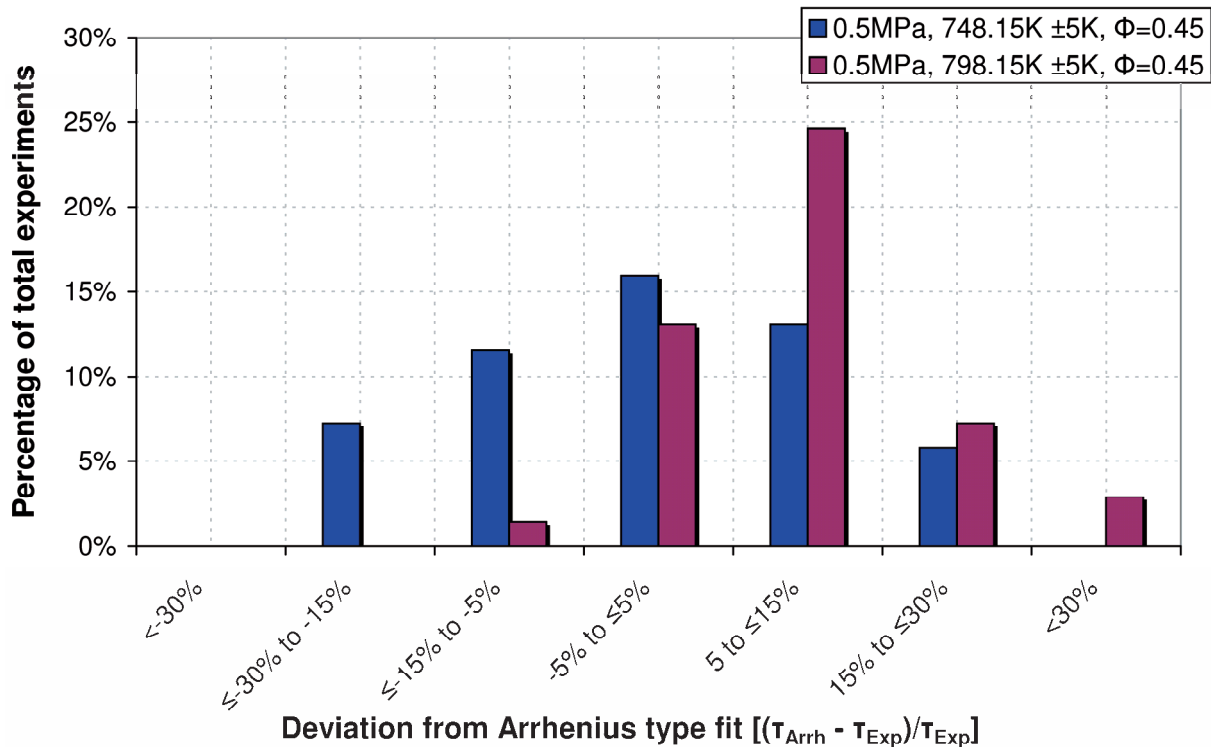


Figure 4.11 – Experimental deviation with respect to the Arrhenius fit

This in turn can lead to the observed variation in autoignition time and the distribution shown in Figure 4.11, since the Arrhenius – type fit can only assume one droplet size.

It is very interesting to note that a change in experimental temperature also leads to a marked shift in the distribution shown in Figure 4.11. At a higher experimental temperature the Arrhenius fit over predicts the induction time. This could be an indicator for the effect described above. At higher temperature a different droplet size class might become more important in terms of the spray overall ignition delay and hence the normal distribution is shifted as shown here.

In order to further investigate this phenomenon, it is necessary to look more closely at the behaviour of single droplet autoignition (which will be done in section 4.2) and then compare single droplet ignition and the combination of many single droplet ignitions to the experimental results. The latter comparison will be the subject of the final section of the results discussion (section 4.3).

Preceding these two discussions however, the final section of the presentation of the experimental results will show some interesting phenomenological findings of the experiments.

#### 4.1.7 Phenomenological observations

This section is mainly concerned with observations made during the experiments that shed more light on the highly turbulent nature of spray autoignition. The information here was obtained from the video data from the DALSA high speed camera located at the end of the

test section, with an axial view and a frame rate of 200Hz. It was originally only meant as a general observation tool and was not expected to yield any interesting findings, also partly due to its relatively low temporal and spatial resolution of only 5ms and 256x256 pixels respectively. Nonetheless, it was found that some interesting features of spray autoignition could be observed, which help further in the understanding of spray autoignition behaviour. These findings will be presented in this section.

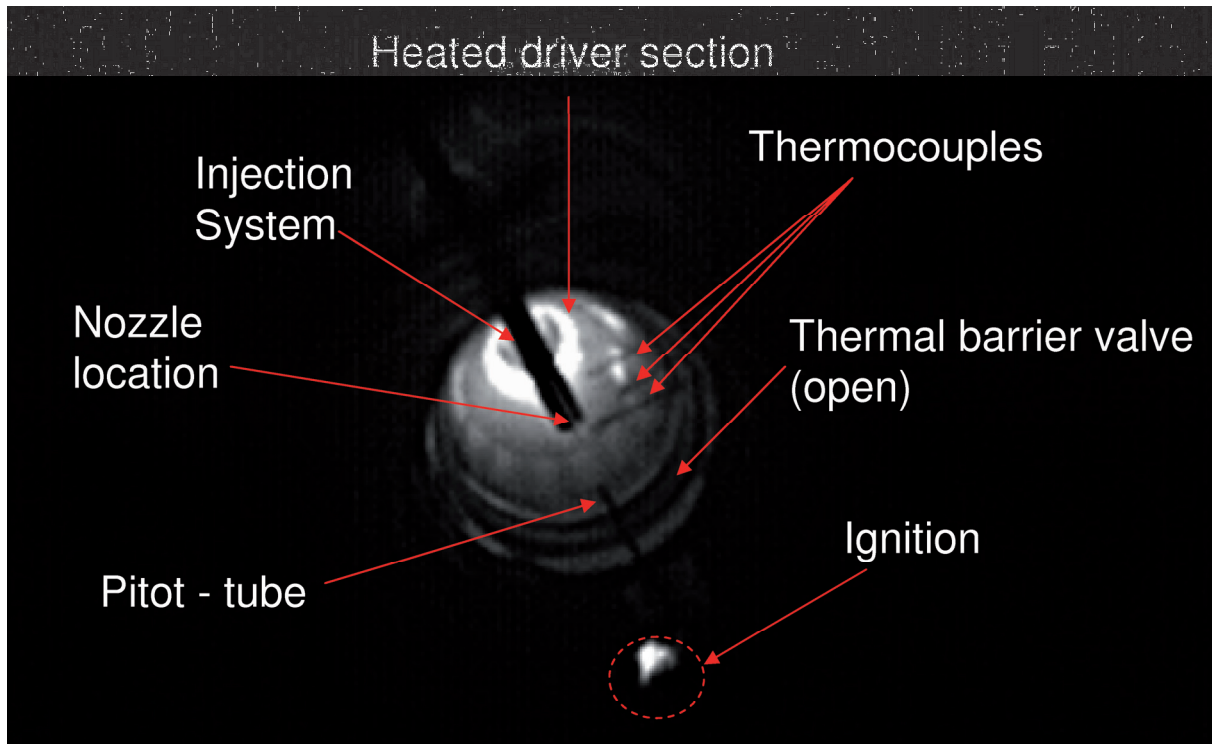


**Figure 4.12** – Annotated view from the DALSA camera

Figure 4.12, shows an annotated view from the DALSA camera. It is installed in the second to last window of the test section (see Figure 3.11) at an angle of about 30° (due to limited space and mechanical reasons). Rather than correcting the angle of the images digitally later and suffering interpolation losses, all images were left at their original angle. This should be kept in mind in the subsequent discussion of the results.

The camera's view upstream along the axis of the HWK shows many mechanical features of the wind-tunnel. The injection system (described in section 3.3.1) being prominent in the middle of the wind-tunnel. Also, some equipment is visible such as the pitot-tube (located underneath the injection system) and some of the many thermocouples. Finally, the rim of the opened thermal barrier valve (see section 3.2.2) and the glowing heated driver section can be seen. The DALSA camera used a rather old CCD chip as its detection device, which turned out to be rather fortuitous, since the CCD has fairly large light sensitive pixels and is also sensitive in the infrared range, which made the detection of ignition possible in the first place. After it was noticed that valuable information could be gleaned from the video information, a more modern CMOS camera with higher frame rate was installed, but it was not sensitive enough to detect even the glow of the heated driver section, let alone ignition.

Finally, the instant of ignition is also visible in Figure 4.12 as a “fuzzy cloud” of heated gas. It should be noted that this is hot ignition and not cool flame ignition. Nonetheless, the ignition kernel is clearly visible.

In the following discussion, the images shown are cut-outs of only the ignition region, so as to focus on the important information in these images.

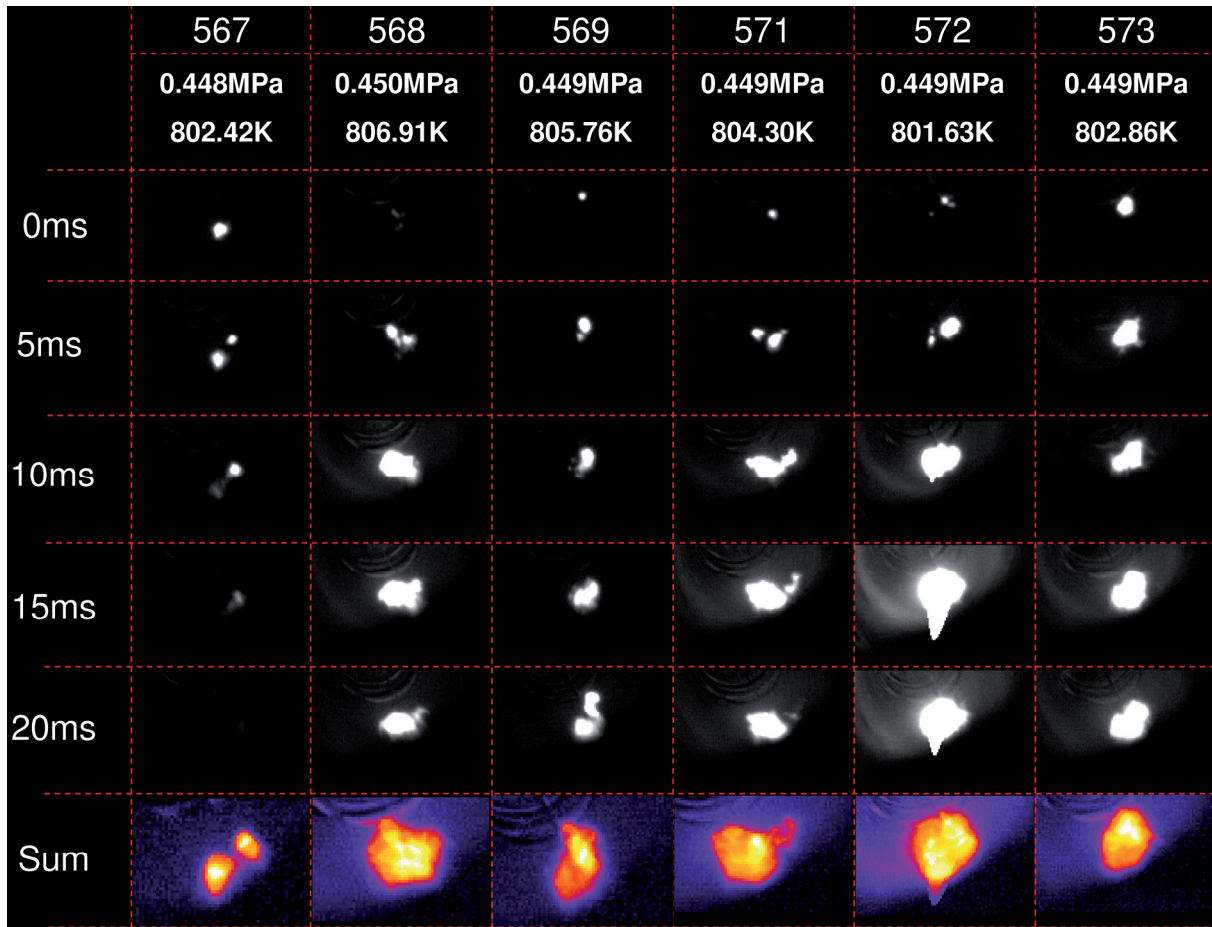


Figure 4.13 – Ignition sequence of six experiments at the same conditions

Figure 4.13, shows a series of frames from the camera of six different experiments (numbers 567-569 and 571-573). All of these experiments were done at the same conditions and conformed to the quality standards set out in section 3.7, as can be seen by the pressure and temperature data in the top line of Figure 4.13. The ignition delay in all of the above images is the same with an average of 36ms and a variation of only  $\pm 3$ ms.

The final line of images is the addition of all previous frames into one frame (coloured for better contrast). This allows the total visualization of the ignition area and possible propagation of the flame through the fuel spray.

At first glimpse the ignition event and the subsequent burning of fuel, proceed very differently in each experiment, but on closer inspection there are many similarities. Although the actual measurement of induction time is completed as soon as the first light hits the photodiodes (slightly preceding the first frame in this series as the diodes are very sensitive), the subsequent images give valuable information about the processes that were invisible beforehand.

One such similarity can be seen in the image series at 5ms. With the exception of experiment number 573, there are always two ignition kernels. Even in experiment number 573 a distinct asymmetry can be seen, which also hints at this phenomenon. This behaviour can also be

found in images from other experiments (experiments 768 and 772) of time step 0ms, albeit very weakly, enhanced images of which can be seen in Figure 4.14.

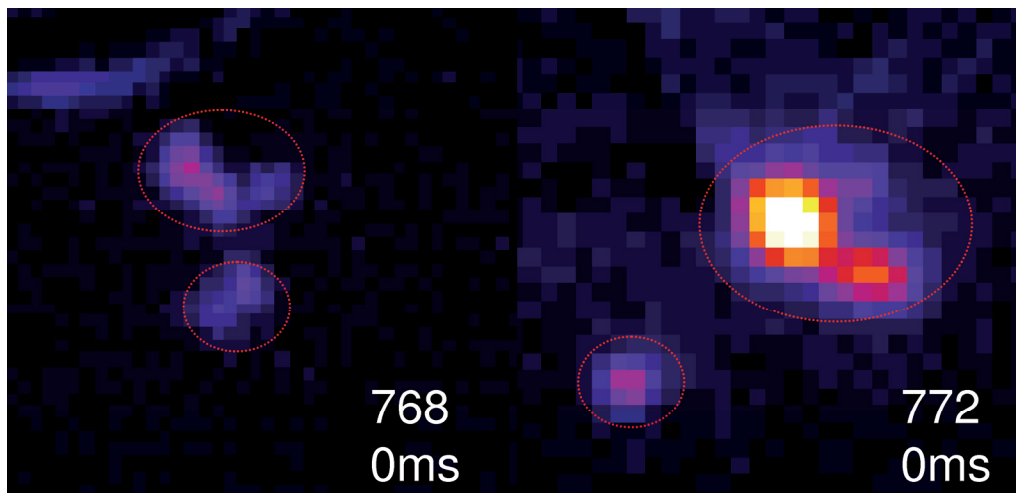


**Figure 4.14** – Moment of ignition of experiments 768 and 772

This dual ignition mode is very interesting as it shows that ignition can happen independently and simultaneously (within the 5ms resolution of the camera) in many locations at once – a single igniting droplet does not necessarily lead to the complete ignition of the spray. This is also exemplified by the image series of experiment 567 – where two independent igniting and burning kernels exist from ignition to extinction.

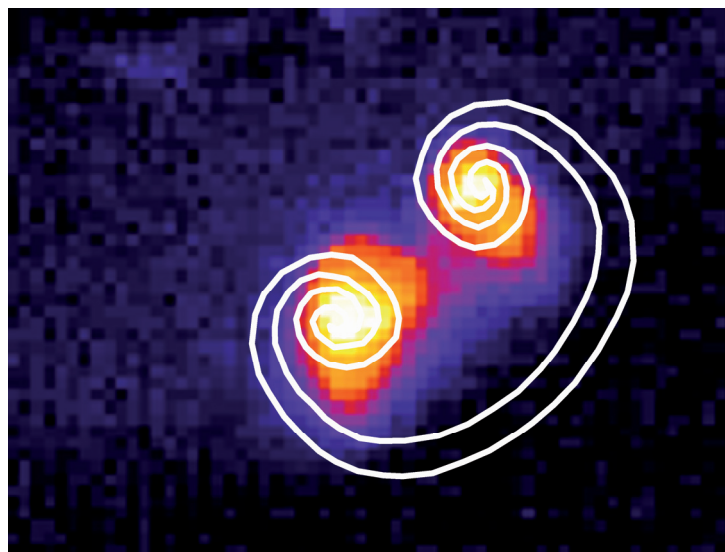


**Figure 4.15** – Large-scale spray structure and ignition locations (average of experiment 567)

Due to this dual ignition and burning mode, experiment 567 is also suited very well to a further investigation concerning the most probable connection between the large scale JICF structures and ignition locations. Figure 4.15 shows the vortex structure proposed by Lim et al. [65], superimposed on the sum of all ignition frames. It can clearly be seen that the ignition kernels are located inside the two main vortices (keeping the camera angle in mind). This finding coincides very well with the findings of Edwards et al. [9] and Sato et al. [8], who found that ignition occurs in eddies containing fuel spray mixtures and at the spray tips respectively. Both investigated a plain jet diesel injection into stagnant air.

This can now also be extended to JICF configurations, where the ignitions happen mainly inside one of the two main vortices. As was mentioned above, the induction times for all of

the above experiments were the same with 36ms ( $\pm 3$ ms), while the location can vary depending on the exact conditions in the spray JICF structure and mixture ratio, which is highly turbulent.

The same kidney like structure to ignition with initially two main ignition locations can also be seen in all other experiments shown in Figure 4.13.

Finally, the summation of all frames of the entire ignition, burning and extinction sequence shows that the spray flame stays roughly at the same location, since no large “smeared” or “streaked” structures can be seen in the summed image. This also compares very well with other findings from continuous flow devices [22, 23, 25], and indicates that the flow speed and flame speed are roughly the same.

## 4.2 Numerical Results

The results of the CVS described in section 2.3, will be highlighted in this section. Since the numerical simulations have to be compared to a vast number of experimental parameters, which are not necessarily always precisely adjustable (or even measurable), it was decided to construct a large lookup table. This table encompasses the following parameter range:

- Pressure: 0.35 – 2.00MPa
- Temperature: 680 – 900K
- Droplet diameter: 5 – 500 $\mu$ m
- Mixture ratio (Fuel/Air): 0.4-2

This leads to a rather large computational requirement of 4320 single droplet simulations. This computation was done on up to 14 individual CPUs and took several months to complete.

The resulting table is used to interpolate the induction delay of any number of parameters within the above parameter space, with reasonable accuracy. The interpolation strategy was a linear interpolation in a four-dimensional parameter space.

As a reminder, the induction delay here is always the total induction time or the time to hot ignition, which is defined as the time when any point in the gas phase reaches a temperature of 1300K (see section 2.3.3) [58].

### 4.2.1 Effect of Pressure and Temperature

Analogous to the previous experimental section, this section will first examine the effects of pressure and temperature on induction times. It should always be kept in mind, that the ensuing discussion is concerned with the ignition of a single droplet, while the experimental section treated the ignition of an entire spray. Consequently, the results differ somewhat and some peculiar effects such as ZTC (Zero Temperature Coefficient) and NTC (Negative Temperature Coefficient) [58] behaviour will be far more pronounced, than would be the case if a large assemblage of droplets were investigated. A detailed comparison and discussion of the experimental and numerical results will follow in the next section.

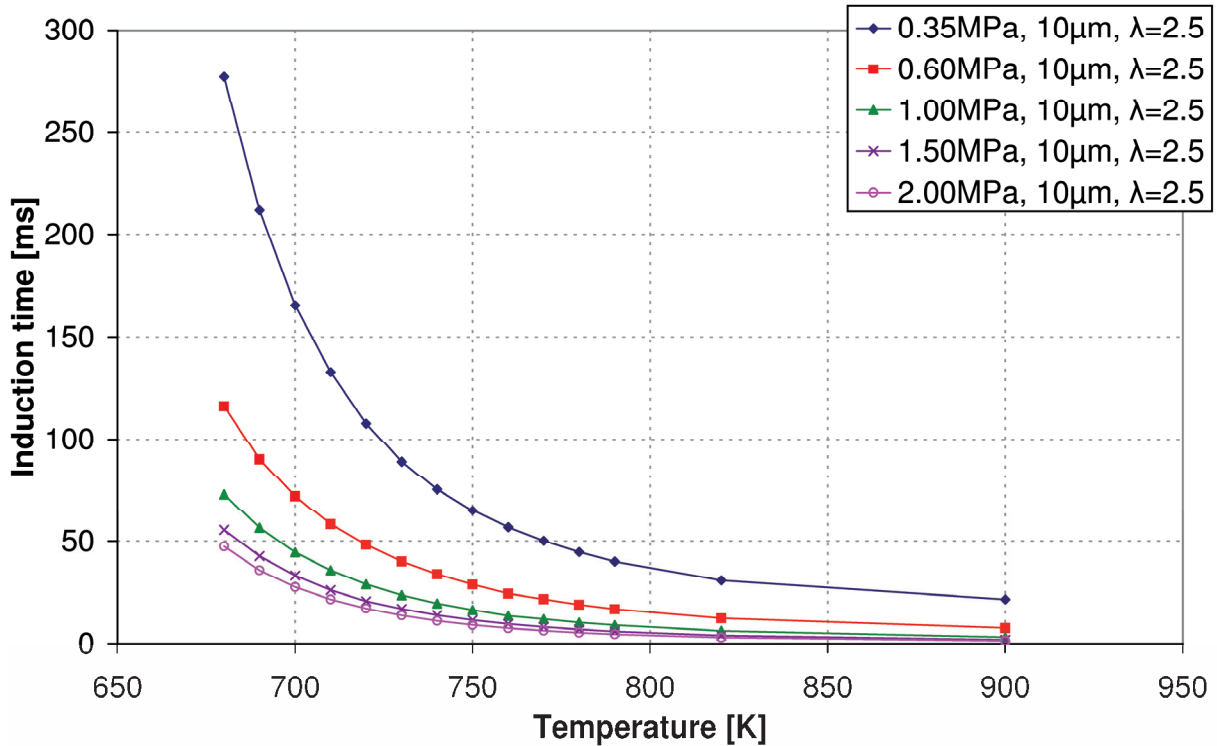


Figure 4.16 – Effect of pressure and temperature on a small droplet (lean mixture)

Figure 4.16 shows the ignition delay for a small single droplet in a lean (overall) gas atmosphere. The initial equivalence ratio of 2.5 is set by varying the size of the gas shell around the droplet until the desired value is obtained. This value is set initially and then remains constant throughout the simulation, ensuring that the global mixture ratio will remain the same throughout the entire simulation.

As was expected from the experimental results in general a higher pressure and higher temperature lead to lower induction times. The effect of both pressure and temperature increases however diminishes with each higher increment. The autoignition characteristic is hence very much in accordance with an Arrhenius type ignition.

If one considers very large droplets (500 $\mu$ m) the effects observed remain largely the same (Figure 4.17), the large droplets however tend to ignite later than the smaller ones at a given pressure and temperature level (in this lean environment at least).

But on closer inspection it can be seen that a higher pressure does not necessarily cause a more rapid ignition. The reason for this is the difference in ignition mode between small and large droplets. While the small droplets (Figure 4.16) evaporate very quickly and the subsequent ignition happens in a homogeneous gas phase, the large droplets remain intact until the point of ignition. Hence the ignition with large droplets is not taking place in a homogenous mixture but a heterogeneous one [5].

This means, while the ignition of small droplets is mainly controlled by the chemical induction time (the time to droplet evaporation and establishment of a homogenous mixture being short in comparison to the total induction time), while in large droplets it is controlled by both physical and chemical induction time and the complex interplay between the two.

This is also the reason for the behaviour exhibited in the higher temperature range (>700K) of the high pressure simulation (1MPa) in Figure 4.17, where a slower chemical path (the result of the cool flame) inhibits the hot flame ignition leading to a ZTC.

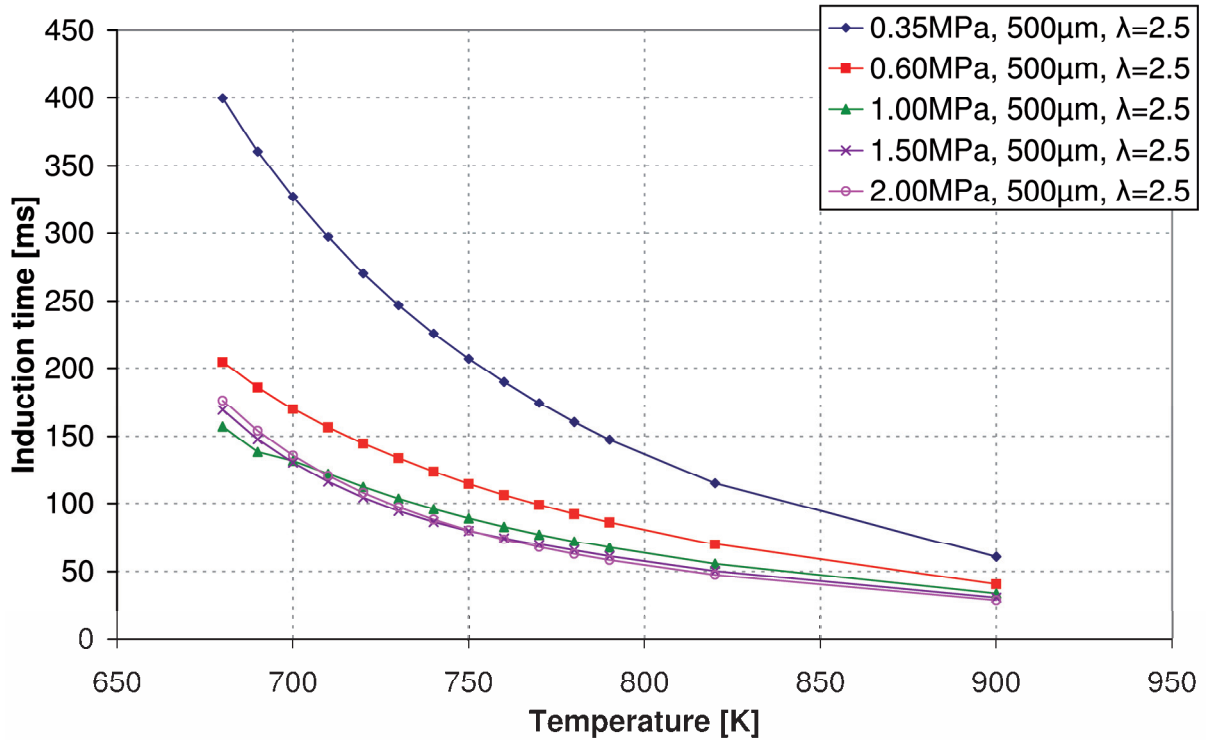


Figure 4.17 – Effect of pressure and temperature on a large droplet (lean mixture)

This behaviour becomes dominant, when medium size droplets are considered. Figure 4.18 shows the ignition of medium sized droplets in a lean ambient. Here, the ZTC becomes a NTC in the lower temperature regions.

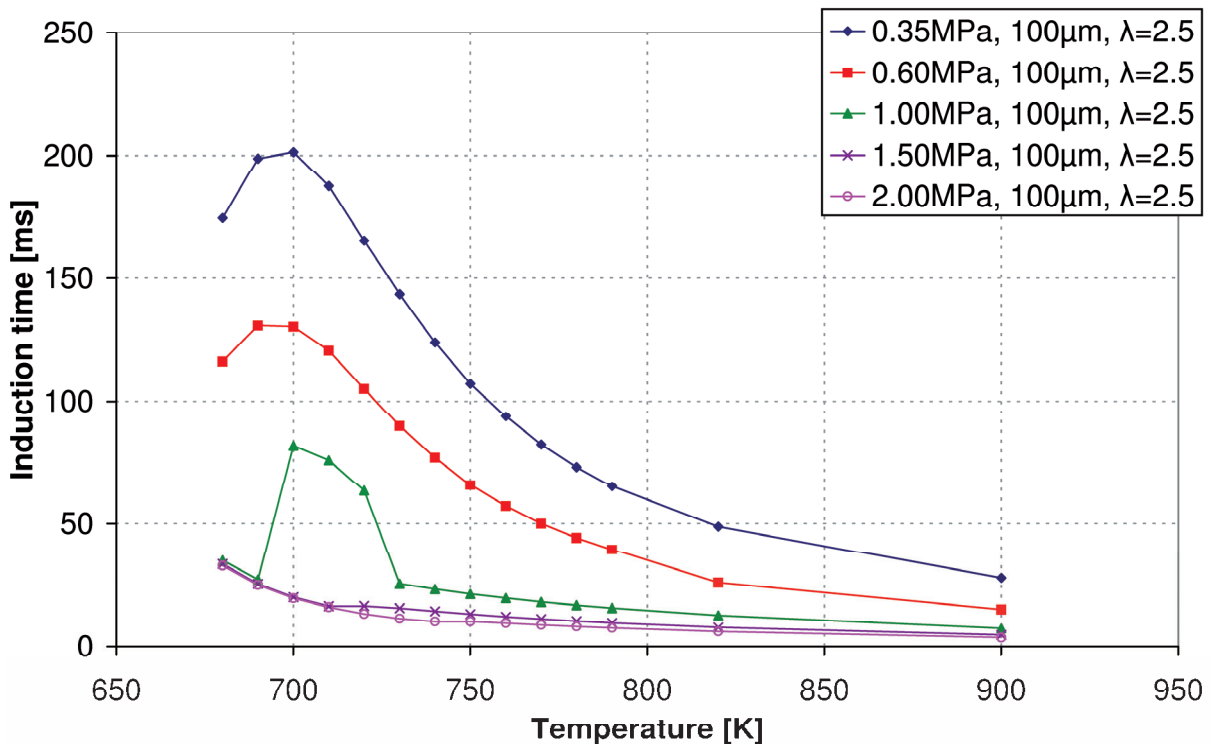


Figure 4.18 – Effect of pressure and temperature on a medium droplet (lean mixture)

The effect is especially pronounced in the 1MPa simulation between 690 and 700K and since it has such a drastic effect, more than doubling induction time within just a 10K span it is worthwhile to examine this effect more closely.

The two simulations are compared in Figure 4.19 and it can be seen that the increased temperature not only has a significant effect on the droplet evaporation time, but also a pronounced effect on the domain maximum temperature. The slightly increased initial temperature causes an early ignition of a pronounced cool-flame, as opposed to only a small cool-flame very shortly before ignition of the hot-flame.

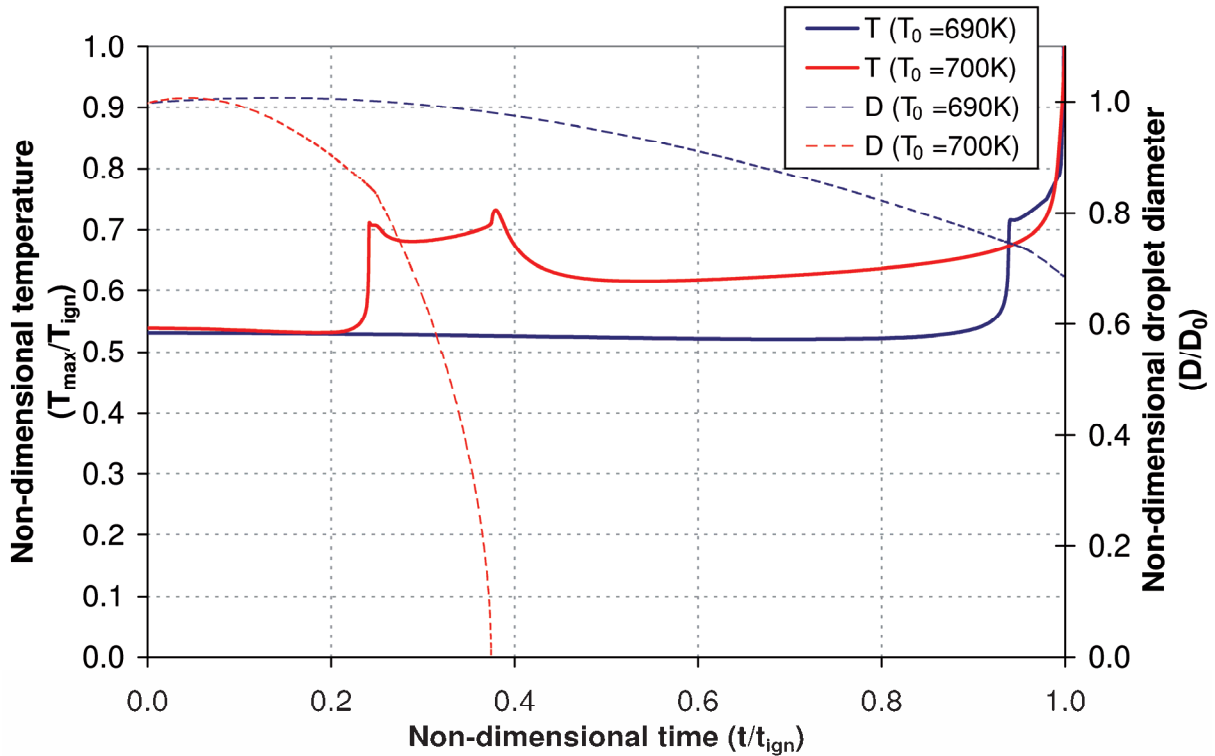


Figure 4.19 – Comparison of two medium sized droplets ( $100\mu\text{m}$ ,  $\lambda=2.5$ , 1MPa) at the NTC border

Evidently a cool-flame igniting early on causes a delayed hot-flame ignition, which is in accordance with findings by Schnaubelt et al. [5, 29]. There are two main causes for this behaviour. As can be seen in Figure 4.19 ( $T_0=700\text{K}$  case) with the onset of the cool – flame, the droplet evaporation rate increases and the droplet vanishes long before hot flame ignition. The intensity of the cool-flame is fairly high at first and then drops when there is no fresh supply of fuel due to the disappearance of the droplet. This behaviour is connected with the second reason for delayed ignition within the presence of a cool – flame, the reaction mechanism. It is displayed in Figure 4.20 and was developed by the “Institute für Technische Mechanik“, at RWTH Aachen. This is the standard mechanism used in the CVS.

The second reason for an increased ignition delay due to the cool-flame is the competition between, the left and right branch of the reaction mechanism shown in Figure 4.20. While the higher temperature reactions strive to directly terminate the reaction in final reaction products, the lower reaction temperature branch uses the educts to prepare the longer molecules for later breakdown into the final products. While the ignition of the cool – flame for these competing processes is highly dependent on temperature, the actual cool – flame burning time (second induction time) is mostly dependent on pressure [5, 30].

In the case of the simulations shown in Figure 4.19, the early ignition of the cool-flame leads to a larger concentration of these low temperature products, leaving only very few highly fractured components, which leads to a suppression of the high temperature path and consequently a longer induction time [30, 58]. A classical indicator for the cool – flame formaldehyde ( $\text{CH}_2\text{O}$ ) clearly shows this in Figure 4.21. In the  $T_0=690\text{K}$  case the production

of formaldehyde starts rather late and with a much lower gradient than the  $T_0=700\text{K}$ . In the latter case, the production of formaldehyde starts much earlier and more rapidly, indicating a strong cool – flame.

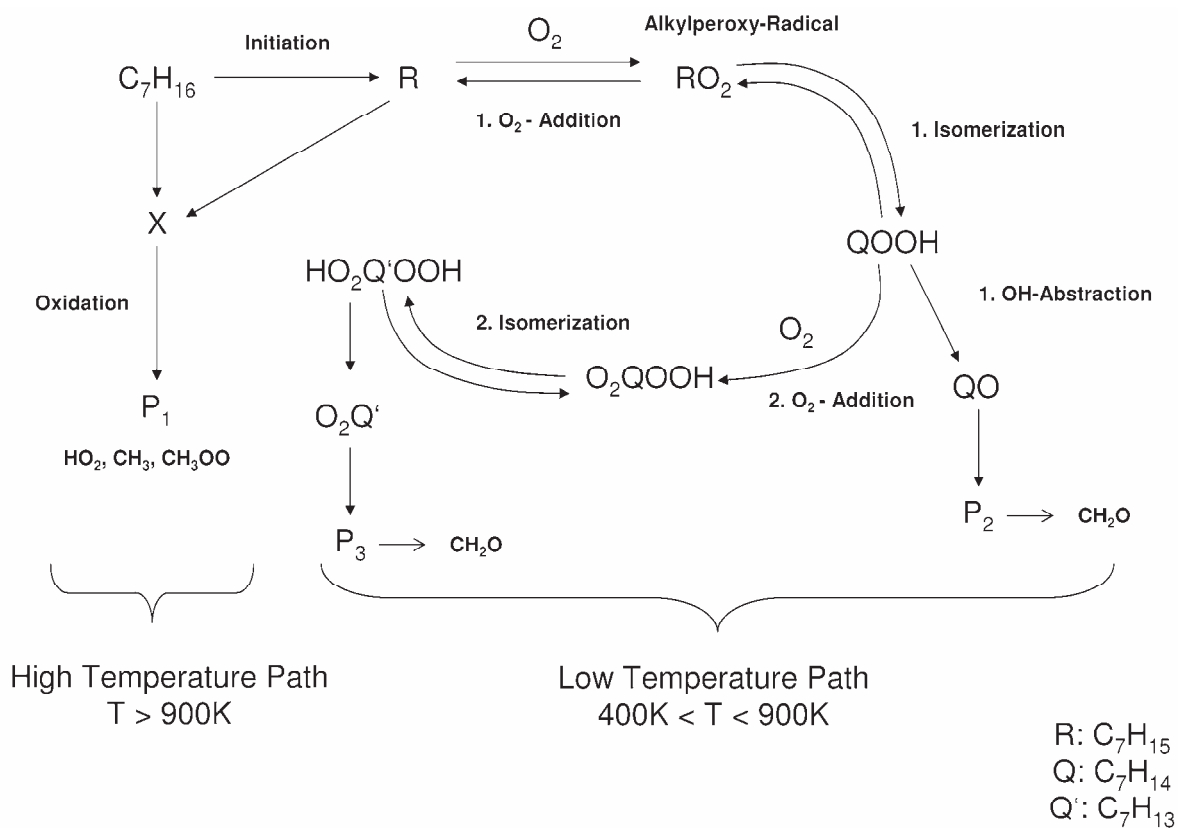


Figure 4.20 – n-Heptane reaction mechanism used in CVS (developed by Institute für Technische Mechanik at RWTH Aachen) [58]

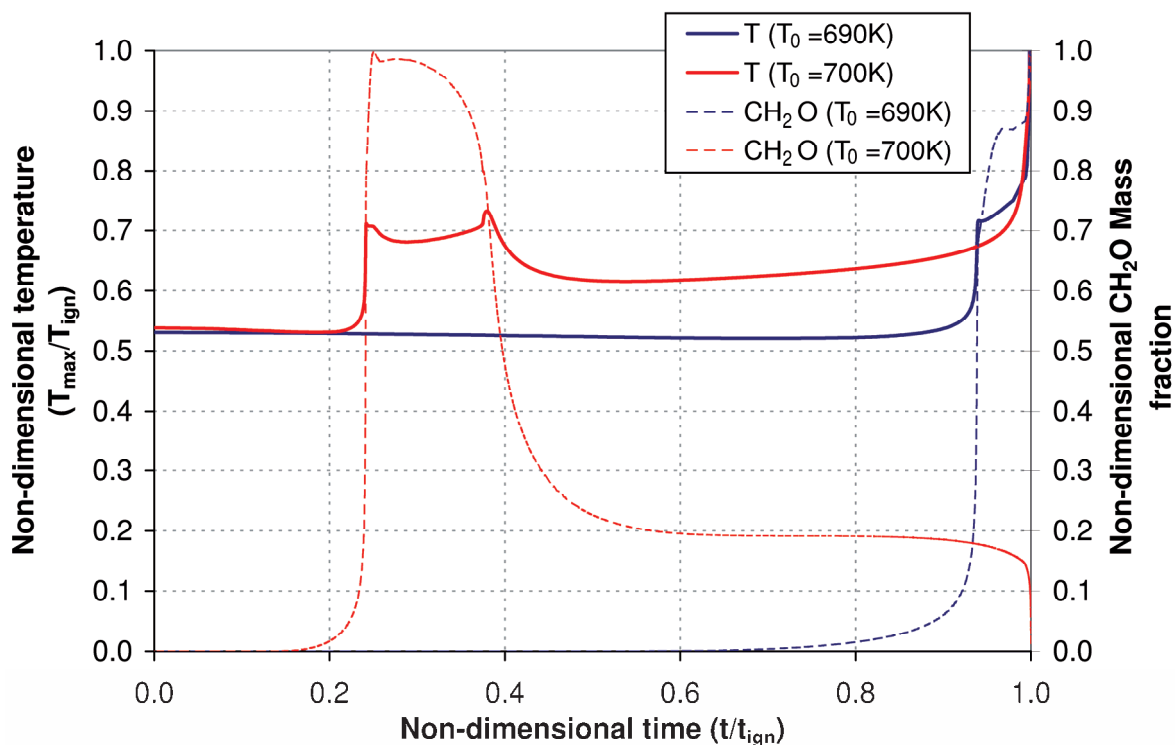


Figure 4.21 – Comparison of two medium sized droplets ( $100\mu\text{m}$ ,  $\lambda=2.5$ ,  $1\text{MPa}$ ) at the NTC border ( $\text{CH}_2\text{O}$  concentration)

#### 4.2.2 Effect of Droplet Diameter and Mixture-ratio

In order to gain further understanding of single droplet ignition, it is helpful to relate induction time to the droplet diameter and vary pressure, temperature and mixture ration. The results of this are displayed in Figure 4.22 to Figure 4.24.

The above analysis showed that there is a sharp demarcation line in terms of droplet diameter, where the induction time changes very abruptly in a given temperature range. The question remains, whether this is always the case at a certain droplet diameter, or if the limiting diameter itself is dependent on the physical parameters.

Figure 4.22, clearly shows that the limiting case is highly dependent on temperature. At lower temperatures, even large droplets exhibit a NTC. As the temperature rises, the limiting droplet size is reduced and the NTC itself is reduced, becoming a ZTC at about 800K.

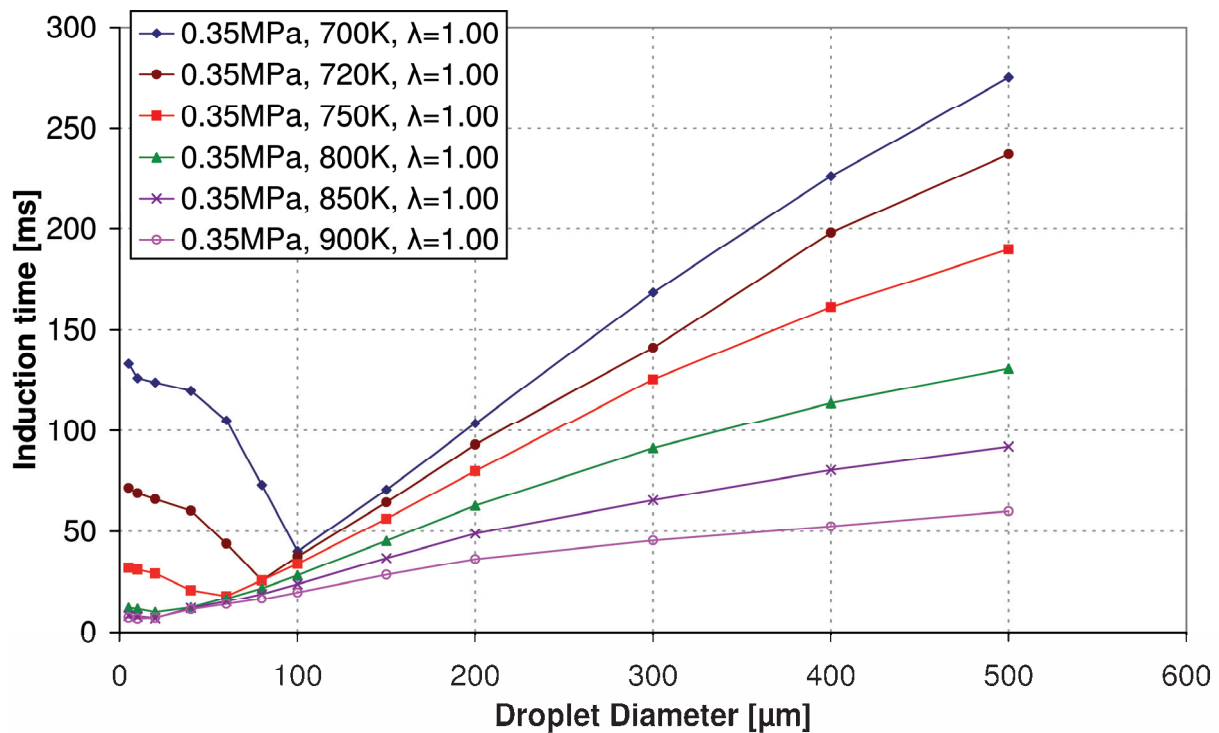


Figure 4.22 – Effect of temperature and droplet size (pressure and mixture ratio constant)

The determining factor is the droplet evaporation time. At lower temperature a large droplet can evaporate slowly with only a limited amount of chemical reactions, which are fairly slow due to the low temperature. If the droplet evaporates fully on the other hand, the ignition will be a full gas phase ignition, which is highly temperature dependant and decreases in induction time at higher temperature, since it is only governed by chemistry and not the physical processes [5, 29].

The same phenomenon can also be seen in Figure 4.23, although much less pronounced. Tanabe et. al. [70] showed that the first induction time (cool-flame ignition) is highly dependent on temperature, while the cool-flame burning time and consequently second induction time is highly pressure dependent. This means that pressure sensitivity of the total induction time is most pronounced in cases, where a strong cool-flame is present.

The limiting droplet size for minimum induction time is constant with pressure (indicating similar cool-flame behaviour); consequently an increase in pressure causes a reduction in the induction time, but no change in the overall shape of the induction time – droplet diameter curve.

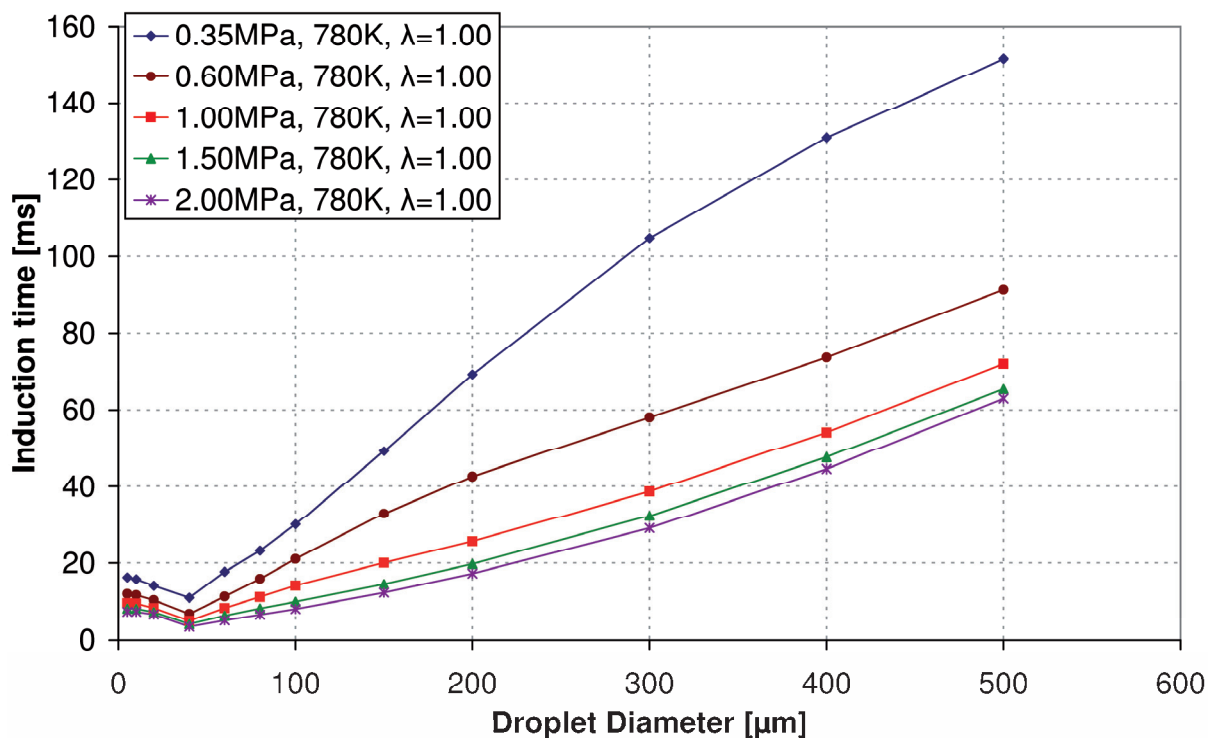


Figure 4.23 – Effect of pressure and droplet size (mixture ratio and temperature constant)

Finally, there is also the global mixture ratio to consider, the numerical results of which can be seen in Figure 4.24. While the global mixture ratio has hardly any effect on the induction time beyond a limiting droplet size, the ignition of smaller droplets is strongly influenced by the overall mixture ratio.

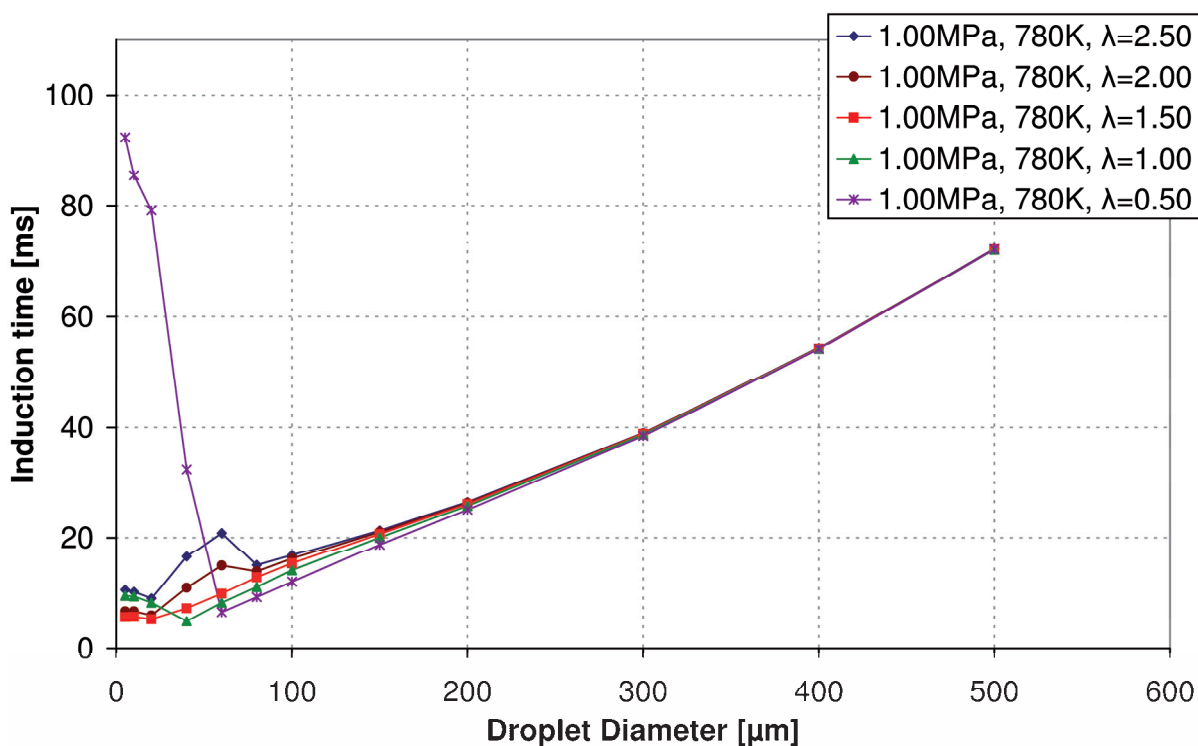


Figure 4.24 – Effect of mixture ratio and droplet size (pressure and temperature constant)

The reason for this is the ignition of these droplets before they fully evaporate. The resulting gas phase will hence behave according to the global mixture ratio, stoichiometric and

lean mixtures igniting quickly, while overly fat mixtures will only be able to ignite via the slow reaction path (Figure 4.20) due to the lack of available oxygen for the faster path. In Figure 4.24, the chosen temperature is fairly high meaning that the limiting droplet size is low (see Figure 4.22) a decrease in temperature will increase the limiting droplet size.

This concludes the description of the numerical results. By their nature the numerical simulation always give a wealth of information on the complex interplay between physical and chemical processes in a single droplet ignition.

The subsequent section will compare the numerical results with the experimental results.

### 4.3 Comparison of Numerical and Experimental Results

The numerical results of the CVS were first compared to the experimental results by simulating a single droplet with a diameter equal to the SMD of the spray and measured parameters of the spray. This type of simulation is a close representation of a monodisperse equidistant spray as shown in Figure 4.25.

The vessel for each droplet is closed to its surroundings and the conditions within each vessel are the overall global conditions measured during the experiment. Since the CVS is independent of its surrounds only one representative droplet needs to be calculated for each experiment. This is of course computationally advantageous, but has the drawback of vastly simplifying the problem at hand, by only taking global conditions into account. This means that as long as the flow field is fairly uniform this approximation holds, but if the flow is varied (for example due to turbulent mixing devices) this model is no longer valid.

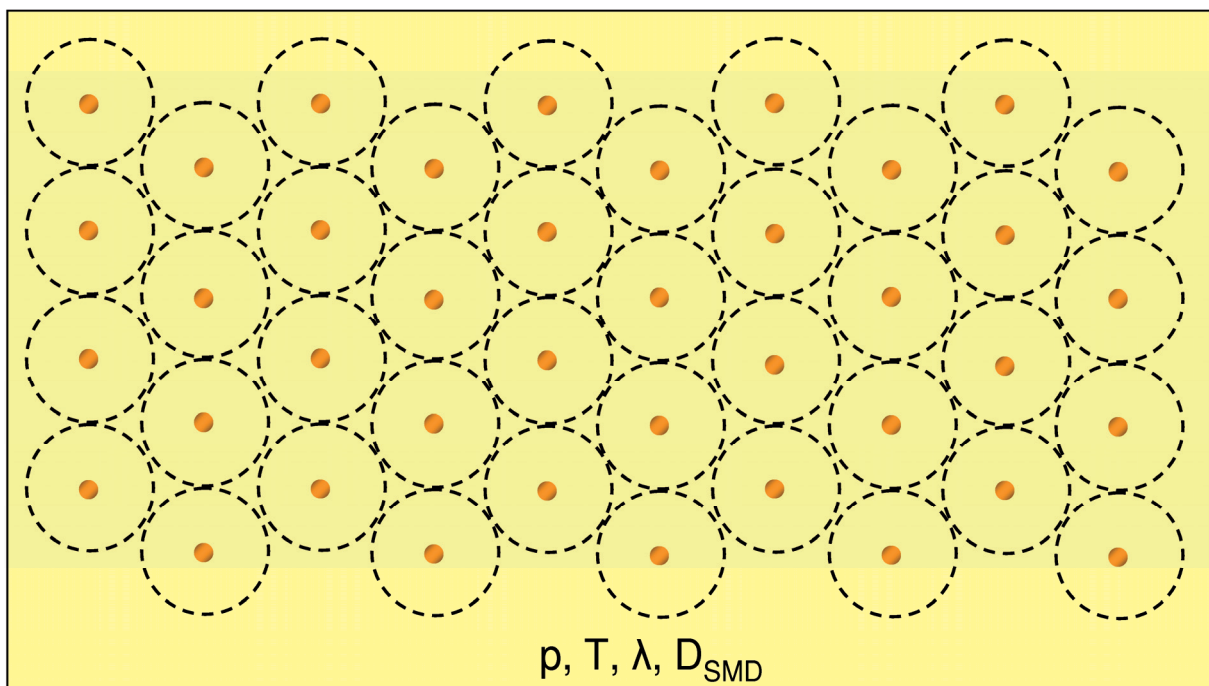


Figure 4.25 – CVS as a monodisperse equidistant spray

The results of this comparison were first presented during the ISPS 2007 [71] and are reproduced here in Figure 4.26

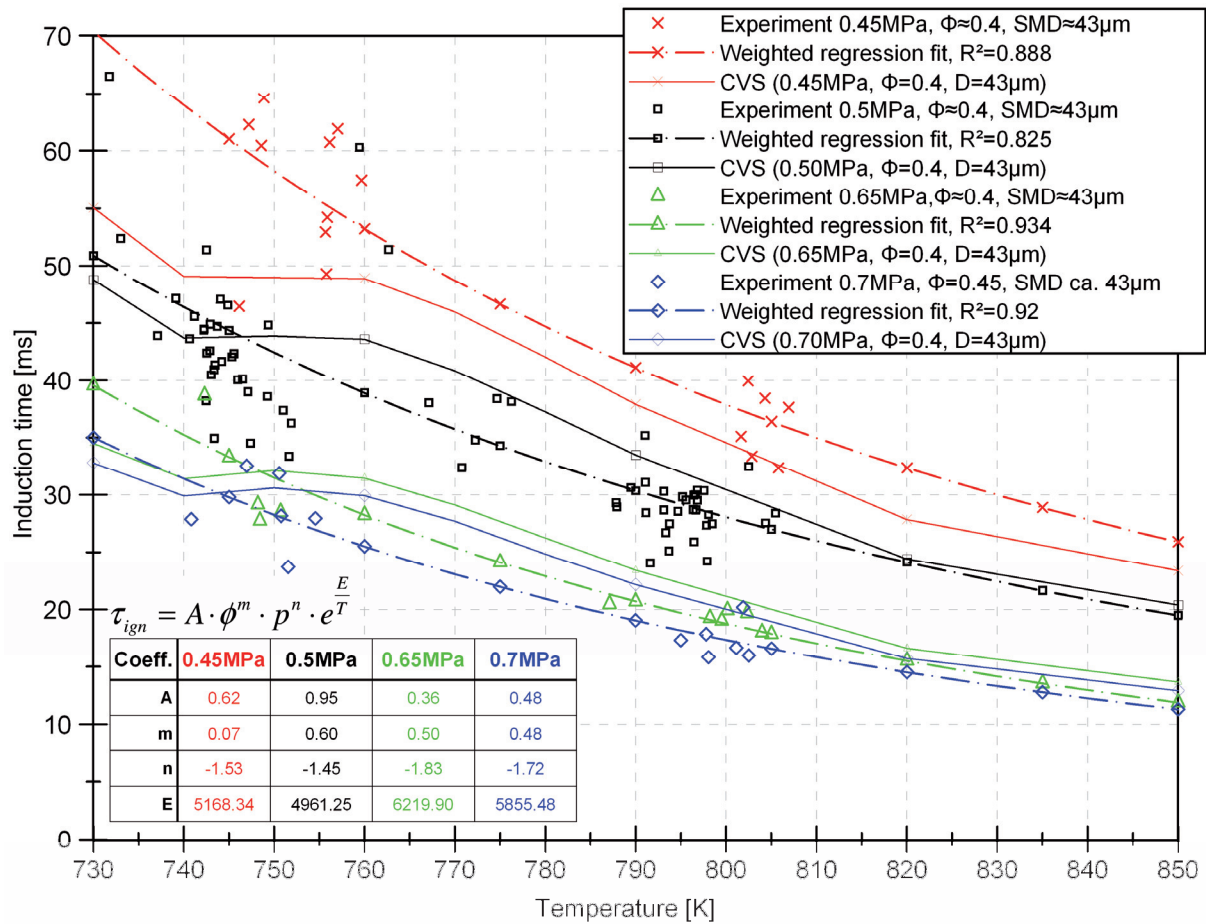


Figure 4.26 – Comparison of the numerical and experimental results (deviations omitted for clarity)

Clearly, even the very simplified simulation model of a monodisperse equidistant spray has some common features with the experimental results. In the low pressure region the simulation under-predicts the induction times significantly, but this is not so much the case with the higher pressure experiments. While the simulation indicates clearly defined NTC regions in the 740K to 760K, this cannot be identified from the experimental results.

The assumption of a monodisperse equidistant spray does provide some insight into the overall process, but as expected is too much of a simplification to enable anything more than the most general approximation. The large scatter in the experimental data cannot be explained. Nonetheless, this is the first step in describing a whole spray.

The next step taken is to assume that the spray consists of a multitude of many different monodisperse equidistant sprays, each still having the same overall mixture ratio and being subject to the same environmental conditions. The droplet size and relative amount for each of these “sub-sprays” is derived from a Rosin-Rammler distribution with  $q=2.75$  and  $X=60.7$ . These values were estimated from the available experimental data, literature values and using the relations explained in section 2.2. The resulting CVF (cumulative volume function) used in this work can be seen in Figure 4.27, with a SMD of about  $43\mu\text{m}$ , a MMD of about  $53\mu\text{m}$  and a  $D_{0.99}$  of about  $105\mu\text{m}$  and the corresponding model can be seen in Figure 4.28.

This type of model now also takes into account of the polydisperse nature of the spray in the hopes to better explain the experimental results. The flow conditions are still approximated globally and the droplets all have the same separation and no interaction is present between adjacent vapour clouds. In order to include these last factors in a model a full coupling between CFD and CVS is necessary.

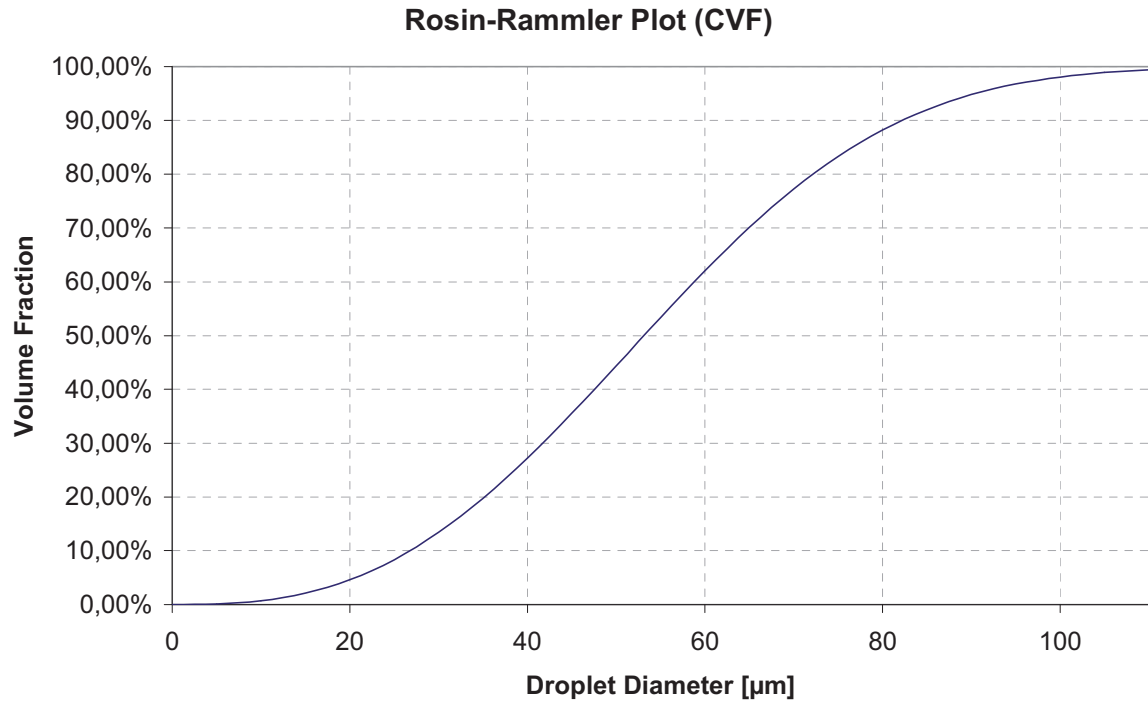


Figure 4.27 – Rosin – Rammler distribution for  $q=2.75$  and  $X=60.7$

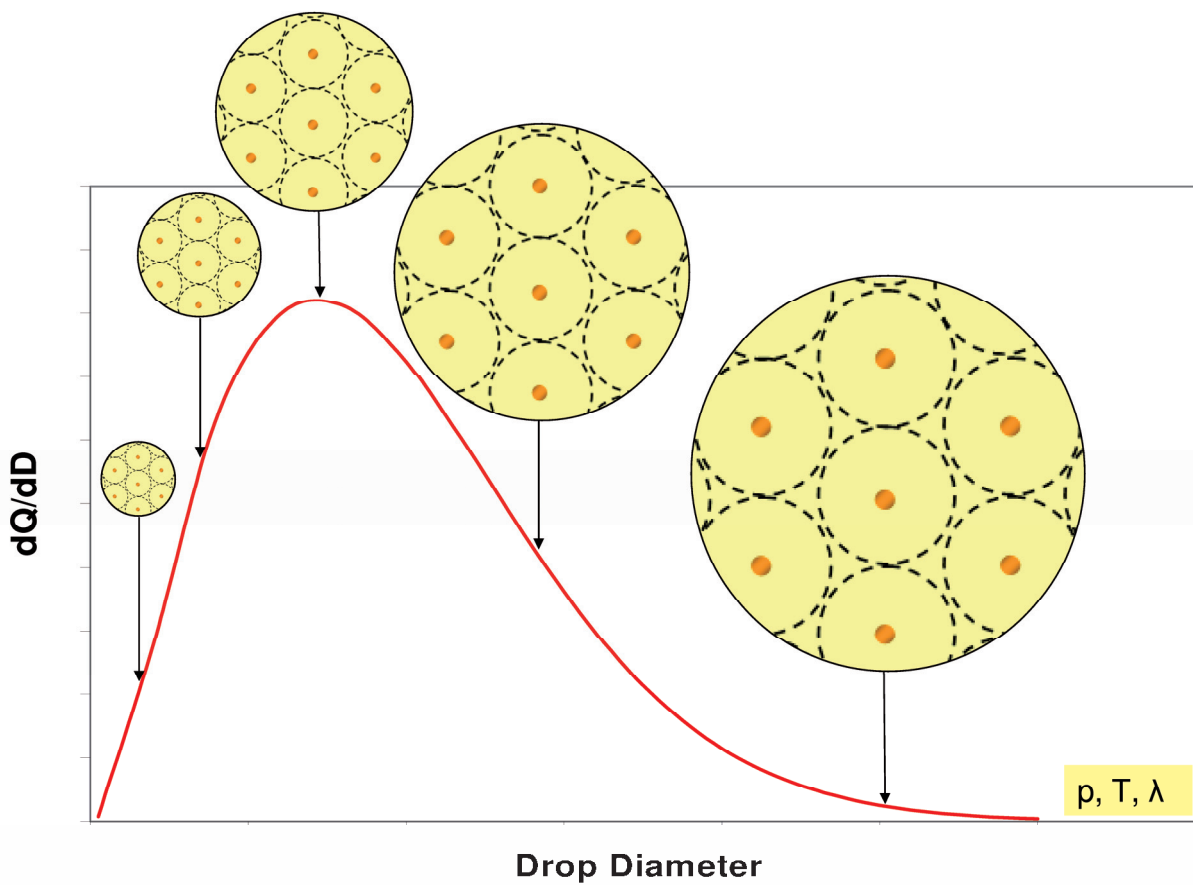


Figure 4.28 – CVS as a polydisperse equidistant model

Under the assumption of such a distribution the autoignition delay was calculated for five different droplet diameters and volume fractions, representing the main body of the spray. The calculation of these was done using the interpolation table described in section 4.2. The resulting plots can be seen in Figure 4.29 through Figure 4.30, where the data for each pressure step was separated into one graph for clarity.

In contrast to the previous results where only a monodisperse equidistant spray was assumed, the assumption of many different monodisperse equidistant sprays with different droplet sizes and volume fractions seems to fit the experimental results much better than the simple first guess assumption (as could be expected).

The MMD droplet is a much closer representation of the curve fit from the experimental results, showing almost no appreciable NTC region, which is consistent with the experimental results. Nonetheless the weak ZTC region in the 0.5MPa graph seems to be mirrored by the experimental results.

Another interesting observation that can be made in the figures is the intersection of the ignition delays for the two smallest droplet classes in the low temperature range. While the very small droplets of about  $10\mu\text{m}$  evaporate and ignite as a gas phase only, the larger droplets of almost  $40\mu\text{m}$  exhibit a distinct NTC region near 750K. This causes these droplets to ignite sooner than the smallest droplets in the low temperature range and consequently cause an inhomogeneous combustion with the associated problems in  $\text{NO}_x$  production. In addition to this the amount of droplets with the larger diameter is much higher, than the smaller droplets making an ignition of these droplets even more likely. This is supported by the experimental data as the variation in induction time increases significantly in the low temperature range where the transition is taking place.

The results show that the variations in induction time are mostly an effect of the natural turbulence and random effects found in a spray. The interaction of turbulent flow and many different droplet sizes leads to a spray ignition likelihood distribution at any given condition. The most likely ignition delay of the entire spray is not (as previously thought) the ignition delay of a droplet with the SMD, but rather the induction time of a droplet possessing the MMD (at least for a spray with fairly large droplets and a large spread – as investigated in the present work). Larger and smaller droplets can delay or expedite ignition (as the case may be) only if the conditions are correct locally at the droplet location. This scenario becomes ever more unlikely the further the droplet size deviates from the MMD, as the number of these types of droplets reduces significantly (according to a Rosin – Rammler distribution). Consequently, the occurrence frequency of the right pressure, temperature, mixture field for the right amount of time, to initiate autoignition, reduces with the deviation from the spray MMD.

This has interesting consequences for many combustion applications as it is possible to determine an average, absolute minimum and absolute maximum ignition delay a priori with this technique of combining single droplet ignition data with spray distribution information. For instance an arbitrary combustion machine operating at 0.5MPa, 790-800K, a flow velocity of about 25m/s and a plain orifice JICF injector operating at 2MPa pressure differential (lean overall lambda of about 2) can have a mixing zone of about 0.5m length after which an ignition becomes likely. Ignition will then most likely take place about 0.75m after the injection point and will definitely have commenced after about 1.2m.

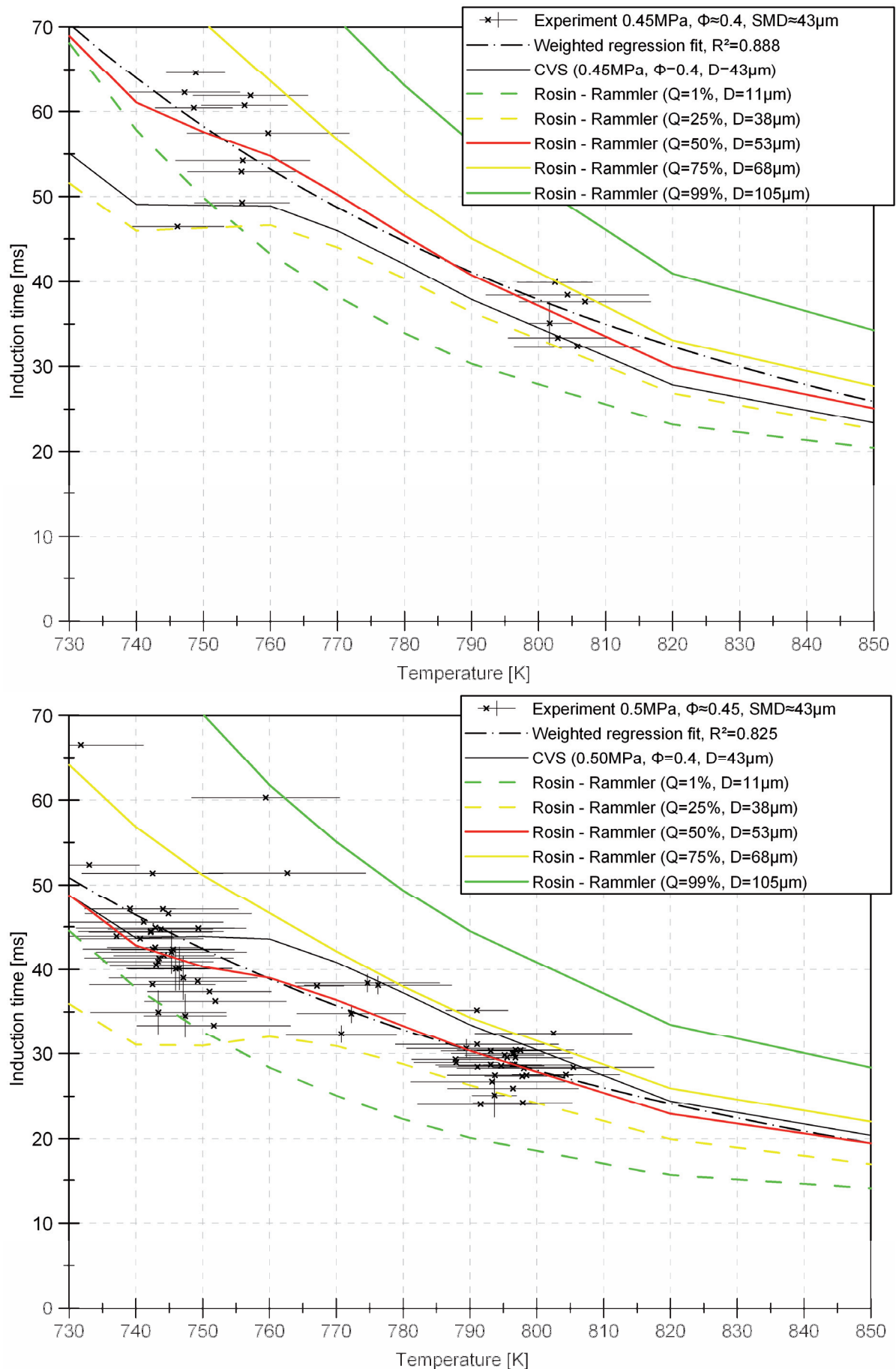


**Figure 4.29** – Spray experiment and Rosin – Rammler distribution for numerical simulation (0.45 and 0.5MPa)

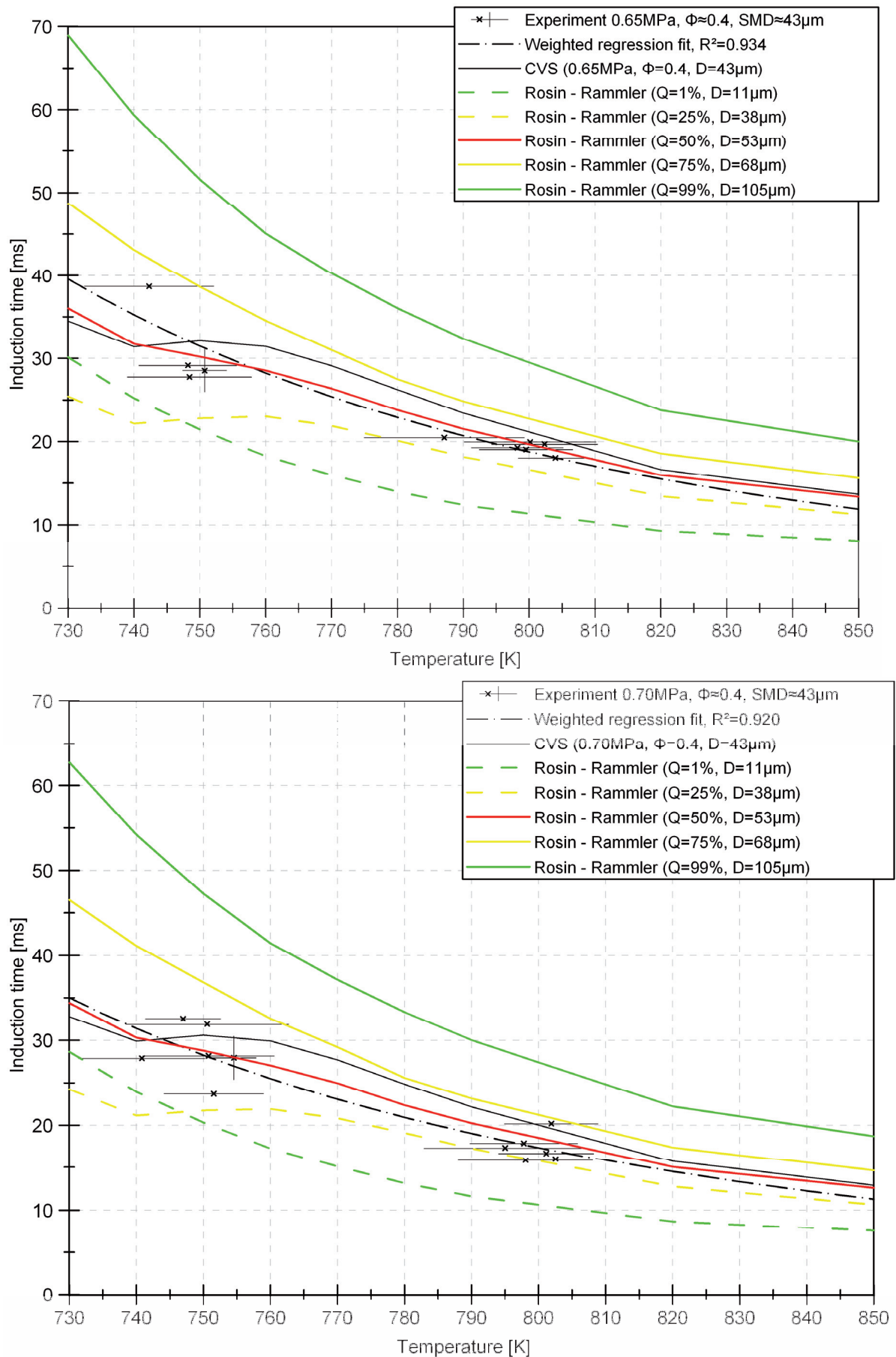


Figure 4.30 – Spray experiment and Rosin – Rammler distribution for numerical simulation (0.65 and 0.7MPa)

The above calculation was done under the assumption that no efforts were taken to prolong the induction time by aerodynamic means, such as for example mixing tubes in which a much richer mixture is created (consequently with longer induction times). The procedure presented here is only valid for the case where the spray is uninhibited and can freely form the overall mixture ratio.

This work hence represents a further step in the development of a spray autoignition simulation. The first was taken with the understanding of the single droplet ignition, the second step, was the understanding and validation of a monodisperse equidistant spray and the third the autoignition of a polydisperse equidistant spray. The final step will be the incorporation of individual droplet trajectories into the simulation and a representative selection of these for the entire spray. This will then allow the prediction of total spray ignition in a complex flow field that is established in modern mixing reactors.

## 5 Conclusion

The combustion of liquid hydrocarbon fuels be they of fossil or bio-mass derived sources is always connected with the production of certain pollutants, most notably  $\text{CO}_2$  and  $\text{NO}_x$ . Nonetheless, hydrocarbon fuels will remain an important energy source for the foreseeable future, due to their high energy density. Consequently, every effort must be taken to minimize the formation of the pollutants during the combustion process.

While  $\text{CO}_2$  can only be reduced indirectly by deriving the fuel from re-growing sources, which absorb the  $\text{CO}_2$  during growth that will later be produced during combustion (or capturing it after combustion and safely storing it),  $\text{NO}_x$  can be significantly reduced by tailoring the combustion process. The most critical factor in this tailoring is temperature, as most of the  $\text{NO}_x$  is produced due to high combustion temperatures via the Zeldovich mechanism. Since flame temperature is at a maximum when the mixture ratio is stoichiometric and decreases as the equivalence ratio becomes leaner, the goal should be to provide a very lean and even mixture of fuel and air prior to combustion – an LPP (lean prevaporised premixed) mixture. This does not only ensure a low combustion temperature and consequently low emissions, but also uses the minimum amount of fuel with maximum efficiency. Unfortunately, a lean mixture is not only prone to autoignite easily, but additionally the complex interaction of mixing fuel spray, chemical kinetics and flow interactions, that lead to autoignition are not well understood and can still not be predicted with any great accuracy.

Still, the time between injection and ignition is the only window of opportunity to provide just this elusive perfect LPP mixture. Hence the ultimate goal should be the development of a simulation that accurately predicts all processes of flow physics and chemistry up to ignition, so that this information can then be used to design the optimal combustor.

The development of such a code has been perused for many years by many workers with many different approaches. In the ZARM combustion group the methodology for the development of such a simulation has been to first understand and simulate single droplet ignitions, then modify this simulation to incorporate a variable outer boundary and connect it with characteristic droplets and their trajectories (for the spray as a whole). While the first step has been achieved, the second step is still ongoing.

This thesis represents an intermediate step in this development process by comparing the first full spray autoignition experiments (which are meant for later validation of the final code) to a single droplet ignition simulation, the CVS. This code simulates a single droplet in a completely closed environment, which is closely emulates a monodisperse equidistant spray.

The more than 800 spray experiments were conducted at the HWK Bremen and represent the first time that this facility has taken up regular experimental operation. The HWK is a hot blow down wind tunnel with a large test section diameter, operating on the principle of the Ludwieg tube. It provides conditions equivalent to those found in any modern continuous flow combustion machine.

The fuel investigated was n-heptane, which was injected into the hot flowing ambience in a cross-flow configuration in the centre of the HWK. The parameters varied in this study were ambient temperature and pressure as well as fuel temperature, while the injection pressure differential and amount of injected fuel per experiment remained constant.

To compare the experiments with the simulations, more than 4320 CVSs were conducted and their hot ignition was tabulated.

While the experimental results could be fitted to an Arrhenius type correlation there is considerable scatter in the data, especially toward the low temperature regime. The scatter is the result of the complex interactions of the spray droplets and fuel vapour with the turbulent flow. Despite the scatter, the experimental results compare well to other similar studies such as those of Wolff et al. [23], who employed a completely different experimental apparatus (a continuous flow wind tunnel), signifying that the HWK is capable of successfully simulating the conditions in other flow machines.

In addition it was found in accordance with results by Edwards et al. [9] and Sato et al. [8] that the spray tends to ignite in the two horseshoe vortices that are naturally produced in a JICF configuration.

A comparison of the experiments with the simulation showed interesting correlations, even though the gross simplification of a monodisperse equidistant spray was taken for the simulations. These simulations were done with a single droplet diameter that was equivalent to the SMD of the spray.

As a second step in the comparison many thousands of single droplet simulations were performed and their hot ignition tabulated. This data was then used to interpolate the induction times for several characteristic droplets of a spray with a Rosin – Rammler distribution similar to that of the spray injected into the HWK. The result was a distribution of the spray ignition likelihood at each temperature, pressure and global mixture ratio – which in essence represents the autoignition a polydisperse equidistant spray.

Comparing these results to the experiments leads to a good fit – now also incorporating the observed experimental data scatter. Accordingly, the scatter observed in the experimental results is mostly due to the polydispersity of the spray and its interaction with the turbulent flow established in a JICF configuration.

As a result, it is possible to predict the maximum, minimum and most likely induction times and consequently their locations, for the simple condition of a single JICF without any obstructions or special turbulence generating devices.

While the final step of predicting the ignition times and locations for any arbitrary flow pattern still requires the completion of the spraylet code, the results of this thesis show, that the methodology chosen is the right one on the path toward a complete spray simulation.

## 5.1 Outlook

On the experimental side the next step in the investigation would be to vary spray parameters, in particular the droplet distribution. To this end the injection system could be modified with a different nozzle, or different injection pressure differentials could be investigated. In order to support these measurements the spray detection methods should be improved on the experiment. One option here would be high resolution photographs of the injection event, to enable a more direct measurement of the spray droplet distribution.

Also improvements on the HWK, in particular the TBV and the temperature field of the flow would go a long way to further improve the experimental output (both in quantity and quality). Such improvements would be the elimination of air cavities in the TBV, which would increase the experimental time available by reducing the initial temperature fluctuations (see section 3.7). In addition a more air tight design would reduce the temperature gradient and reduce hot air leakage. This could not only lead to reduced thermal stresses of the test section and increase the experiment frequency (less waiting time between each experiment for the temperature to equalise) but also an improved spray history, especially in the spray history temperature variation.

Finally, more high resolution (both spatial and temporal) measurement techniques such as LIF (laser induced fluorescence) for example, along the axis of the test section will bring more insight into the exact ignition locations and the interactions between the fuel jet and air flow.

On the numerical side, the development of the spraylet code is of foremost importance. Once available, a detailed CFD simulation of the spray injection event (with input from the spray measurements for droplet distribution) and the spraylet code can be coupled and directly compared to the available experimental database.

Some of these goals could be achieved in a new project (started in late 2009) focusing on the environmental aspect of spray autoignition in particular with reference to new bio fuels of the second generation, derived from Fischer – Tropsch synthesis.

## 6 Appendix

### 6.1 Thermocouples

The thermocouples employed in this theses are of type – k. Since the experimental time is very limited with a maximum of about 100ms, the thermocouples need to have a fast response. This is best achieved by very fine wires with a very small heat capacity.

Suitable thermocouples are produced by Medterm Corp. (Huntsville, Alabama, USA), a picture of which can be seen in Figure 6.1.

The two very fine wires ( $12.7\mu\text{m}$ ) are threaded through holes in the individual wires of a larger thermocouple, then welded in place and finally coated in a ceramic resin. This type of design is very sturdy, while still exhibiting a fast response of about 4ms. The response time is dependent on the flow velocity and full graph can be seen in Figure 6.2.

Furthermore, to avoid falsified results due to thermal radiation emanating from the heated driver section, the thermocouple was shielded by a radiation shield. This ensured that only the temperature of the flowing gas was measured and had the added advantage of protecting the thermocouple from any stray dust particles, which might cause damage.

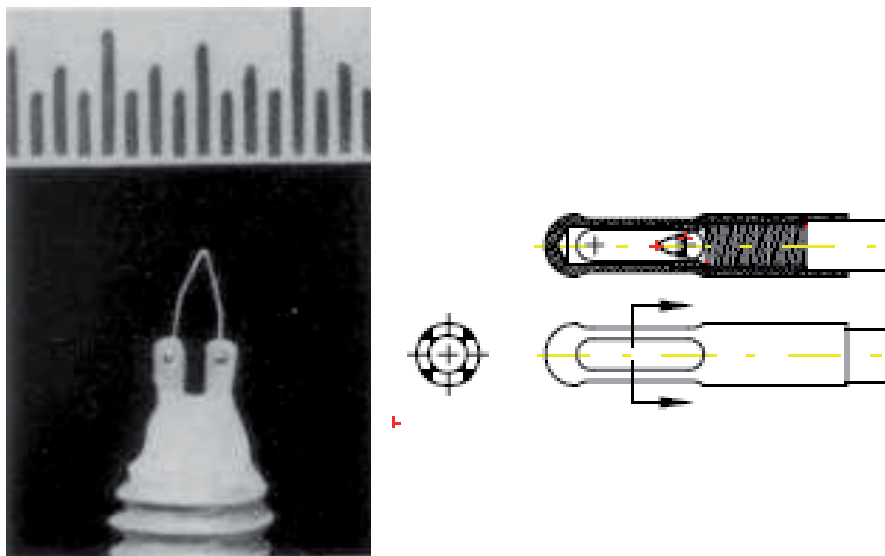


Figure 6.1 – Thermocouple (left) and radiation shield (right) [72]

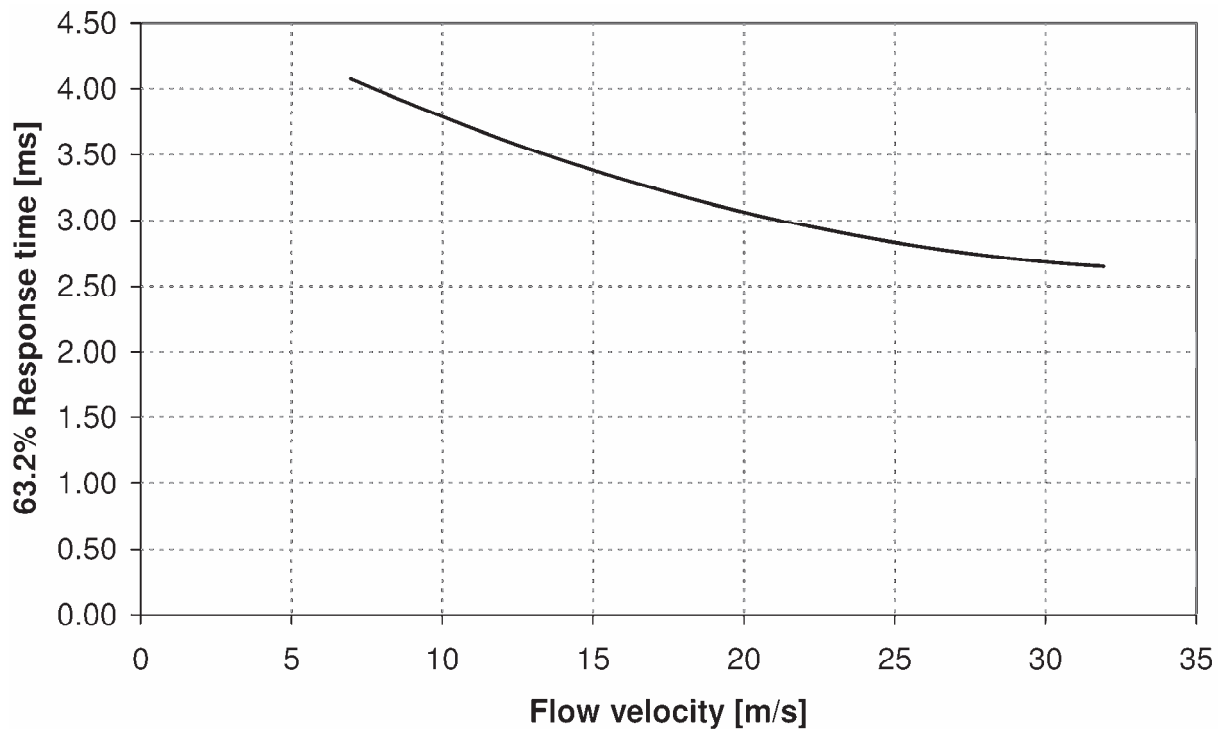


Figure 6.2 – Medterm Corp. 0.0005<sup>''</sup>-thermocouple response time [72]

## 6.2 Pressure Transducers

The pressure transducers used in this experimental work were manufactured by Sensortech GmbH and are designated SSC2070AB. These sensors were specifically designed to operate in harsh environments, and have a fully welded stainless steel diaphragm and very low temperature drift.

In order to allow a fast response time in the millisecond range, the sensor is connected to a custom made temperature compensated amplifier.



Figure 6.3 – SSC2070AB pressure transducer [73]

The sensors are then calibrated against a highly accurate secondary sensor to ensure accuracy of the measurements. A picture of the sensor can be seen in Figure 6.3.

## 6.3 Photodiodes

One of the most critical parts in the detection of the ignition is the photodiode. Its sensitivity and speed determine the accuracy of the induction time measurement.

The photodiodes employed here are manufactured by Advanced Photonics (API) Inc. and its designation is PDB-715-100 (blue enhanced). This photodiode is a detector/ amplifier hybrid that combines both the detector and operational amplifier in one package. [74]

This sensitivity of the photodiode is shown in Figure 6.4.

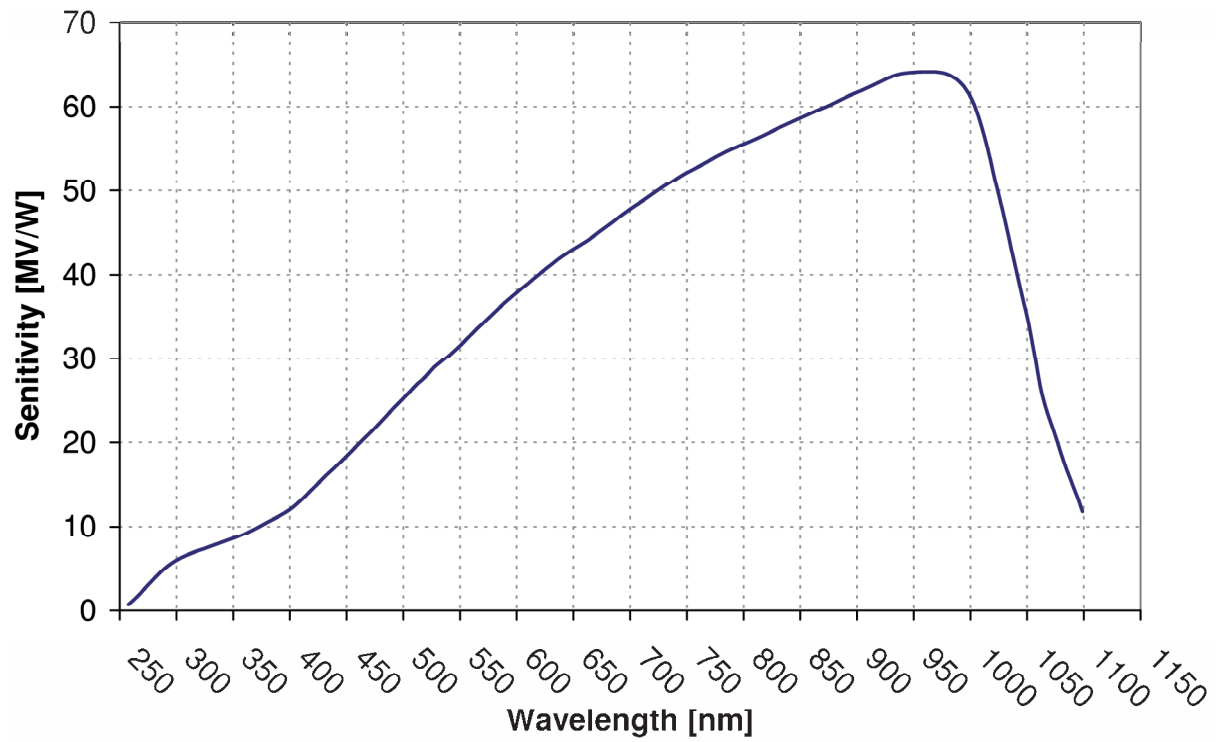


Figure 6.4 – PDB-715-100 Photodiode sensitivity [74]

## 7 Bibliography

1. Umweltbundesamt 2009 [cited Jan 2009]; Available from: <http://www.umweltbundesamt.de/>.
2. *Endenergieverbrauch in Deutschland 2007*. 2008, BDEW Bundesverband der Energie- und Wasserwirtschaft e.V.: Berlin.
3. Nitsch, J., et al., *Ökologisch optimierter Ausbau der Nutzung erneuerbarer Energien in Deutschland*. 2004, Bundesministerium für Umwelt, Naturschutz und Reaktorsicherheit: Heidelberg.
4. Warnaz, J., U. Maas, and R.W. Dibbel, *Verbrennung*. 2001, Berlin: Springer Verlag.
5. Schnaubelt, S., *Numerische Analyse des Selbstzündverhaltens einzelner Brennstofftropfen*, in *FB4*. 2004, University of Bremen: Bremen.
6. Aggarwal, S.K., *A Review of Spray Ignition Phenomena: Present Status and Future Research*. *Progress in Energy and Combustion Science*, 1998. **24**: p. 565-600.
7. Spadaccini, L.J. and J.A. TeVelde, *Autoignition Characteristics of Aircraft-Type Fuels*. *Combustion and Flame*, 1982. **46**: p. 283-300.
8. Sato, J., et al. *Ignition Process of Fuel Spray Injected into High Pressure High Temperature Atmosphere*. in *Twentyfirst Symposium (International) on Combustion*. 1986. Pittsburgh.
9. Edwards, C.F., D.L. Siebers, and D.H. Hoskin, *A Study of the Autoignition Process of a Diesel Spray Via High Speed Visualization*. SAE International, 1992: p. No. 920108.
10. Ikura, S., T. Kadota, and H. Hiroyasu, *Ignition Delay of Fuel Sprays in a Constant Volume Bomb*. *Transactions of the Japan Society of Mechanical Engineers*, 1981. **41**: p. 1559-1568.
11. Makoto, I., et al., *A Study of the Ignition Delay of Diesel Fuel Spray Using a Rapid Compression Machine*. *Transactions of the Japan Society of Mechanical Engineers*, 1987. **53B**: p. 274-281.
12. Yukio, M., C.J. Do, and N. Kazuyoshi, *Supplementary Study of Ignition Phenomena of Sprays using a Shock Tube*. *Transactions of the Japan Society of Mechanical Engineers*, 1990. **56B**(529): p. 2802-2807.
13. Cavaliere, A., et al., *Autoignition of N-Heptane and N-Tetradecane in Engine-Like Conditions*. *Combustion and Flame*, 1993. **93**(3): p. 279-286.
14. Livengood, J.C. and W.A. Leary, *Autoignition by Rapid Compression*. *Industrial and Engineering Chemistry*, 1951. **43**(12): p. 2797-2805.
15. Mullins, B.P., *Studies on the spontaneous ignition of fuels injected into a hot air stream*. *Fuel*, 1953. **32**(4): p. 451.
16. Taback, E.D., *The Autoignition Characteristics of JP-4 at High Temperature and Pressure*. 1971.
17. Spadaccini, L.J. and J.A. TeVelde, *Autoignition Characteristics of No. 2 Diesel Fuel*. 1981, NASA.
18. Spadaccini, L.J., *Journal of Engineering for Power*, Tans. ASME 99A, 1977.
19. Mestre, A. and F. Ducourneau, *Recent Studies of the Spontaneous Ignition of Rich Air-Kerosene Mixtures*, in *Combustion Institute European Symposium*. 1973.
20. Marek, C.J., L. Papatthakos, and P. Verbulecz, *Preliminary studies of autoignition and flashback in a premixing-prevaporizing flame tube using Jet-A fuel at lean equivalence ratios*. 1977, NASA.
21. Stringer, F.W., A.E. Clarke, and J.S. Clarke, *The Spontaneous Ignition of Hydrocarbon Fuels in a Flowing System* Proc. Auto. Div. . 1970: Institution of Mechanical Engineers.

22. Hinkeldey, O., et al., *Laser based study of auto-ignition of sprays in a continuous flow reactor*, in *3rd European Combustion Meeting - ECM 2007*. 2007: Mediterranean Agronomic Institute of Chania, Crete, Greece.
23. Wolff, M.C., et al. *The Influence of Evaporation on the Autoignition-Delay of n-Heptane Air Mixtures under Gas Turbine Conditions*. in *Twenty-Seventh Symposium (International) on Combustion*. 1998: The Combustion Institute.
24. Colket, M.B. and L.J. Spadaccini, *Scramjet fuels autoignition study*. Journal of Propulsion and Power, 2001. **17**(2): p. 315-323.
25. Spadaccini, L.J. and M.B. Colket, *Ignition Delay Characteristics of Methane Fuels*. Progress in Energy and Combustion Science, 1994. **20**(5): p. 431-460.
26. Vermeer, D.J., J.W. Meyer, and Oppenhei.Ak, *Auto-Ignition of Hydrocarbons Behind Reflected Shock-Waves*. Combustion and Flame, 1972. **18**(3): p. 327-&.
27. Miyasaka, K. and Y. Mizutani, *Ignition of Sprays by an Incident Shock*. Combustion and Flame, 1975. **25**(2): p. 177-186.
28. Nakabe, K., et al., *Burning Characteristics of Premixed Sprays and Gas-Liquid Coburning Mixtures*. Combustion and Flame, 1988. **74**(1): p. 39-51.
29. Moriue, O., et al., *Verification of a Numerical Simulation Model of Fuel Droplet Ignition through Microgravity Experiments and its Further Application*. Journal of The Japan Society of Microgravity Application, 2007. **24**(3): p. 251-254.
30. Schnaubelt, S., et al., *Verification of Detailed Numerical Simulations with Complex Chemistry for the Multi-Stage Selfignition Process of n-Decane Droplets*. Microgravity Science and Technology, 2001. **XII**(1): p. 20-23.
31. Schnaubelt, S., et al., *Verification of Detailed Simulations for Two-Stage Ignition of Single Droplets by Ignition Radii*. Space Forum (Proc. of Drop Tower Days 1998), 2000: p. 299-306.
32. Eigenbrod, C., et al., *Experimental and Numerical Studies on the Autoignition Process of Fuel Droplets*, in *Joint Meeting of the British, German and French Sections of the Combustion Institute*. 1999, The Combustion Institute: Nancy.
33. Anderson, J.D., *Modern Compressible Flow with Historical Perspective*. Third Edition ed. 2003: Mc Graw Hill.
34. Lefebvre, A.H., *Atomization and Sprays*. 1989: Hemisphere Publishing Corporation.
35. Bidone, G., *Expériences sur la Forme et sur la Direction des Veines et des Courants d'Eau Lancées par Diverses Ouvertures*. Imprimerie Royale, Turin, 1829: p. 1-136.
36. Savart, F., Ann. Chim. Phys., 1833. **53**: p. 337-386.
37. Rayleigh, L., *On the Instability of Jets*. Proc. London Math. Soc., 1878. **10**: p. 4-13.
38. Tyler, F., *Instabilities of Liquid Jets*. Philos. Mag. (London), 1933. **16**: p. 504-518.
39. Weber, C., *Disintegration of Liquid Jets*. Z. Angew. Math. Mech., 1931. **11**(2): p. 136-159.
40. Haenlein, A., *Disintegration of a Liquid Jet*. 1932.
41. Ohnesorge, W., *Formation of Drops by Nozzles and the Breakup of Liquid Jets*. Z. Angew. Math. Mech., 1936. **16**: p. 355-358.
42. Reitz, R.D., *Atomization and Other Breakup Regimes of a Liquid Jet*. 1978, Princeton University.
43. Czerwonatis, N., R. Eggers, and M. Hobbie, *Strahlzerfall und Tropfenwiderstand in Druckkräusen*. Chem. Ing. Tech., 2000. **72**(11): p. 1371-1375.
44. Tanner, F.X., *Atomization and Droplet Breakup Modeling of Diesel Sprays*. 1999.
45. Fraser, P.R. and P. Eisenklam, *Liquid Atomization and the Drop Size of Sprays*. Trans. Inst. Chem. Eng., 1956. **34**: p. 294 - 319.
46. Rosin, P. and E. Rammler, *The Laws Governing the Fineness of Powdered Coal*. J. Inst. Fuel, 1933. **7**(18): p. 29-36.

47. Mugele, R.A. and H.D. Evans, *Droplet Size Distribution in Sprays*. Industrial & Engineering Chemistry, 1951. **43**(6): p. 1317-1324.
48. Tate, R.W. *Some Problems Associated with the Accurate Representation of Drop-Size Distributions*. in *Proceedings of the 2nd International Conference on Liquid Atomization and Sprays (ICLASS)*. 1982. Madison, Wis.
49. Merrington, A.C. and E.G. Richardson, *The Break-Up of Liquid Jets*. Proceedings of the Physical Society, 1974. **59**(33): p. 1-13.
50. Panasenkov, N.J., *Zhurnal Tekhnicheskoi Fiziki*, 1951. **21**: p. 160.
51. Harmon, D.B., *Drop Sizes from Low Speed Jets*. Journal of The Franklin Institute, 1955. **259**(6): p. 519 - 522.
52. Miesse, C.C., *Correlation of Experimental Data on the Disintegration of Liquid Jets*. Industrial & Engineering Chemistry, 1955. **47**(9): p. 1690-1701.
53. Tanasawa, Y. and S. Toyoda, *On the Atomization of a Liquid Jet Issuing from a Cylindrical Nozzle*, in *Tech. Report of Tohoku University*. 1955, Tohoku University: Japan. p. 135.
54. Hiroyasu, H. and T. Katoda, *Fuel Droplet Size Distribution in a Diesel Combustion Chamber*. Bulletin of the JSME, 1976. **19**(135): p. 1064-1072.
55. Elkotb, M.M., *Fuel Atomization for Spray Modelling*. Progress in Energy and Combustion Science, 1982. **8**(1): p. 61-91.
56. Moriue, O., et al., *Numerical Simulation of the Ignition of a Single Fuel Droplet in Air with Finite Volume*, in *Proc. 9th Int. Conf. on Liquid Atomization and Spray Systems, ICLASS 2003*. 2003.
57. Tanabe, M., et al., *Numerical Analysis of Two-Stage Ignition of n-Heptane Isolated Droplets*, in *Twenty-Seventh Symposium (International) on Combustion*. 1998, The Combustion Institute: Boulder.
58. Schnaubelt, S., et al., *Detailed Numerical Simulations of the Multistage Selfignition Process of n-Heptane Isolated Droplets and their Verification by Comparison with Microgravity Experiments*. Proceedings of the Combustion Institute, 2000. **28**: p. 953-960.
59. *LabView 8.5 - Help*. 2009, National Instruments.
60. Savitzky, A. and M.J.E. Golay, *Smoothing and Differentiation of Data by Simplified Least Squares Procedures*. Analytical Chemistry, 1964. **36**(8): p. 1627-&.
61. Wu, P.K., et al., *Breakup processes of liquid jets in subsonic crossflows*. Journal of Propulsion and Power, 1996. **13**(1): p. 64-73.
62. Inamura, T., et al., *Disintegration phenomena of metalized slurry fuel jets in high speed air stream*, in *Proc. of 5th Int'l Conference on Liquid Atomization and Spray Systems (ICLASS-91)*. 1991: Gaithersburg, Maryland, USA. p. 839-846.
63. Oda, T., et al., *Characterization of Liquid Jet Atomization across a High-Speed Airstream*. JSME International Journal, 1994. **37-B**(4): p. 937-944.
64. Inamura, T. and N. Nagai, *Spray characteristics of liquid jet traversing subsonic airstreams*. Journal of Propulsion and Power, 1997. **13**(2): p. 250-256.
65. Lim, T.T., T.H. New, and S.C. Luo, *On the development of large-scale structures of a jet normal to a cross flow*. Physics of Fluids, 2001. **13**(3): p. 770-774.
66. Mashayek, A., A. Jafari, and N. Ashgriz, *Improved Model for the Penetration of Liquid Jets in Subsonic Crossflows*. AIAA Journal, 2008. **46**(11): p. 2674 - 2686.
67. Nguyen, T.T. and A.R. Karagozian, *Liquid Fuel Jet in Subsonic Cross-Flow*. Journal of Propulsion and Power, 1992. **8**(1): p. 21-29.
68. *Toxicological Profile for Jet Fuels JP-4 and JP-7*. 1995 [cited May 2009]; Available from: <http://www.atsdr.cdc.gov/toxprofiles/tp76.html>.

- 
69. Majer, V. and V. Svoboda, *Enthalpies of Vaporization of Organic Compounds: A Critical Review and Data Compilation*. 1985, Oxford: Blackwell Scientific Publications.
  70. Tanabe, M., et al., *Spontaneous Ignition of Liquid Droplets from a View of Nonhomogeneous Mixture Formation and Transient Chemical Reactions*, in *26th Symposium (Int.) on Combustion*. 1996: Naples.
  71. Rickmers, P., J.-C. Dittmer, and C. Eigenbrod, *Comparison of experimental and numerical results of the autoignition of n-heptane sprays under machine conditions*. *JASMA*, 2008. **25**(3): p. 367-370.
  72. *Medtherm Corporation*. 2009: Huntsville
  73. *Sensortechnics GmbH* 2009 [cited Sep. 2009]; Available from: <http://www.sensortechnics.com>.
  74. *Detector/Amplifier Hybrids With Feedback Resistor PDB-715-100*. [cited 2009 Sept. 2009]; Available from: <http://www.aptecelectronics.com/manuals/PDB-715-100.pdf>.